EXPLORATION OF PROTON TRANSFER PATHWAYS IN THE OXYGEN-TOLERANT [NiFe]-HYDROGENASE FROM *ESCHERICHIA COLI*



Emily J. Brooke

St. John's College

Trinity Term 2017

A thesis submitted to the Board of the Faculty of Physical Sciences, for the degree of Master of Science by Research, University of Oxford

EXPLORATION OF PROTON TRANSFER PATHWAYS IN THE OXYGEN-TOLERANT [NiFe]-HYDROGENASE FROM *ESCHERICHIA COLI*

Emily J. Brooke, St. John's College, University of Oxford

A thesis submitted for the degree of Master of Science by Research, Trinity Term 2017

Hydrogenases catalyse the interconversion of molecular hydrogen (H_2) with protons (H^+) and electrons (e^-). Thus, they are of significance due to the growing interest in a hydrogen economy, which would serve to replace fossil fuels. Hyd-1 is a [NiFe]-hydrogenase from *Escherichia coli* and, unlike many hydrogenases, it is capable of H_2 oxidation in the presence of O_2. Understanding the mechanism of H_2 activation by Hyd-1 is, therefore, paramount to the rational design of synthetic analogues which may be used in H_2 technologies. In this thesis, the role of several conserved carboxylate residues in [NiFe]-hydrogenases – E28, D118 and D574– has been explored using Protein Film Electrochemistry (PFE), solution assays and X-Ray crystallographic structures. PFE is a technique used in the study of redox proteins, including [NiFe]-hydrogenases. Precise potential control means that a detailed picture of an enzyme's thermodynamic and kinetic characteristics can be elucidated.

D118 and D574 form a canopy above the NiFe active site with the conserved arginine R509, which has recently been implicated as the base in H_2 oxidation. Although the high levels of conservation for these enzymes suggest an active role in H_2 oxidation, the rates of variants D574N and D118N/D574N indicate that they are not crucial to Hyd-1. Instead, D118 appears to have a role in controlling gas access to the active site and D574 is important for ensuring a wide potential window for H_2 oxidation in the presence of O_2.

Previous studies with E28 variants in a standard [NiFe]-hydrogenases have indicated that this highly conserved residue is part of an extended proton transfer network. The variant E28Q has unusual activity at high potential, which suggests that the role of E28 is more complex. This work has raised some interesting questions that require further exploration.

Acknowledgements

First my thanks must go to Professor Fraser A. Armstrong for giving me the opportunity to work in your lab on such an exciting project. I thank you for your guidance and insight throughout my studies, and for the opportunity to be your Academic Assistant, which allowed me to follow my passion for teaching. Although my time at Oxford has not ended as was initially intended, I will always feel privileged to have worked for you.

Second, I must thank Dr Rhiannon M. Evans. You have been my role model and mentor during my time at Oxford. You have provided me with not only endless guidance and support, but also with friendship. Thank you for proof reading everything I have ever given you, despite being as busy as you always are. I would not be writing this without you. A special thank you also must go to Dr Clare M. Megarity. Thank you for your friendship, for being a wonderful office-mate and always offering your honest opinion when sought. Stevie B, thank you for your stimulating conversations about anything and everything, including many about Taylor Swift. You have always been there to offer your advice and opinion, whether it be scientific or not. Every time we speak, I learn something new. Elena, thank you for your help with protein preps and support in the lab, and for putting up with, I'm sure, many silly questions! You deserve a medal. To the rest of the Armstrong group, past and present, thank you. I have been lucky to work with and get to know all of you. I will always remember the lunch time debates and the Christmas parties!

I would like to thank our collaborators. Professor Simon Phillips and Dr Stephen Carr (now at Oxford), you were instrumental in the structural studies. Steve, thank you for the many entertaining conversations about cats, Yorkshire and more. Dr Philip Ash and Professor Frank Sargent, you have been a part of stimulating conversations about this work. It has

been a pleasure working with you. Thank you to Dr Will Myers for your help with EPR spectroscopy, and for fishing my sample out of the resonator when I dropped it!

This work would not have been possible without the ICL support staff, including, but not limited to, Terri, Nenad, Martin and Dave. Thank you for all your help, whether it be breakages or ‘emergencies’. Martin, thank you for helping me with gas cylinder regulators during so many early mornings in the empty building.

During my time at Oxford, I have had the pleasure of supervising some wonderful students. Gerri, you set the bar for hard work and I am fortunate to have worked with you. I am grateful even more for your friendship, which I hope continues despite the ocean between us. Alex and Ed, it was a pleasure to work with you and I am grateful for all your hard-work.

Finally, I must thank my family, my partner and my friends for the endless love and support. Mum and Dad, you are my pillars of support and William, thank you for your pride. To my partner, Jack. No one makes me laugh like you do. Thank you for putting up with the tears and the stress during my time at Oxford. Thank you for knowing it won’t get better once I’m a teacher but for sticking around to make me laugh regardless.

Contents

Collaborations i

Publications ii

Symbols and Abbreviations iii

List of Figures vii

List of Tables x

1 Introduction 1

1.1 Hydrogen and Bacterial Metabolism 2

1.2 Escherichia coli and hydrogenases 2

1.3 Why study hydrogenases? 4

1.4 Hydrogenases use nickel and iron 7

1.5 Hydrogenase structure 8

1.5.1 [NiFe]-hydrogenases 8

1.5.2 [FeFe]-hydrogenases 11

1.6 Fe-S Clusters in [NiFe]-hydrogenases 12

1.6.1 Standard Hydrogenases 12

1.6.2 Membrane-Bound Oxygen Tolerant Hydrogenases 13

1.7 Catalytic bias 14

1.8 Mechanism of Oxygen Tolerance in [NiFe]-hydrogenases 17

1.9 [NiFe]-hydrogenase Catalytic Cycle 19

1.10 Mechanism of Hydrogen Activation 22

1.10.1 Kubas Mechanism vs. Frustrated Lewis Pairs 22
1.10.2 [FeFe]-Hydrogenases and H_2 activation 24
1.10.3 Hydrogenase Model Catalysts 25
1.10.4 [NiFe]-Hydrogenases 28
1.11 Topics addressed in this thesis 30
2 Experimental Methods and Theory 31
2.1 Solutions 32
2.2 Molecular Biology Methods 32
2.2.1 Strains, Plasmids and Oligonucleotide Primers 32
2.2.2 Cell Growth and Culture 34
2.2.3 Methods for Genetic Engineering 35
2.2.4 The pMAK cycle 42
2.3 Purification of Hydrogenase-1 45
2.3.1 Aerobic Isolation 45
2.4 Crystallography of Hyd-1 Variants 48
2.4.1 Aerobic Isolation for X-Ray Crystallography 49
2.5 Mediator-based Solution Assays for H_2 Oxidation by Hydrogenase 51
2.6 Electrochemical Theory 52
2.6.1 Overview of Protein Film Electrochemistry 52
2.6.2 Three Electrode System 52
2.6.3 Cyclic Voltammetry 53
2.6.4 Chronoamperometry 57

2.6.5 Mass Transport 57
2.7 Electrochemical methods 58
2.7.1 Experimental set up 58
2.7.2 Growing an enzyme film 60
2.7.3 Modification of PGE Electrodes 60
2.7.4 Enzyme film activation 61
2.8 Electron Paramagnetic Resonance Spectroscopy 61
2.8.1 Theory of EPR Spectroscopy 61
2.8.2 EPR Spectroscopy Methods 62
3 The Role of D118 and D574 in *Ec*Hyd-1 63
3.1 Introduction to Proton Transfer in [NiFe]-hydrogenases 64
3.2 Mechanism of Proton Transfer 64
3.3 Proposed Proton Transfer Pathways 65
3.4 The 'First Proton' Transfer Network 69
3.5 Contributions to this chapter 71
3.6 Results 72
3.6.1 Rates and pH optima 72
3.6.2 Electrocatalytic Window and E_{Switch} 73
3.6.3 Michaelis constant and activation enthalpies 75
3.6.4 Oxygen Tolerance 77
3.6.5 H_2 Production 81
3.6.6 Crystal Structures 84

3.7 Discussion 86

4 The role of conserved glutamate-28 in Hyd-1 91

4.1 Introduction 92

4.1.1 E28 and proton transfer 92

4.1.2 In search of the Michaelis complex 94

4.1.3 Contributions to this thesis 97

4.2 Results 97

4.2.1 Turnover frequency and electrocatalytic profile 97

4.2.2 Michaelis Constant and Activation Enthalpy of E28D 98

4.2.3 Kinetic Isotope Effect of E28D 99

4.2.4 Response of E28D to O_2 and CO 100

4.2.5 pH profile of E28Q 102

4.2.6 Response of E28Q to O_2 and CO 104

4.2.7 EPR Spectra 106

4.2.8 Crystal Structures 108

4.3 Discussion 109

4.4 Conclusions and future work 114

5 Bibliography 116

6 Appendices 123

6.1 Nernst Equation 124

6.2 pH dependence of native Hyd-1 and canopy variants 126

6.3 Michaelis-Menten Kinetics and Hanes-Woolf Analysis 127

6.4 Eyring equation and use 131

6.5 Correcting for a current offset 134

6.6 CO dependence of E28D 135

6.7 pH dependence of E_{Kick} 136

Collaborations

Several collaborations have contributed to this work. Advice regarding molecular biology work was generously offered by Professor Frank Sargent at the University of Dundee.

Professor Simon E. V. Phillips and Dr Stephen B. Carr at the Research Complex at Harwell (RCaH) (now at the University of Oxford) were instrumental in the crystallographic studies. Elena Nomerotskaia kindly helped Part II student Alexander Bridgeman, and me prepare protein samples. Prof. Phillips and Dr Carr collected data and built models for the crystal structures. Analysis of samples was done by myself or Alexander Bridgeman under my supervision, with guidance from Dr Carr when required. Prof. Phillips and Dr Carr also provided useful discussions about this work.

Gerri M. Roberts was a summer student on the SURF programme from the California Institute of Technology (CalTECH) who worked on the H_2 production studies of Hyd-1 canopy variants under my supervision. Some of this data and analysis was then repeated by myself. Alexander Bridgeman performed initial Protein Film Electrochemistry and solution assays experiments for Hyd-1 variants E28D and E28Q under my supervision. Again, this was repeated by myself. Edward Mallet, a Part II student, performed Protein Film Electrochemistry and solution assays for Hyd-1 variants D118V and D118E under my supervision.

Advice regarding the EPR experiments was provided by Dr Kourosh H. Ebrahimi in the Armstrong group. When he was unavailable, help was provided by Dr William K. Myers at the Centre for Advanced Electron Spin Resonance (CÆSR) at the University of Oxford.

Dr Philip Ash in the group of Professor Kylie A. Vincent at the University of Oxford was involved in many discussions about the variants E28D and E28Q, discussed in Section 4

Publications

Evans, R. M.; Brooke, E. J.; Wehlin, S. A. M.; Nomerotskaia, E.; Sargent, F.; Carr, S. B.; Phillips, S. E. V.; Armstrong, F. A., Mechanism of hydrogen activation by [NiFe]-hydrogenases. *Nat. Chem. Biol*., **2016**, *12*, 46-50

Carr, S. B.; Evans, R. M.; Brooke, E. J.; Wehlin, S. A. M.; Nomerotskaia, E.; Sargent, F.; Armstrong, F. A., Phillips, S. E. V., Hydrogen activation by [NiFe]-hydrogenases. *Biochem. Soc. Trans*. **2016**, *44* (3), 863-868

Brooke, E. J.; Evans, R. M.; Islam, S. T. A.; Roberts, G. M., Wehlin, S. A. M.; Carr, S. B.; Phillips, S. E. V.; Armstrong, F. A., Importance of the active site "canopy" residues in an O_2-tolerant [NiFe]-hydrogenase. *Biochemistry*. **2017**, *56* (1), 132-142

Symbols and Abbreviations

Å	Angstrom
A	Ampere (amp)
B_0	strength of external magnetic field
Cam	Chloroamphenicol
CHES	buffering agent, N-Cyclohexyl-2-aminoethanesulfonic acid
C_{O}	Concentration of species O
CV	cyclic voltammogram
Cy	Cyclohexyl
Df	*Desulfovibrio fructosovorans*
*Df*MF	[NiFe]-hydrogenase from *Desulfovibrio fructosovorans* Miyazaki F
D_{O}	Diffusion coefficient
Dv	*Desulfovibrio vulgaris*
$E_{\text{entry/exit}}$	reduction potential of electron entry/exit site in a redox protein
E	electrode potential
e^-	electron
E^{o}	standard reduction potential
$E^{\mathrm{o}}_{\mathrm{cell}}$ or E_{cell}	standard cell potential or cell potential
E_{eq}	equilibrium potential
E_{Kick}	second threshold potential seen for E28Q
$E_{\text{ox/red}}$	reduction potential for a species ox/red
EPR	Electron Paramagnetic Resonance
E_{Switch}	the potential at which Ni-B is reductively reactivated

*Ec*Hyd-1	*Escherichia coli* Hydrogenase-1
*Ec*Hyd-2	*Escherichia coli* Hydrogenase-2
F	Faraday constant $= 96\,485$ C mol^{-1}
FLP	Frustrated Lewis Pair
FTacV	Fourier Transform alternating current Voltammetry
FT-IR	Fourier Transform Infrared Spectroscopy
g_e	value of g for a free electron $= 2.00232$
h	Planck constant $= 6.626\,x\,10^{-34}$ J s
H^+	proton
HEPES	buffering agent, 4-(2-hydroxyethyl)-1-piperazineethanesulfonic acid
i	current
IET	Interfacial Electron Transfer
i_{lim}	maximum current due to mass transport limitations
i_{obs}	observed current
K	Kelvin
K	equilibrium constant
k	rate constant
k_{B}	Boltzmann constant $= 1.381\,x\,10^{-23}$ J K^{-1}
k_{cat}	turnover frequency for an enzyme-catalysed reaction. Also known as k_2 in Michaelis-Menten kinetics
K_2HPO_4	buffering agent, potassium phosphate dibasic
KH_2PO_4	buffering agent, potassium phosphate monobasic
KIE	kinetic isotope effect
K_{M}	Michaelis constant; enzyme specific affinity constant
MBH	membrane-bound hydrogenase

MES	buffering agent, 2-(N-morpholino)ethanesulfonic acid
mV	millivolts
n	number of electrons
NaCl	sodium chloride
NAD(P)H	refers to the reduced forms of Nicotinamide Adenine Dinucleotide Phosphate (NADP) and Nicotinamide Adenine Dinucleotide (NAD)
NRVS	Nuclear resonance vibrational spectroscopy
PCR	Polymerase Chain Reaction
PFE	Protein Film Electrochemistry
PGE	Pyrolytic Graphite Edge
PT	proton transfer
q	charge
R	gas constant $= 8.314$ J K^{-1} mol^{-1}
RCaH	Research Complex at Harwell
*Re*MBH	*Ralstonia eutropha* Membrane Bound Hydrogenase
RDE	Rotating Disk Electrode
scc min^{-1}	standard cubic centremetres per minute
SCE	Saturated Calomel Electrode
SDS PAGE	sodium dodecyl sulfate polyacrylamide gel electrophoresis
SHE	Standard Hydrogen Electrode
T	temperature in Kelvin
TAPS	buffering agent, tris(hydroxymethyl)methylamino]propanesulfonic acid
Tris-HCl	buffering agent, tris(hydroxymethyl)aminomethane
V	volts
v	velocity (rate of enzyme-catalysed reaction)

vs.	versus
^{o}C	degrees Centigrade
ΔG	Gibbs free energy change
ΔH	change in enthalpy
ΔS	change in entropy
μ	micro
μ_B	Bohr magneton
ω	rotation rate

List of Figures

Figure 1.1: Subunit composition of Hyd-1 in the periplasmic membrane in cartoon form. ... 3

Figure 1.2: Structural representation of the active sites of [NiFe]- and [FeFe]-hydrogenases. 8

Figure 1.3: Crystal structure of the Hyd-1 tetramer $(HyaAB)_2$ from *Escherichia coli*. 9

Figure 1.4: The Fe-S clusters in standard [NiFe]-hydrogenases. 12

.....14

Figure 1.6: A comparison of Hyd-1 and Hyd-2 at pH 6 and 37 ^{o}C under 100% H_2. 15

Figure 1.7: The inactive, oxidised Ni-A state in *E. coli* Hyd-1. 17

Figure 1.8: Catalytic Cycle of O_2-tolerant [NiFe]-hydrogenases. 21

Figure 1.9: Example metal complexes with H_2 and dihydride ligands. 22

Figure 1.10: Bonding of dihydrogen (H_2) to a transition metal centre through σ-donation and back donation. 23

Figure 1.11: Reversible H_2 activation by $(Mes_2P)C_6F_4(B(C_6F_5)_2)$. 24

Figure 1.13: H_2 activation by [FeFe]-hydrogenases using a pendent amine base. 25

Figure 1.14: Hydrogenase model compounds. 26

Figure 1.15: General structure of Cy complexes with amino acid or dipeptides. 27

Figure 1.16: The conserved arginine (R509) in [NiFe]-hydrogenases, shown in *Ec*Hyd 1. 28

Figure 2.1: PCR to generate two linear fragments from plasmid DNA. 38

Figure 2.2: Agarose gel showing fragments of pMAK hyaB following PCR. 38

Figure 2.3: Recombination events leading to introduction of a mutation from a free plasmid onto the chromosome of *E. coli*. 42

Figure 2.4: Chromatogram from Ni-affinity chromatography of the Hyd-1 variant D118N/D574N. 47

Figure 2.5: Denaturing electrophoresis (SDS-PAGE) of native Hyd-1. 48

Figure 2.6: Three electode set up for Protein Film Electrochemistry. 53

Figure 2.7: Cyclic voltammetry.....54

Figure 2.8: The electrical double layer at an electrode-solution interface.....55

Figure 2.9: Cyclic voltammogram of native Hyd-1 on a pyrolytic graphite edge electrode. .57

Figure 2.10: Electrochemical set up for Protein Film Voltammetry.. 59

Figure 2.11: Zeeman splitting of electron spin states in a magnetic field.....62

Figure 3.1: The Grotthuss Mechanism of proton transport through a chain of water molecules. 65

Figure 3.2: Proton transfer pathways proposed for [NiFe]-hydrogenases. 66

Figure 3.3: Direction of proton transfer networks away from the active site.....69

Figure 3.4: The active site 'canopy' of Hyd-1, including the conserved D118 and D574.....70

Figure 3.5: Electrocatalytic profile for H_2 oxidation by Hyd-1 and variants.....74

Figure 3.6: Potential dependence of $K_{H_2}^{M}$ for native Hyd-1 and canopy variants.. 76

Figure 3.7: Potential dependence of $\Delta H^{\ddagger}$ for native Hyd-1 and canopy variants.....77

Figure 3.8: Response of H_2 oxidation to native Hyd-1, D574N and D118N/D574N to a transient burst of O_2. 79

Figure 3.9: Response of H_2 oxidation by native Hyd-1, D574N and D118N/D574N to prolonged O_2 exposure.....80

Figure 3.10: Sensitivity of native Hyd-1 and canopy variants to CO.....81

Figure 3.11: H_2 evolution by native Hyd-1 and canopy variants at pH 3 and 1% H_2. 83

Figure 3.12: Comparison of D118A and D574N at pH 3 – 9 and 1% H_2. 84

Figure 3.13: The active sites of native Hyd-1, D574N and D118N/D574N. 85

Figure 3.14: Putative gas channels in native Hyd-1, including the bottleneck residues E28, V78, D118 and L126. 88

Figure 3.15: The potential window for O_2-tolerant H_2 oxidation for native Hyd-1 and D118N/D574N. 90

Figure 4.1: The active site of native Hyd-1 with residue E28.....92

Figure 4.2: Ni-C to Ni-SI transition in [NiFe]-hydrogenases, as proposed by Greene *et al*. 94

Figure 4.3: H_2 binding modes at the active site of [NiFe]-hydrogenases. 95

Figure 4.5: Electrocatalytic profile of native Hyd-1 and E28D.....98

Figure 4.6: The potential dependence of the Michaelis constant $K_{H_2}^M$ and the activation enthalpy $\Delta H^{\ddagger}$ for native Hyd-1 and E28D. 99

Figure 4.7: H_2/D_2 Kinetic Isotope Effect (KIE) for native Hyd-1 and E28D. 100

Figure 4.8: Response of native Hyd-1 and E28D to O_2. 101

Figure 4.9: Cyclic voltammetry of E28Q at pH 6 and 37 ^{o}C. 102

Figure 4.10: pH dependence of electrocatalytic H_2 oxidation by E28Q.....103

Figure 4.11: Response of E28Q in the presence of small molecule inhibitors. 105

Figure 4.12: X-band EPR spectra of E28D (upper) and E28Q (lower) at 70 K (left) and 15 K (right). 107

Figure 4.13: Crystal structures of native Hyd-1, E28D and E28Q. 109

Figure 4.15: Swinging arm mechanism for proton transfer by amino acid carboxylate side chains. 110

Figure 6.1: pH dependence of native Hyd-1, D574N and D118N/D574N. 126

Figure 6.2: Cyclic voltammograms of the Hyd-1 variant D574N in different H_2/Ar mixes. .130

Figure 6.3: Example of a Hanes-Woolf analysis for the Hyd-1 canopy variant D574N.. ...130

Figure 6.4: Cyclic voltammograms of Hyd-1 variant D574N at different temperatures. 133

Figure 6.5: Example of an Eyring plot for the Hyd-1 canopy variant D574N. 133

Figure 6.6: Current offset adjustment for R509K film on a modified electrode. 134

Figure 6.7: CO flow experiment for E28D. 135

Figure 6.8: Determining E_{Kick} for E28Q.....136

Figure 6.9: pH dependence of E_{Kick} for E28Q. 136

List of Tables

Table 1.1: Reduction potentials (mV *vs.* SHE) of Fe-S clusters in O_2-sensitive and O_2-tolerant hydrogenases. 13

Table 2.1: Strains used in this research 32

Table 2.2: Plasmids used in this research. 33

Table 2.3: Oligonucleotide Primers used in this research 33

Table 2.4: Buffers for preparation of competent cells using RbCl methods. 35

Table 2.5: Reaction mixture for a 50 μL PCR using Q5 polymerase.. 37

Table 2.6: Thermocycling conditions for PCR for Site-Directed Mutagenesis with Q5 Polymerase. 37

Table 2.7: Buffer used in agarose gel electrophoresis for DNA separation. 39

Table 2.8: Buffers used in PCR Purification using Quiagen QIAquick Method. 39

Table 2.9: Buffers for Gel Extraction of PCR products. 40

Table 2.10: Reaction mixture for Gibson Assembly.. 41

Table 2.11: Buffers for DNA purification by mini-prep. 41

Table 2.12: Reaction mixture for a 60 μL PCR using Taq polymerase. 44

Table 2.13: Thermocycling conditions for colony PCR with Taq Polymerase. 44

Table 2.14: Buffers for Hyd-1 Purification. 46

Table 2.15: Buffers for SDS-PAGE. 47

Table 2.16: Additional buffers required for Hyd-1 purification for X-Ray Crystallography. ..49

Table 2.17: Buffers used in Crystallisation of Hyd-1 variants. 50

Table 3.1: Kinetic data for Hyd-1 and canopy variants. 72

Table 4.1: Turnover frequencies of H_2 oxidation for native Hyd-1, E28Q and E28D at pH 6 and 25 ^{o}C. 98

1 Introduction

1.1 Hydrogen and Bacterial Metabolism

The reducing and hydrogen (H_2) rich nature of Earth's early atmosphere[1] led to the evolution of organisms capable of using H_2 in their metabolism. The range of organisms able to use H_2 is broad and includes prokaryotes, eukaryotes and archaeal classes.[2] Hydrogen is used in many distinct metabolic contexts including the generation of electrons for respiration or removal of excess reducing equivalents.[3] The enzyme nitrogenase also produces H_2 during nitrogen fixation but this is later recycled.[4] Despite the diversity in the organisms that use H_2, hydrogen cycling is catalysed universally by enzymes known as hydrogenases according to reaction (1.1):[2, 5]

$$H_2 \rightleftharpoons H^- + H^+ \rightleftharpoons 2H^+ + 2e^- \quad (1.1)$$

Broadly, hydrogenases are classified according to the metal content of their active site, [NiFe]-, [FeFe] and [Fe]-only, as discussed in more detail in Section 1.4. However, more specific groupings have been proposed based on their cellular location and function.[2] Recently, these have been expanded[6] as the number of known hydrogenases (including putative hydrogenases) and cellular functions has increased.

1.2 Escherichia coli and hydrogenases

Escherichia coli (*Ec*) is a facultative anaerobe capable of growth in a variety of conditions and can metabolize H_2.[7] Under anaerobic conditions, *E. coli* produces four [NiFe]-hydrogenases termed Hydrogenase-1 (Hyd-1), Hydrogenase-2 (Hyd-2) and so on,[8-9] which allow *E. coli* to use both respiratory H_2 oxidation and H_2 evolution during metabolism. Little is known about Hyd-4, but there is a significant body of work concerning the others: all three are membrane-bound [NiFe]-hydrogenases (MBH) comprised minimally of a large and small subunit containing the active site (Section 1.4) and Fe-S clusters (Section 1.6), respectively.[10] Hyd-1 (Group 1d)[6] is expressed from the *hya* operon during the stationary

phase of growth.[11-12] The small and large subunits are the products of the *hyaA* and *hyaB* genes, respectively. A transmembrane domain on the C-terminus of HyaA anchors Hyd-1 to the periplasmic membrane, where it associates with a *b*-type cytochrome (HyaC) that links it to the membrane quinone pool (Figure 1.1)[10, 13] Although its *specific* function remains speculative, Hyd-1 is a respiratory H_2 uptake (oxidising) hydrogenase.[7-8] It should be noted that although Hyd-1 is produced under anaerobic conditions, it is able to function in the presence of oxygen (O_2). It is an "O_2-tolerant" [NiFe]-hydrogenase[14-16] (Section 1.8) and so may be important when there is a switch from anaerobic to aerobic conditions.[10]

Hyd-2 is a standard [NiFe]-hydrogenase[16] (Section 1.8) that is expressed maximally under exponential growth conditions from the *hyb* operon.[10] The large and small subunits are HybC and HybO, respectively, and HybO also contains a transmembrane domain. Hyd-2 contains two additional peptides: one is a second Fe-S cluster containing peptide (HybA) which mediates electron transfer from the quinone pool to Hyd-2, and the other is predicted to be

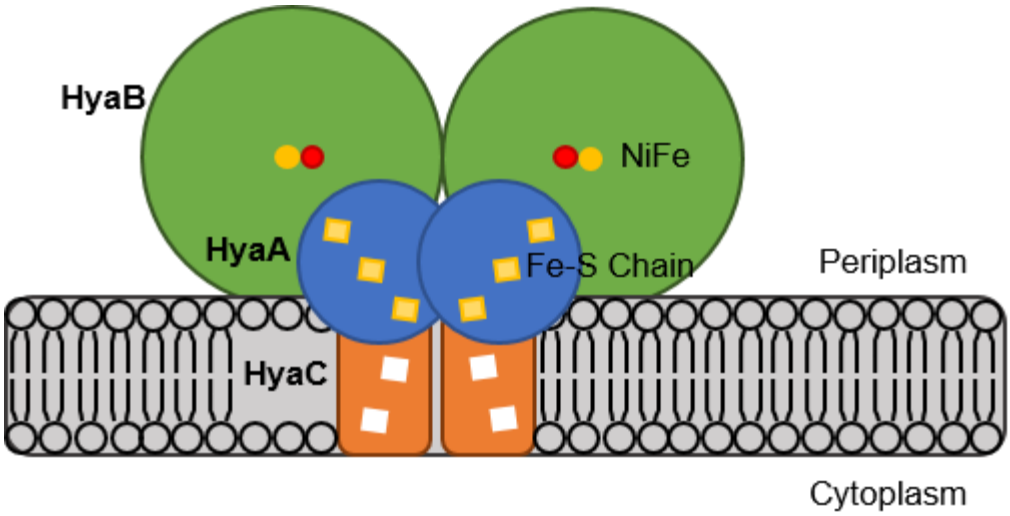


Figure 1.1: Subunit composition of Hyd-1 in the periplasmic membrane in cartoon form. Hyd-1 is composed of a small subunit (HyaA, blue) containing three Fe-S clusters (yellow squares), a large subunit (HyaB, green) containing the NiFe active site (red, yellow circles) and a cytochrome *b* subunit (HyaC, orange) with two haem groups (white squares). Hyd-1 resides in the periplasm and is anchored to the periplasmic membrane by a C-terminal transmembrane α-helix, which links it to cytochrome *b*. Hyd-1 is arranged as a $(HyaAB)_2$ dimer of heterodimers (or tetramer). H_2 is oxidised at the NiFe active site and electrons are transferred to the membrane quinone pool via the Fe-S cluster relay and the cytochrome *b*.

an integral membrane protein (HybB).[17] Despite early indications that Hyd-2 is also a respiratory uptake hydrogenase,[7] protein film electrochemistry (Chapter 2) showed that Hyd-2 is in fact bidirectional.[16] Instead, it appears that Hyd-2 is able to affect the redox conditions in the cell when required by acting as a "release valve" to remove or supply electrons.[17]

Hyd-3 is expressed under anaerobic fermentative conditions and is part of the formate hydrogenlyase (FHL) complex, which converts formate into CO_2 and H_2 under specific conditions.[18] It is well documented that [NiFe]-hydrogenases are typically more proficient in H_2 oxidation[5] and, although Hyd-2 is expected to be bidirectional *in vivo*, Hyd-3 is unusual in that it functions solely as a H_2 producer. Like Hyd-2, however, on an electrode Hyd-3 can catalyse both H_2 oxidation and H_2 evolution.[18]

1.3 Why study hydrogenases?

Fossil fuels make the largest contribution to meeting current energy demands. Not only are fossil fuels finite resources, but the emission of carbon oxides (CO_2, CO) and other harmful products through fossil fuel use is associated with climate change and health issues.[19-20] Climate change is an important issue, and society is seeking alternatives to fossil fuels. Alternative fuels are expected to be "clean" (non-greenhouse gas emitting) and sustainable.[5, 20] Among these alternative fuels, H_2 has been recognised as a clean energy carrier for four decades.[19] Use of H_2 as a fuel is advantageous because it has the highest energy content per mass of any fuel (120 MJ/kg compared with 46.4 MJ/kg for petrol),[19-20] and under combustion in O_2 the only reaction product is water making it carbon neutral.[19, 21] However, it is not without disadvantages. The low density of H_2 means it has a low energy content by volume density and larger storage containers are required for a given journey, for example, when compared with other fuels (e.g. methane).[19] Although the topic of H_2 storage is beyond the scope of this thesis, metal-based compounds may be used if the H_2

adsorption/desorption kinetics can be optimised.[21-22] Currently the major source of industrially produced H_2 is fossil fuels, for example by steam reforming of natural gas, making H_2 production unsustainable and non-carbon neutral.[19, 23] Aside from the applications of H_2 as a fuel, we must also not forget that H_2 is an important reagent and has many industrial uses, including in the synthesis of ammonia, via the Haber-Bosch process, and in methanol production.[24]

A viable H_2 economy requires non-fossil fuel based methods for H_2 production, such as water electrolysis, and the development of efficient H_2 devices including fuel cells that oxidise H_2 to generate electricity. Platinum (Pt) is the most efficient catalyst for both water electrolysis and H_2 oxidation. However, Pt is a finite and thus expensive resource, and is also poisoned by reagent contaminants, including CO.[5] Additionally, traditional fuel cells use Pt for both the H_2 oxidation (anode) and O_2 reduction (cathode) reaction, and this lack of specificity requires a membrane to separate the reactions, adding considerable cost to fuel cell production.[5]

The pressure to move towards renewable energy carriers has resulted in an intensive research effort to understand biological catalysts, including hydrogenases. The selectivity of enzymes for their substrates should eliminate the need to separate anodic and cathodic reactions of fuel cells using expensive membranes.[5] Hydrogenases are highly active in both H_2 oxidation and evolution (although they do have a catalytic bias, Section 1.7), and have been shown to catalyse H_2 oxidation at rates comparable to Pt despite using earth-abundant metals at their active sites.[25] Hydrogenases have already been utilised in both water electrolysis and fuel cells, including one example in which a hydrogenase/laccase fuel cell powered a digital wristwatch for 24 hours.[26] Regarding chemical feedstocks, enzymes are increasingly being accepted as viable catalysts for industry as they are highly selective, and include catalytic hydrogenation by oxidoreductase enzymes.[27] Many oxidoreductases, however, require hydride transfer from NAD(P)H cofactors for their reactions. These cofactors are expensive and so the possibility of recycling/regenerating them is desirable.

This has been performed successfully using a system that couples the oxidoreductase for the hydrogenation reaction to a hydrogenase for cofactor regeneration.[27]

Despite their high efficiencies, it is unlikely that hydrogenases will ever be used directly in H_2 devices for several reasons:[5] firstly, many hydrogenases are unable to function under oxidative conditions and would be inactivated by O_2 in a membrane-less H_2/O_2 fuel cell. There is, however, a subset of [NiFe]-hydrogenases which are O_2-tolerant (Section 1.8) and over the past decade a picture of how these enzymes deal with O_2 has appeared.[14-15, 28-29] Although these may be better candidates, the other disadvantages mean that they are unlikely to be used. Secondly, fuel cells require enzymes to be stably immobilised on an electrode surface in an orientation that allows facile electron transfer. Many hydrogenases, including Hyd-1, readily absorb onto pyrolytic graphite edge (PGE) electrodes,[5, 16] but without covalent attachment these are still susceptible to 'film loss' over time. However, some methods for covalent attachment have been developed.[30-31] Unlike small molecule catalysts, hydrogenases have the additional disadvantage of being bulky (Section 1.5) and the number of enzyme molecules that can fit on a planar electrode surface in a monolayer arrangement is, therefore, restricted. Only enzymes in a monolayer arrangement can exchange electrons with the electrode surface rapidly, and so the current density and power output of the fuel cell are limited.[5] These problems may be overcome by using 3D electrodes that allow for increased enzyme loading whilst maintaining electronic contact.[30, 32] Additionally, the complex biological machinery required for hydrogenase expression means that producing large quantities of enzyme can be difficult.

Given these disadvantages, it is more likely that synthetic catalysts will replace hydrogenases in H_2 devices. However, it is crucial that we understand how hydrogenases activate H_2 so that synthetic catalysts can be designed in a rational and logical manner. Some mechanistic details are known (Sections 1.9 and 1.10) but other aspects remain elusive, including how protons are transported to and from the active site. Synthetic model

compounds are discussed in more detail in Section 1.10.3 but chemists are becoming increasingly accepting of catalysts that, like enzymes, include more than just an active site: recent examples of hydrogenase model compounds include a second coordination sphere to allow proton transfer between solvent and the metal site.[33] Prior to these many model compounds were not bidirectional, catalysing solely H_2 oxidation or evolution. Additionally, large overpotentials and the need for non-aqueous solutions has been observed.[5]

1.4 Hydrogenases use nickel and iron

Hydrogenases are classified according to the nature of their active site which contain nickel and/or iron, i.e. [NiFe]-, [FeFe]- and the [Fe]-hydrogenases (Figure 1.2).[5] The focus of this report is the [NiFe]-hydrogenases and so the latter will not be addressed. It is, however, useful to draw comparisons to the [FeFe]-hydrogenases in some instances (see below).

[NiFe]-hydrogenases contain a Ni and Fe connected by two bridging cysteine residues. A further two cysteine residues coordinate the Ni and the Fe has three exogenous ligands identified as CN^- and CO by FT-IR spectroscopy.[34-37] Although common in organometallics, CN^- and CO are not usually seen in biological complexes, but are also present in the [FeFe]-hydrogenases and play an important role in modulating the redox properties of the active site: in the [NiFe]-hydrogenases, these strong field ligands ensure Fe is maintained in a Fe(II), low spin state and thus only the Ni oxidation state changes during catalysis (Section 1.9); similarly, in the [FeFe]-hydrogenases, only the oxidation state of the Fe distal to the [4Fe4S] cluster cycles during catalysis.[5] Each metal has a vacant coordination site for H_2 (or small molecule inhibitors) to bind.

A subset of the [NiFe]-hydrogenases contain selenocysteine in place of one of the terminal cysteine residues (C576, Hyd-1). These will not be discussed here in any detail but the selenocysteine imparts unique properties onto the [NiFeSe]-hydrogenases. For example, [NiFe]-hydrogenases are inhibited by H_2 (they are ‘product inhibited’) but the [NiFeSe]-

hydrogenases exhibit lower product inhibition. Additionally, many hydrogenases are inactivated by O_2 (Section 1.8) but the [NiFeSe]-hydrogenases appear to have a greater tolerance to O_2.[38] These characteristics have led to their use in H_2 devices.[39]

In the [FeFe]-hydrogenases, a single cysteine residue anchors the active site to the protein scaffold and links the FeFe site to a $[4Fe4S]^{2+/+}$ cluster.[5] Collectively, the FeFe bimetallic site and Fe-S cluster are referred to as the 'H-cluster'. Each Fe is coordinated by a CO and CN ligand, and linked by a bridging CO ligand and an azadithiolate bridge. The azadithiolate bridge is crucial for activity and is directly involved in catalysis, acting as the base in H_2 activation (Section 1.10.2).[40]

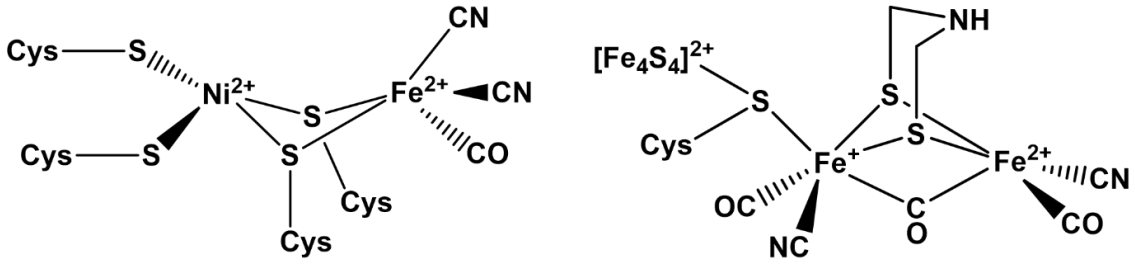


Figure 1.2: Structural representation of the active sites of [NiFe]- and [FeFe]-hydrogenases. Both active sites are shown with a vacant coordination site: for the [NiFe]-hydrogenases, the vacant site bridges the two metals and the active site is shown in the "Ni-SI" state (Section 1.9); for the [FeFe]-hydrogenases, the vacant site lies on the distal Fe and the "H_{ox}" state is shown.

1.5 Hydrogenase structure

1.5.1 [NiFe]-hydrogenases

The first crystal structure was published in 1995 when the structure of the periplasmic [NiFe]-hydrogenase from *Desulfovibrio gigas* (*Dg*) was resolved to 2.85 Å,[37] although a [NiFe]-hydrogenase had been crystallised some years before.[41] Since then, a number of structures have been published and include both the standard and O_2-tolerant [NiFe]-hydrogenases classes.[5] Figure 1.3 shows the structure of the O_2-tolerant Hyd-1. The structures of all [NiFe]-hydrogenases are very similar: the active site is buried within the large

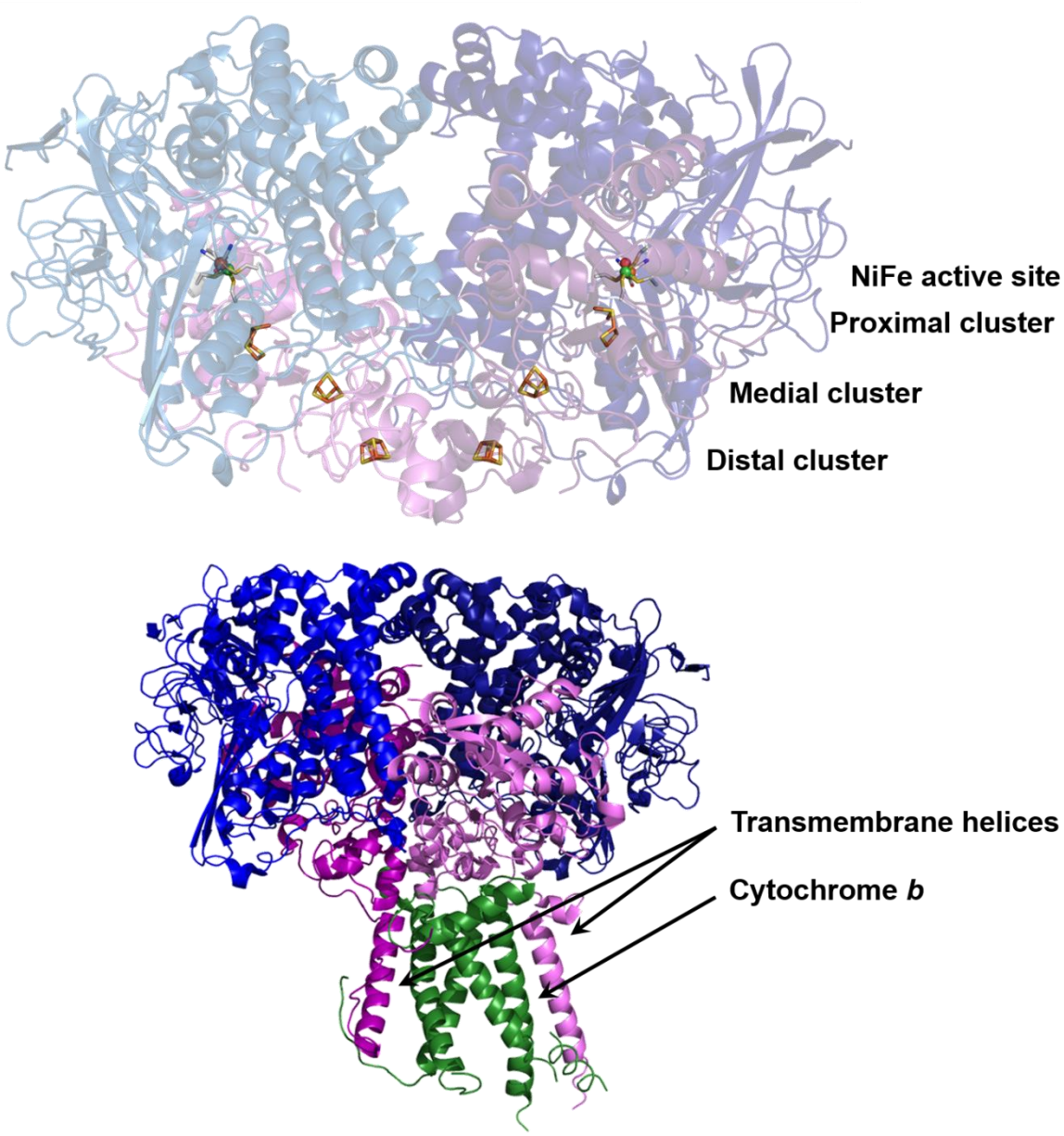


Figure 1.3: Crystal structure of the Hyd-1 tetramer $(HyaAB)_2$ from *Escherichia coli*. Upper – Hyd-1 at 1.7 Å resolution shown in cartoon form. The large subunits are shown in blue and the small subunits in pink. The active site ligands and Fe-S clusters are shown in stick form, and the Ni and Fe are shown as spheres. So that the Fe-S clusters and the active site can be seen clearly, the cartoon is shown at 60% transparency. Crystal structure produced from a Hyd-1 hyaA(ΔTM,his_6) strain which has a his_6 affinity tag but does not have the transmembrane α-helix to simplify purification. PDB: 5A4M. **Lower** – Hyd-1 at 3.3 Å resolution also shown in cartoon form but including the transmembrane helices and a single cytochrome *b* (green). The enzyme is the P242C variant which has a [4Fe4S] cluster in place of the [3Fe4S] cluster. However, overall the structure is unchanged from that of native Hyd-1. Only one cytochrome *b* crystallised with the $(HyaAB)_2$ tetramer. PDB: 4GD3

subunit (~ 60 kDa) and a chain of three iron sulfur clusters in the small subunit (~35 kDa) form an electron transport pathway. The identity of these clusters will be discussed in more detail in Section 1.6. Additionally, the small subunit of MBHs have a C-terminal α-helical transmembrane domain which anchors the hydrogenase to the membrane through hydrophobic interactions, so it can associate with cytochrome *b*.[5, 13] Typically, both the transmembrane domain and the redox partner go unseen in crystal structures due to increased mobility in these regions,[42] but a structure of a Hyd-1 HyaA variant P242C published in 2013 included both the transmembrane helix and cytochrome *b* (Figure 1.3).[13] However, only a single cytochrome *b* per dimer of heterodimers $(HyaAB)_2$ was observed and it is unlikely that this is the physiological form *in vivo*.

Whilst most [NiFe]-hydrogenase structures show a single heterodimer (a single small and large subunit), structures of MBH, including Hyd-1, show a tetramer (or dimer of heterodimers, e.g. $(HyaAB)_2$).[5] It is worth mentioning that although the MBH from *Ralstonia eutropha* (*Re*MBH) crystallised as a single heterodimer, there is evidence to suggest that it exists as a tri-heterodimer.[29, 43] The aggregation state of different [NiFe]-hydrogenases may be important when O_2 attacks (Section 1.8).

As well as an electron transport chain, hydrophobic channels run from the protein surface to the active site, allowing transport of the non-polar substrate H_2 (and small molecule inhibitors e.g. O_2, CO) to and from the active site.[5] Although there are electronic tools available to calculate channels in protein structures (e.g. *Caver*[44]), for some [NiFe]-hydrogenases they have been experimentally determined using X-ray crystallography with noble gas probes.[45-46] Recent work by Kalms *et al* demonstrated that the number and diameter of tunnels in O_2-tolerant and standard hydrogenases differs. Oxygen-tolerant enzymes tend to have narrower tunnels and fewer openings on the surface. The case is extreme for Hyd-1 which has only one tunnel opening on its surface.[45] The number of channels and their diameter may, therefore, be a governing factor in the sensitivity of different

enzymes to small molecule inhibitors. However, it is not the sole origin of O_2-tolerance (Section 1.8). As well as noble gas studies, mutagenic studies have also been used to explore the gas channels. At the NiFe active site, there is a bottleneck to the gas channels formed by three residues – V78, D118 and L126. D118 will be explored in detail in Chapter 3 (and refs 47-48) but variants of these three residues effect gas diffusion to the active site, observed through greatly enhanced Michaelis constants $K_{\mathrm{M}}^{\mathrm{H_2}}$ (i.e. lower affinities for H_2).

Proton transfer is a pre-requisite for H_2 oxidation or evolution (reaction 1.1) and specific proton transfer pathways allow H^+ movement to and from the NiFe active site. For the [NiFe]-hydrogenases, the identity of such pathways is still speculative and several models have been proposed based on multiple computational and experimental studies.[49-53] There are, however, two common starting points for these pathways. The first is via one of the terminal cysteinate-S Ni ligands and the second is via a conserved arginine residue suspended directly above the NiFe site, both of which are proposed to be the base in H_2 activation (Section 1.10.4).[5, 48]

1.5.2 [FeFe]-hydrogenases

Compared with the [NiFe]-hydrogenases, far fewer crystal structures of [FeFe]-hydrogenases have been produced. To date, the only structures available from the protein data bank (PDB) are those of hydrogenase I from *Clostridium pasterianum* (*Cp*I),[54] the periplasmic hydrogenase from *Desulfovibrio desulfuricans*[55] and HydA from *Chlamydomonas reinhardtii* (*Cr*HydA).[56] The latter, however, was produced from a strain that is missing key maturation proteins HydE, HydF and HydG. As a result, it contains only the the [4Fe4S] cluster and the [FeFe] site is missing. Many other [FeFe]-hydrogenases have been identified through the highly conserved catalytic domain, or 'H-cluster domain', which contains the H-cluster.[5] Other aspects of [FeFe]-hydrogenase structure are far less conserved, including the number of subunits and Fe-S clusters. For example, *Cr*HydA exists

only as the H-cluster domain and has no additional Fe-S clusters[56] whilst *Cp*I contains three additional domains and four more Fe-S clusters.[54] For the [FeFe]-hydrogenases, gas channels have not been determined experimentally and putative channels are based on computational results.[57-58] Of the three proposed gas channels, one is speculated to be the dominant pathway for O_2 diffusion to the active site.[58]

1.6 Fe-S Clusters in [NiFe]-hydrogenases

1.6.1 Standard Hydrogenases

Movement of electrons to/from the protein surface (and thus physiological redox partners) is mediated by a chain of three Fe-S clusters that are located within electron tunnelling distance (< 14 Å[59]) of one another/the active site.[5] In standard hydrogenases, a [4Fe4S] cluster resides in the proximal and distal positions, and a [3Fe4S] cluster in the medial

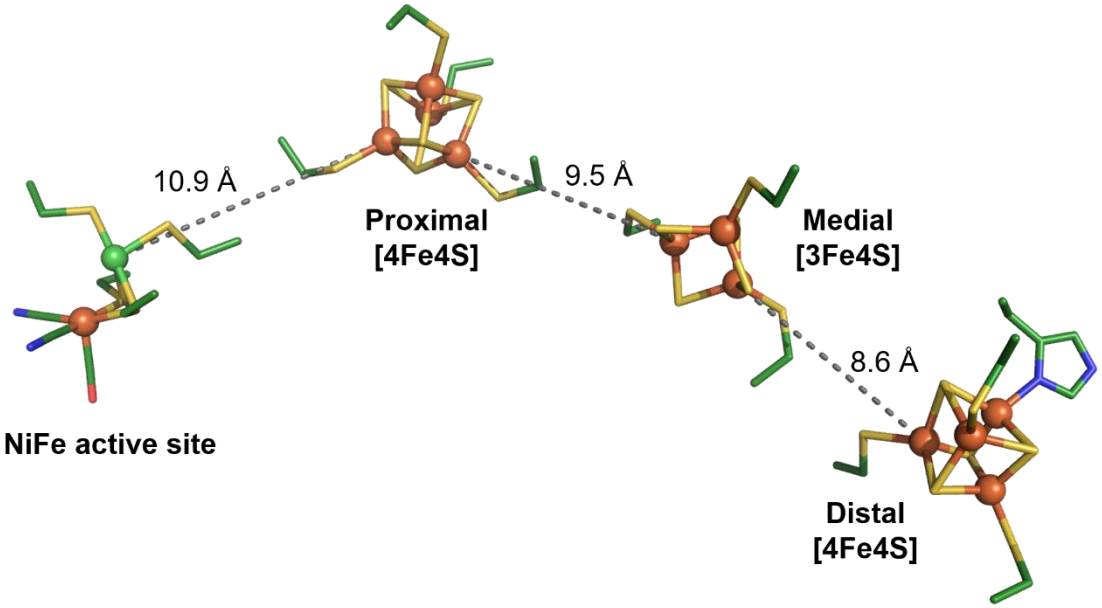


Figure 1.4: The Fe-S clusters in standard [NiFe]-hydrogenases. Standard [NiFe]-hydrogenases have a proximal [4Fe4S] cluster, a medial [3Fe4S] cluster and a distal [4Fe4S] cluster with an unusual Cys_3His coordination. The closest distance between the active site and/or the clusters is shown. Each distance is less than 14 Å, the maximum distance for electron tunnelling as described by Dutton *et al*.[59] The active site and clusters are shown in stick form with metal atoms shown as spheres. Crystal structure is the *Desulfovibrio fructosovorans* Miyazaki F [NiFe]-hydrogenase at 0.89 Å. The active site [O] ligand was removed to represent the Ni-SI state. PDB: 4U9H

position (Figure 1.4).[37] One of the coordinating cysteine residues at the distal cluster is replaced with a histidine.[60-61] This is also seen in a cluster of *Cp*I[54] and the Fe-S clusters of other redox proteins and may affect the electron transfer rate.[61] The reduction potentials of Fe-S clusters (Table 1.1) are typically measured by potentiometric titrations using Electron Paramagnetic Resonance (EPR) Spectroscopy, although recent work by Adamson *et al* has used Fourier Transformed alternating current Voltammetry (FTacV) to determine the reduction potential of the distal cluster in Hyd-1.[62] The reduction potential of the distal cluster is crucial for understanding the catalytic bias of [NiFe]-hydrogenases (Section 1.7).

Table 1.1: Reduction potentials (mV *vs.* SHE) of Fe-S clusters in O_2-sensitive and O_2-tolerant hydrogenases.

	Proximal $[4Fe4S]^{2+/+}$	**Proximal $[4Fe3S]^{5+/4+}$**	**Proximal $[4Fe3S]^{4+/3+}$**	**Medial $[3Fe4S]^{+/0}$**	**Distal $[4Fe4S]^{2+/+}$**
O_2-sensitive	−340[a]	n/a	n/a	+65[a]	−340[a]
O_2-tolerant	n/a	230 ± 15[b] 232[c]	30 ± 30[b] 87[c]	190 ± 30[b] 68[c]	−228[d]/−190* −78[c]

[a]data for [NiFe]-hydrogenase from *Desulfovibrio fructosovorans* at pH 8, taken from ref [63]

[b]data for Hyd-1 at pH 6, taken from ref [64]

[c]data for O_2-tolerant [NiFe]-hydrogenase from *Aquifex aeolicus* at pH 7.4, taken from ref [65]

[d]data for O_2-tolerant Hyd-1 from *Escherichia coli* at pH 7 taken from ref [62]

*The distal cluster of Hyd-1 is EPR Silent and so this value is modelled, taken from ref 66

1.6.2 Membrane-Bound Oxygen Tolerant Hydrogenases

There are two crucial differences between the Fe-S clusters of membrane bound O_2-tolerant [NiFe]-hydrogenases and their O_2-sensitive counterparts. Firstly, the reduction potentials of the Fe-S clusters in O_2-tolerant MBHs are consistently higher (Table 1.1). Secondly, the O_2-tolerant MBHs have a unique proximal cluster. Work in 2011 began to shed light on this unusual cluster through the discovery that six, rather than four, cysteines coordinate the iron atoms.[15, 67] Protein Film Electrochemistry (PFE, Section 2.6) experiments indicated C19 (Hyd-1) is crucial for O_2-tolerance.[15, 67] It was later revealed that the proximal

cluster is in fact a [4Fe3S] cluster in which a sulfide is replaced with a cysteine-S ligand.[68] This unusual coordination allows the cluster to undergo structural changes and cycle between three oxidation states ([4Fe3S]$^{5+/4+/3+}$) to donate *two* electrons.[28, 64-65, 68] In the superoxidised (5+) state, Fe4 shifts, and the broken Fe-S bond is replaced by the backbone amide of Cys20 in Hyd-1 (Figure 1.5). This state is seen in many Group 1d O_2-tolerant [NiFe]-hydrogenases, including, but not limited to, *Re*MBH and Hyd-1. The structure of *Re*MBH is shown in Figure 1.5 as an example.

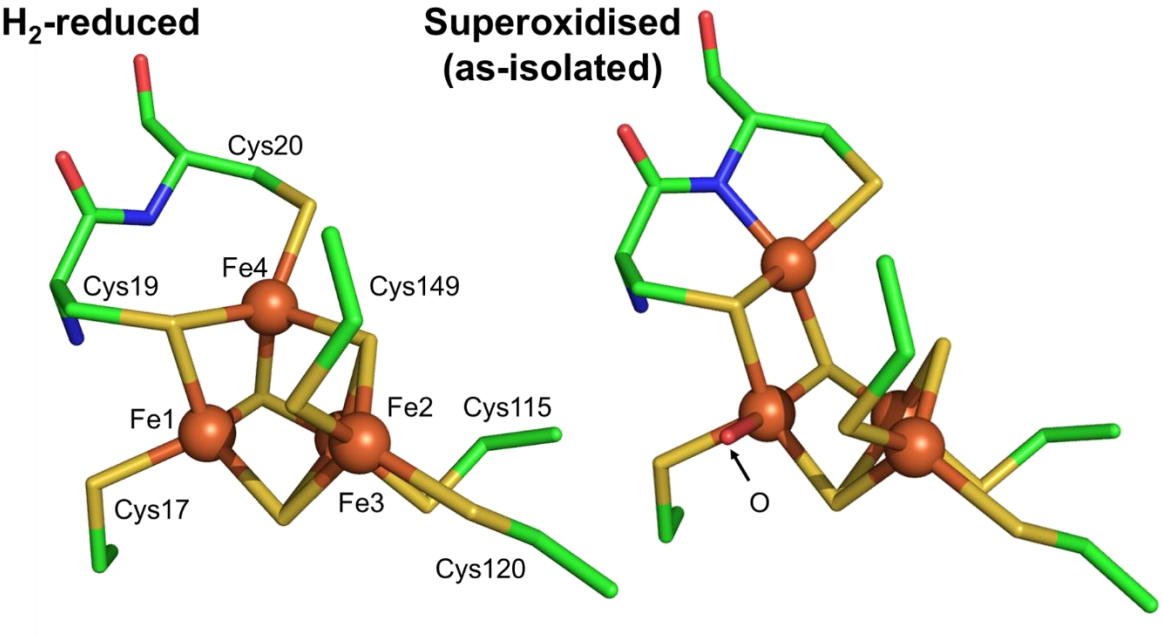


Figure 1.5: Cluster morphing of the proximal cluster of O_2-tolerant [NiFe]-hydrogenases. The [4Fe3S] proximal cluster of *Re*MBH in the H_2-reduced (left) and as-isolated (right) states. The Fe-S cluster is shown as sticks, with Fe atoms as spheres. Cysteine residues are shown as sticks. A corner sulphide is replaced by Cys19 which coordinates two Fe atoms. In the as-isolated (superoxidised) states, Fe4 migrates and is coordinated by the backbone amide of Cys20. PDB: H_2-reduced 3RGW, As-isolated 3IUC

1.7 Catalytic bias

Although catalysts can have no intrinsic bias for reaction direction beyond that dictated by thermodynamics, many catalysts exhibit greater rates for one reaction direction. In the hydrogenases, a 'catalytic bias' is observed and the different classes of hydrogenases have higher rates in H_2 oxidation *or* H_2 evolution. Whilst the [FeFe]-hydrogenase are generally

considered to be H_2 evolvers, the [NiFe]-hydrogenases are more active in H_2 oxidation.[5] The O_2-tolerant [NiFe]-hydrogenases show an extreme bias, exhibiting no H_2 evolution at neutral pH and ambient temperatures.[16, 69] In part, this is due to strong product inhibition by H_2[70-71] but it is also controlled by the reduction potentials of the electron relay. A comparison of Hyd-1 and Hyd-2 on an electrode (Figure 1.6) at pH 6 and under 100% H_2 reveals that Hyd-1 does not evolve H_2 and requires that an additional driving force, or 'overpotential', is applied before H_2 oxidation is seen.

Hexter *et al* proposed a model[66] that links catalytic bias and the overpotential requirement to the reduction potential of a catalyst's electron entry/exit site ($E_{entry/exit}$): a catalyst will only act reversibly if the difference between $E_{entry/exit}$ and the equilibrium potential of the substrate ($E_{eq}(H^+/H_2)$ here) is minimal. For the [NiFe]-hydrogenases, the distal [4Fe4S] cluster is expected to fulfil the role as the electron entry/exit site and in the O_2-tolerant enzymes the higher potentials of the distal cluster, compared with their standard counterparts (Table 1.1),

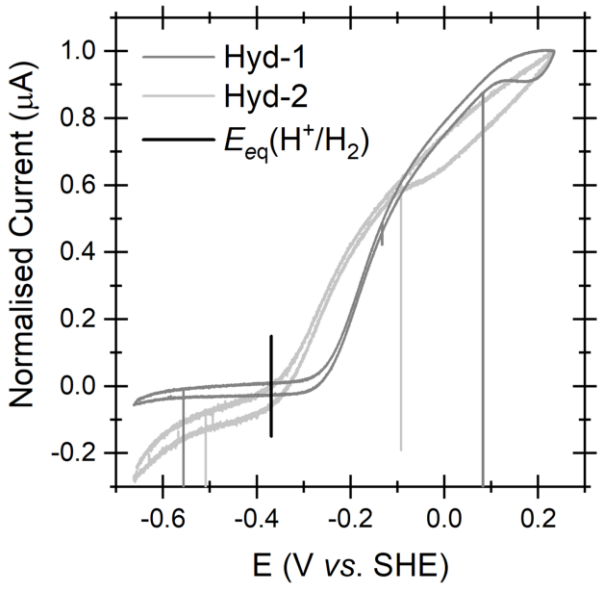


Figure 1.6: A comparison of Hyd-1 and Hyd-2 at pH 6 and 37 °C under 100% H_2. Cyclic voltammograms of Hyd-1 (dark grey) and Hyd-2 (light grey) adsorbed on pyrolytic graphite edge electrodes. The equilibrium potential for the H_2 couple $E_{eq}(H^+/H_2)$ is shown in black. Hyd-1 shows no H_2 evolution current (negative current) and an increased overpotential requirement for H_2 oxidation. Other conditions: −0.65 V to +0.24 V, total gas flow 500 scc min^{-1}, ω = 1000 rpm, the current was normalised relative to the current at the upper potential limit.

increase the difference between $E_{entry/exit}$ and $E_{eq}(H^+/H_2)$. However, given that the reduction potentials of Fe-S clusters are not pH-dependent, and that the $E_{eq}(H^+/H_2)$ changes by −60 mV per pH unit and −30 mV per order of magnitude change in pressure of H_2 ($p(H_2)$), it was proposed that Hyd-1 would be capable of H_2 evolution under conditions in which $E_{eq}(H^+/H_2)$ and $E_{entry/exit}$ meet. This was demonstrated by Murphy *et al* who turned Hyd-1 into a proficient H_2 producer at low pH and low $p(H_2)$.[69]

The role of the distal cluster and its control over catalytic bias was further explored by Adamson *et al*.[62] The distal cluster in Hyd-1 is EPR silent and so its reduction potential has not been determined using potentiometric titration. Although PFE (Section 2.6) can be used to determine reduction potentials of redox enzymes, for Hyd-1 this has not been possible (Section 2.6.3). Adamson, however, used FTacV to determine the potential of the distal cluster in native Hyd-1 and a variant hyaA-R193L.[62] Arginine-193 is conserved in the O_2-tolerant [NiFe]-hydrogenases and is located close enough to the His ligand of the distal cluster (Section 1.6.2) to form cation-π interactions, which may alter the redox properties of the distal cluster.[62] In the hyaA-R193 variant, the distal cluster had a reduction potential of −0.228 V at pH 7, an decrease of approximately 60 mV in comparison with native Hyd-1 (Table 1.1) putting it closer to $E_{eq}(H^+/H_2)$. The authors measured the ratio of H_2 oxidation current to H_2 production current at pH 3 and 1% H_2 to determine the catalytic bias of the two enzymes: this was measured to be 3.2 for native Hyd-1 and 1.1 for hyaA-R193L. Not only is there a significant shift in the bias of the hyaA-R193L variant, but at pH 7 a marked decrease in the overpotential requirement for H_2 oxidation was observed.[62] These results clearly demonstrate the importance of the reduction potential of the distal cluster in determining the catalytic bias of [NiFe]-hydrogenases and provide further experimental evidence in support of the model by Hexter.

1.8 Mechanism of Oxygen Tolerance in [NiFe]-hydrogenases

Although the [FeFe]-hydrogenases are irreversibly damaged by O_2,[72] some [NiFe]-hydrogenases can sustain H_2-oxidation in the presence of O_2. These enzymes are referred to as 'O_2-tolerant',[14-15] whilst those that are inactivated by O_2 are 'O_2-sensitive' or 'standard' hydrogenases. The most extensively studied O_2-tolerant enzymes are the MBH, including Hyd-1, but other types also include the actinobacterial-type [NiFe]-hydrogenase from *Ralstonia eutropha*.[73]

There are two spectroscopically defined inactive states (EPR and FT-IR spectroscopies) referred to as 'Ni-A' and 'Ni-B' which can form as the result of O_2 attack.[5] Ni-A is the product of incomplete O_2 reduction and long reactivation times result in it being referred to as an 'Unready' state.[14-15, 74-75] Ni-A has been the subject of discussion for many years.[5] Although it was known to be a Ni(III) state, the identity of the bridging ligand has remained uncertain and speculation has included a peroxo species.[76] Structures of the aerobically crystallised [NiFe]-hydrogenase from *Desulfovibrio fructosovorans*, however, provide evidence for a bridging hydroxide and a sulfenate at one of the bridging cysteines[77], also seen in Hyd-1

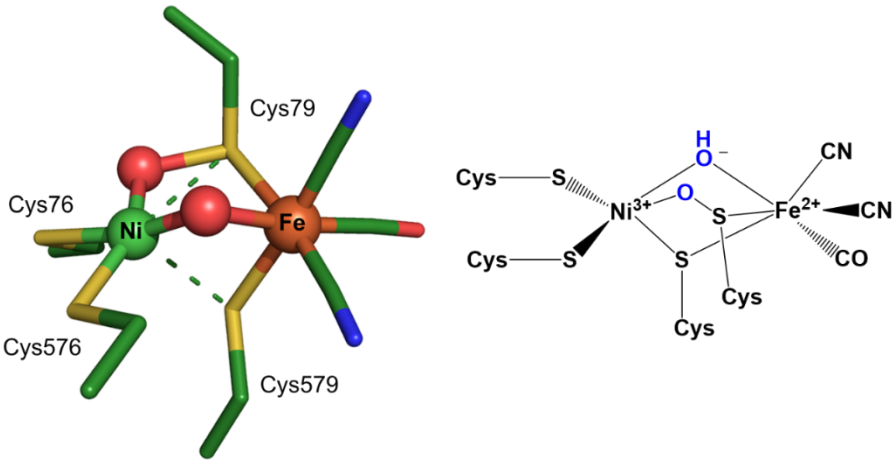


Figure 1.7: The inactive, oxidised Ni-A state in *E. coli* Hyd-1. The Ni-A state is represented in a crystal structure (left) and ChemDraw representation (right). In the crystal structure, the cysteine and Fe ligands are seen in stick form, the metals and oxygens are shown as spheres. Cys79 is consistently the site of additional oxidation to sulfenic acid refs 48, 77. Ni is in the 3+ oxidation state and Fe in the 2+ state. PDB: 5A4M

structures (C79 in Hyd-1, Figure 1.7).[48] Ni-B, or the 'Ready' state, is a Ni(III) state with a solvent derived bridging hydroxide[78] and is rapidly reactivated with H_2 or at low potential. Ni-B is also formed under anaerobic oxidising conditions,[15, 78] i.e. by applying a high electrode potential or in the presence of mediators such as $K_3[Fe(CN)_6]$.

Oxygen-tolerance requires that: (1) all four electrons for the complete reduction of O_2 are supplied immediately and, (2) Ni-B is the sole product of O_2 attack[74] and is rapidly reactivated.[14-15] In the O_2-tolerant [NiFe]-hydrogenases, advantages are not only afforded by the higher reduction potentials of the Fe-S clusters (Table 1.1), but also the special $[4Fe3S]^{5+/4+/3+}$ proximal cluster which can donate two electrons (Section 1.6).[28, 68] The medial $[3Fe4S]^{+/0}$ cluster has also been shown to be crucial for O_2-tolerance.[14] The fourth electron is provided by oxidation of the active site to form Ni-B. For continuing H_2 oxidation, Ni-B is then rapidly reactivated by Ni(III) to Ni(II) reduction and protonation of OH^- so that the enzyme can enter the catalytic cycle. Standard [NiFe]-hydrogenases, however, become trapped in Unready states when O_2 attacks and activity is lost. It should be noted that a mixture of states, including Ni-A, is produced when O_2-tolerant enzymes are purified aerobically without H_2.[48]

To date, all O_2-tolerant [NiFe]-hydrogenases, with the exception of *Re*MBH, have been crystallised as the $(HyaAB)_2$ tetramer.[5] For Hyd-1, this quaternary arrangement places the two distal clusters within 12.2 Å of one another, a distance short enough for electron transfer[59] and suggests that if O_2 attacks the active site of one HyaAB dimer, electrons could be supplied by the second HyaAB dimer. Like the Hyd-1 tetramer, the isolated hyaAB heterodimer (referred to as "monomer" in ref 79) achieved steady state H_2 oxidation in a continuous flow of O_2 and rapidly reactivated once the O_2 was removed. Formation of Ni-B exclusively is, therefore, not related to the tetramer formation of Hyd-1. However, in conventional solution assays using enzyme that had been activated prior to being exposed

to air, a larger 'lag phase' before reduction of benzyl viologen began was seen for the heterodimer.[79] For the tetramer, electrons can be shared between the two distal clusters leading to faster reactivation of Ni-B; this may be an important mechanism for dealing with O_2 *in vivo*.

1.9 [NiFe]-hydrogenase Catalytic Cycle

The catalytic cycle of [NiFe]-hydrogenases has been examined using FT-IR and EPR spectroscopies.[5] There are some differences in the catalytic cycles of the different classes of [NiFe]-hydrogenases,[5] but only the cycle specific to O_2-tolerant [NiFe]-hydrogenases is shown in Figure 1.8.

The two inactive states known as Ni-A and Ni-B were discussed in the context of O_2-tolerance in Section 1.8. An enzyme in any inactive states must be reactivated by reduction prior to catalysis. Ni-A is slowly reactivated to form the Ni-SU state, a Ni(II) species with an oxygen ligand, which requires further reduction before catalysis can begin. In the presence of H_2, Ni-B is the only state present following O_2 attack of the O_2-tolerant enzymes, and so only this state is shown in Figure 1.8. Reduction of Ni-B forms the EPR silent Ni-SI, a Ni(II) state with a vacant coordination site to which H_2 binds. In standard hydrogenases, it has been demonstrated that reduction of Ni-B forms one of two isoelectronic Ni-Si_r states (I and II). The structure of these remains speculation and differs depending on the enzyme but proposals include a loosely bound bridging hydroxide ($(Ni\text{-}Si_r)_I$) or water molecule ($(Ni\text{-}Si_r)_{II}$). Loss of the bridging ligand results in formation of the Ni-SI_a state, which is equivalent to Ni-SI.[5]

On binding to Ni-SI, H_2 is immediately activated by the [NiFe] site and a local base (Section 1.10.4), forming an EPR silent Ni(II)-hydride known as Ni-R and a proton. Multiple Ni-R states are seen in the FT-IR spectra and which may reflect the proton being located at different bases.[80] In an ultra-high resolution (< 1 Å) structure of the [NiFe]-hydrogenase from

Desulfovibrio vulgaris Miyazaki F (*Dv*MF) in the Ni-R state[81], additional electron density was observed on one of the terminal cysteine residues and has been modelled as a proton (Figure 1.8). However, the angle of the Ni-S-H bond is very small (82º) which suggests the assignment may be incorrect. Additionally, recalculation of $2F_o$-F_c maps for C546 in the *Dv*MF by our collaborators suggests that the S of C546 is, in fact, displaced rather than protonated.[82] Oxidation of Ni-R produces a Ni(III) state with a bridging hydride that is EPR active and known as Ni-C.[5] It is expected that oxidation of Ni-C and proton transfer results in hydrogenase returning to Ni-SI so that a new catalytic cycle can begin.

EPR and FT-IR spectra also reveal a Ni(I) species known as Ni-L, which contains no bridging ligand but has a formal metal-metal bond, and is formed by reductive elimination of the hydride as a proton.[83] Thus, Ni-L and Ni-C are tautomers. The exact location of the proton is unknown but there are three spectroscopically defined Ni-L states in which the proton is expected to reside on different bases.[5, 80] One proposal for Ni-L includes Ni-cysteine thiol that is hydrogen bonded to a nearby base (Section 4.1.1).[84-85] In the past, Ni-L has been disregarded as an artefact because of reports that it is only seen following illumination of Ni-C at cryogenic temperatures, resulting in photolysis of the bridging hydride. However, the conversion of Ni-C to Ni-L occurs in Hyd-1 in dark conditions at high pH[86] and in the standard [NiFe]-hydrogenase *Dv*MF when the proximal cluster is reduced (i.e. under H_2).[87] These results provide Ni-L with a more significant role in the catalytic cycle of [NiFe]-hydrogenases than was previously assumed. The transition from Ni-C to Ni-SI directly requires *simultaneous* proton and electron transfer but this is not possible under conditions under which the proximal cluster is reduced, and so Ni-L acts as an intermediate between the Ni-C and Ni-SI states.[86] The role of Ni-L has led to its reassignment as 'Ni-I' by Greene *et al*.[88] This is more relevant to the O_2-tolerant [NiFe]-hydrogenases as the higher potential Fe-S clusters are more likely to be in the reduced states under the low potential conditions required for Ni-C and Ni-L.

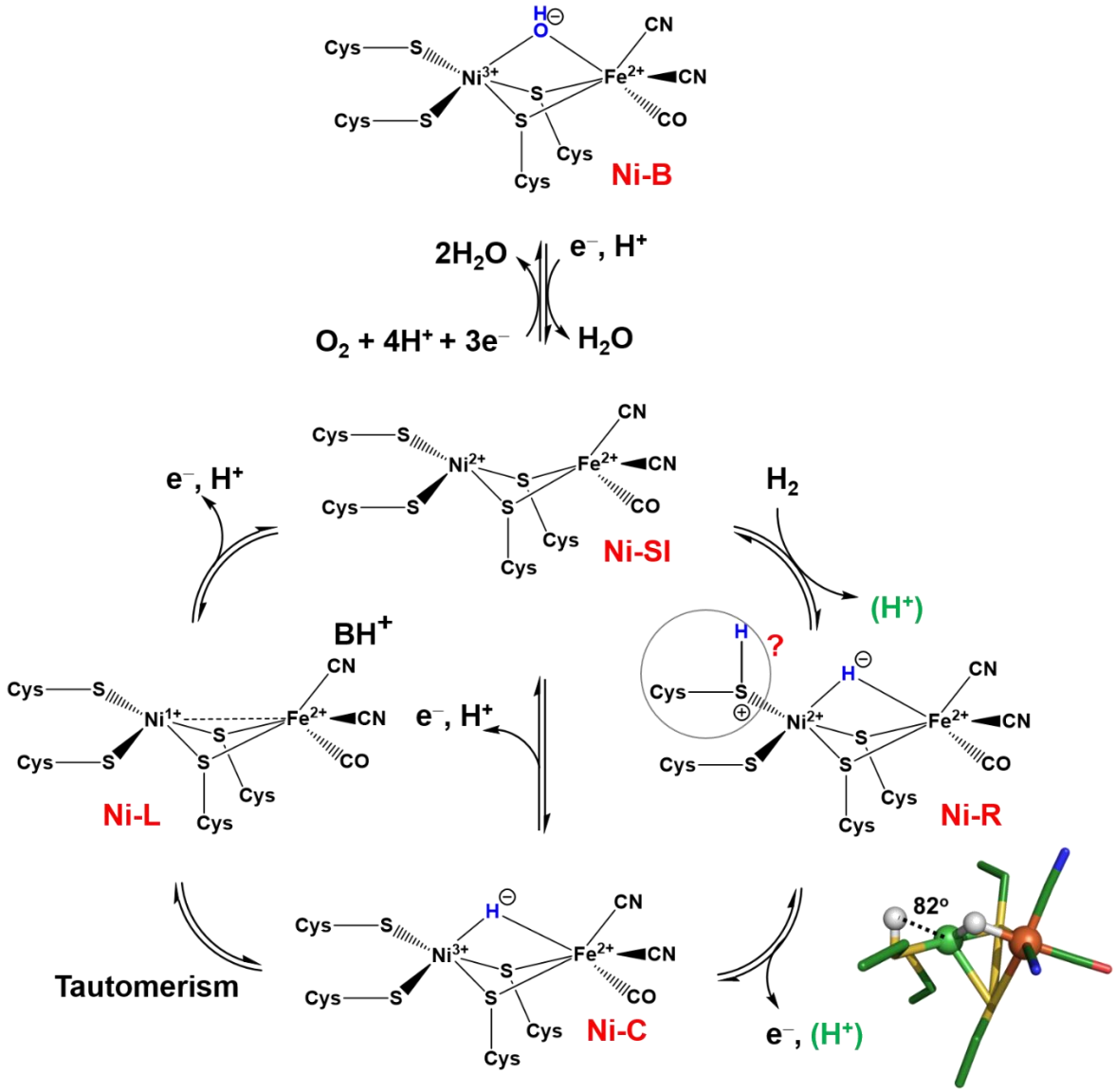


Figure 1.8: Catalytic Cycle of O_2-tolerant [NiFe]-hydrogenases. Reduction of Ni-B forms the Ni-SI state, which has no bridging ligand. Hydrogen binds in the vacant coordination site and is immediately activated by the NiFe active site and a local base. Electron density at one of the terminal cysteinate-S ligands in structure of the [NiFe]-hydrogenase from *Desulfovibrio vulgaris* Miyazaki F crystallized in the Ni-R state has been modelled as a proton (circled, also shown in stick and ball form)[81]. However, the Ni-S-H angle is 82° which brings this assignment into question. Thus, depending on the true structure of Ni-R, the first proton that formed by heterolytic splitting of H_2 could move to a local base at one of two points, indicated by the green protons: the Ni-SI to Ni-R transition (assuming Ni-R does *not* have a protonated cysteine) or the Ni-R to Ni-C transition (assuming Ni-R does have a protonated cysteine). Ni-C can then be oxidised to Ni-SI by *simultaneous* electron-proton transfer or via the Ni-L state using sequential proton and electron transfers. The latter would occur under conditions in which the proximal cluster is reduced.[86-87] In Ni-L, the proton has migrated to a base, the exact identity of which is unknown. Multiple Ni-L and Ni-R states are defined spectroscopically and it is expected that the proton is located at different position in each.

1.10 Mechanism of Hydrogen Activation

1.10.1 Kubas Mechanism vs. Frustrated Lewis Pairs

To design synthetic hydrogen catalysts, we must first understand how H_2 binds to and is activated by metal complexes. The first example of a transition metal-dihydrogen complex to be isolated was $W(CO)_3(P^iPr_3)_2(\eta^2\text{-}H_2)$ (Figure 1.9A) by Kubas *et al* in 1984;[89] prior to this, only dihydride complexes formed by the oxidative addition of H_2 to the metal centre had been isolated (Figure 1.9B).[90] X-Ray characterisation of the tungsten complex, however, by X-Ray crystallography revealed a H–H bond length of approximately 0.8 Å, a distance too short for it to exist as two hydride ligands. Since then, many stable transition metal-H_2 complexes have been characterised. To understand why in some instances H_2 binds stably to a transition metal and in other times is split to form two hydride ligands, we must consider *how* H_2 coordinates to metals.

Hydrogen binds through a combination of two interactions as shown in Figure 1.10. Firstly, there is σ-donation from the full bonding σ-bond of H_2 into an empty d-orbital of the metal centre. The second interaction is reminiscent of the Dewar-Chatt-Duncanson model of alkene-transition metal coordination in which the metal back donates electron density to the alkene π* orbital but is instead donated into the σ*-orbital of H_2. The back donation is

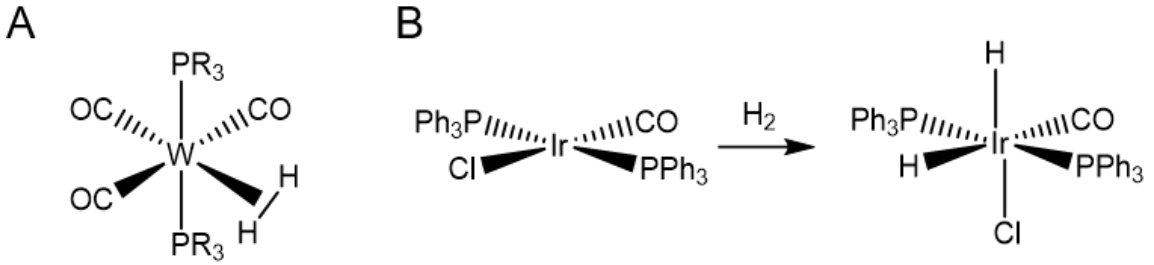


Figure 1.9: Example metal complexes with H_2 and dihydride ligands. A – Tungsten-H_2 complex, $W(PR_3)_2(CO)_3(\eta^2\text{-}H_2)$ where R = ^{i}Pr, characterised using X-Ray crystallography by Kubas *et al*. For more details see ref 89. **B** – Vaska's complex undergoes *reversible* oxidative addition of H_2 to form the cis-dihydride complex $Ir(CO)(Cl)(H)_2(PPh3)_2$, see ref 90.

necessary for stabilising the H_2 complex but is also important for H_2 cleavage.[22] In metal centres with increased electron density, for instance in complexes with strong σ-donor ligands, the back-donation interaction is stronger and, in the extreme case, the σ* orbital on H_2 becomes occupied. The H–H bond is cleaved *homolytically* as a result and a dihydride complex is formed; this process is oxidative cleavage and the oxidation state of the metal is increased by two. Conversely, replacing ligands with strong π-acceptors such as CO reduce back-donation to H_2 and the H–H bond remains intact.[22]

More recently, H_2 activation based on Lewis acid-base reactivity by main group elements has emerged. Typically, the reaction of a Lewis acid and base results in the formation of a neutral adduct; however, the use of Lewis acid and base pairs to activate hydrogen has been exemplified by the Stephan group by exploiting sterically demanding ligands on both the Lewis acid and base.[91-92] In such cases, bulky ligands prevent the formation of adducts and so the Lewis acidity/basicity remains unquenched. Such combinations are termed "Frustrated Lewis Pairs" (FLPs), and commonly employ group 3 elements, particularly boron, and group 5 elements, including nitrogen and phosphorus, as the Lewis acid and base, respectively. The first example of H_2 activation by an FLP used a catalyst that contained the Lewis acid and base in the same molecule (Figure 1.11).[93] Unexpectedly, this catalyst was capable of both H_2 cleavage and formation. Despite the initial proposal that this worked in an

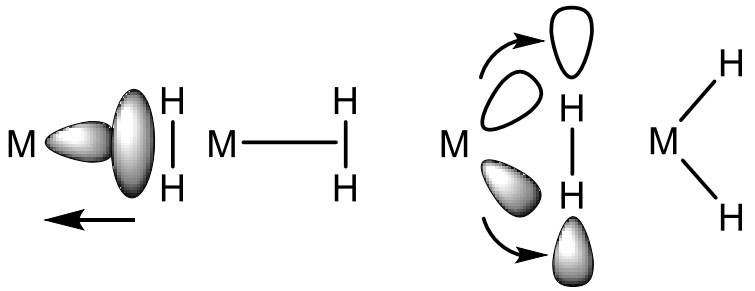


Figure 1.10: Bonding of dihydrogen (H_2) to a transition metal centre through σ-donation and back donation. H_2 donates electron density from the σ bond to empty d-orbitals on the metal. Electron density is then back donated from occupied metal based d-orbitals into the empty H_2 σ* star orbital. The extent of this back donation determines whether a M(η^2-H_2) or M$(H)_2$ complex is formed, refs 22, 90.

intramolecular fashion, it uses a bimolecular mechanism.[91] Since this pioneering work, many examples of FLPs have been published and the activity has been extended to include, for example, hydrogenation, alkene activation and reduction of CO_2.[91-92]

Hydrogen activation by FLPs occurs *heterolytically*, producing a hydride and a proton. Again, we consider the orbital interactions: the lone pair on PR_3 is donated to the σ*-orbital of H_2 in an 'end-on' manner with concomitant donation of the H_2 σ-bonding pair into the empty p-orbital of BR'_3 (Figure 1.12);[94] together these interactions destabilise and break the H–H bond, producing protonated phosphine and a hydride-borane.

1.10.2 [FeFe]-Hydrogenases and H_2 activation

For many years, the central bridgehead atom of the dithiolate bridge in the H-cluster was unknown. Seminal work published in 2013, however, revealed that a nitrogen in this position is crucial for activity.[40] A series of synthetic [FeFe] mimics with variable bridgehead atoms (N, O, CH_2) were used to reconstitute apo-HydA1, that is HydA1 containing only the [4Fe4S]

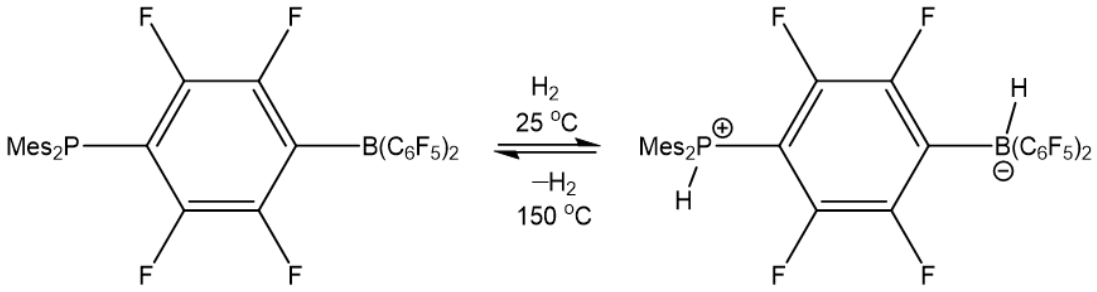


Figure 1.11: Reversible H_2 activation by $(Mes_2P)C_6F_4(B(C_6F_5)_2)$. $(Mes_2P)C6F_4(B(C_6F_5)_2)$ readily activates H_2 at ambient temperatures by a Frustrated Lewis Pair mechanism. The bulky Mes and C_6F_5 ligands prevent formation of the typical Lewis Acid-Base adduct between separate molecules. H_2 can be liberated from the zwitterionic species under heating. Mes is the Mesitylene or 1,3,5-trimethylbenzene group and C_6F_5 is pentafluorophenyl group. For more details refer to ref 92.

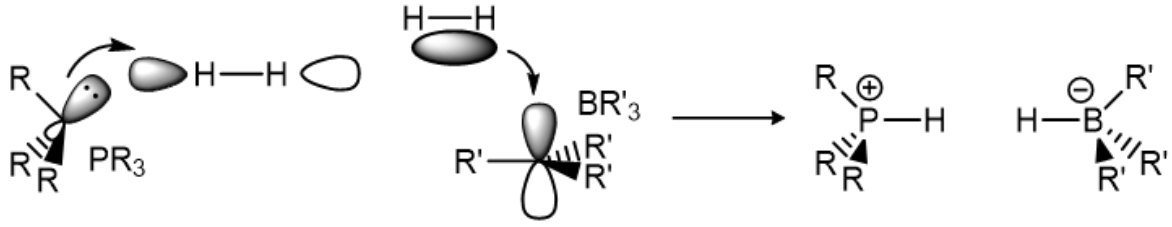


Figure 1.12: H_2 activation by a Lewis acid (BR'_3) and Lewis base (PR_3). The lone pair on the phosphine is donated to the σ* orbital of H_2. Concomitant donation of the σ(H_2) electrons to the empty borane orbital results in heterolytic cleavage of H_2 to form a protonated phosphine and a borane-based hydride.[94]

cluster and no [FeFe] site. However, only the mimic containing a N bridgehead (referred to as $[2Fe]^{mim}$) produced fully active enzyme.[40, 95] This nitrogen is optimally placed above the distal Fe to act as a base in the heterolytic splitting of bound H_2 using a mechanism reminiscent of H_2 splitting by FLPs (Figure 1.13). However, 'free' $[2Fe]^{mim}$ (non-protein bound) was inactive in H_2 production and oxidation, a result which demonstrates the importance of both the Fe-S cluster and wider protein scaffold.

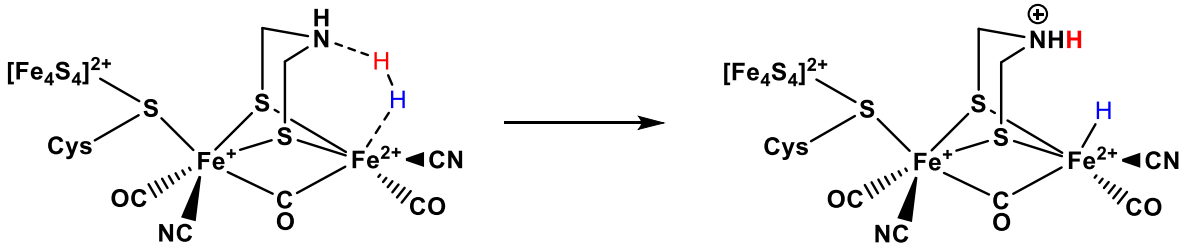


Figure 1.13: H_2 activation by [FeFe]-hydrogenases using a pendent amine base. Hydrogen is split by [FeFe]-hydrogenases to form a proton, which resides on the pendent N bridge head atom, and a hydride on the distal Fe in an FLP-like mechanism. Refs 40, 95.

1.10.3 Hydrogenase Model Catalysts

It is unlikely that hydrogenases will be used directly in H_2 technology (Section 1.3). Instead, it is more likely that synthetic catalysts will be used and since the publication of hydrogenase crystal structures many model compounds have been synthesised. Early examples resembled the NiFe active site, and contained both the Ni-thiolate groups and Fe-CO (CN) groups (Figure 1.14A) but had limited or no activity.[5, 96] Complexes produced by Ogo *et al*, however, exhibit H_2 oxidation activity: both a NiRu complex[97] and a NiFe complex[98] activated H_2 to form a metal-hydride complex (Figure 1.14B & C). Although the Ni(H)Ru complex was inactive in H_2 evolution, H_2 was liberated from the NiFe complex when treated with strong acid.

Some of the most successful catalysts for H_2 activation come from the groups of DuBois and Shaw at the Pacific Northwest National Laboratory (PNNL). These catalysts contain only a single metal site (Ni) coordinated by diphosphine ligands with bridging amines ($P^R_2N^{R'}_2$)

and the first example of a $[Ni(P^{R}_{2}N^{R'}_{2})_2]^{2+}$ complex (referred to as Cy) showed a turnover frequency (TOF) of over 100,000 s^{-1} for H_2 production in an acetonitrile/water mix.[99] Despite containing a single Ni ion, the mechanism of these catalysts mimics that of the [FeFe]-hydrogenases, with the amines acting as pendent bases in H_2 activation (Figure 1.14D). Although this group of catalysts now includes those with H_2 oxidation activity, these catalysts are not bidirectional. Hydrogenases, and indeed other enzymes, do not rely on their active sites alone for catalytic activity but have a protein scaffold which enables transport of substrate/product, electrons and protons to/from the active site.

The group of Shaw *et al* has been expanding the portfolio of Cy complexes by including a second coordination sphere. To mimic the protein scaffold, the group have produced a series of catalysts containing an amino acid (CyAA) or dipeptides on the amine groups (Figure 1.15). Cy catalysts containing phenylalanine (CyPhe)[33] and arginine (CyArg),[100] show reversibility and fast turnover frequencies in methanol and water, respectively. It was

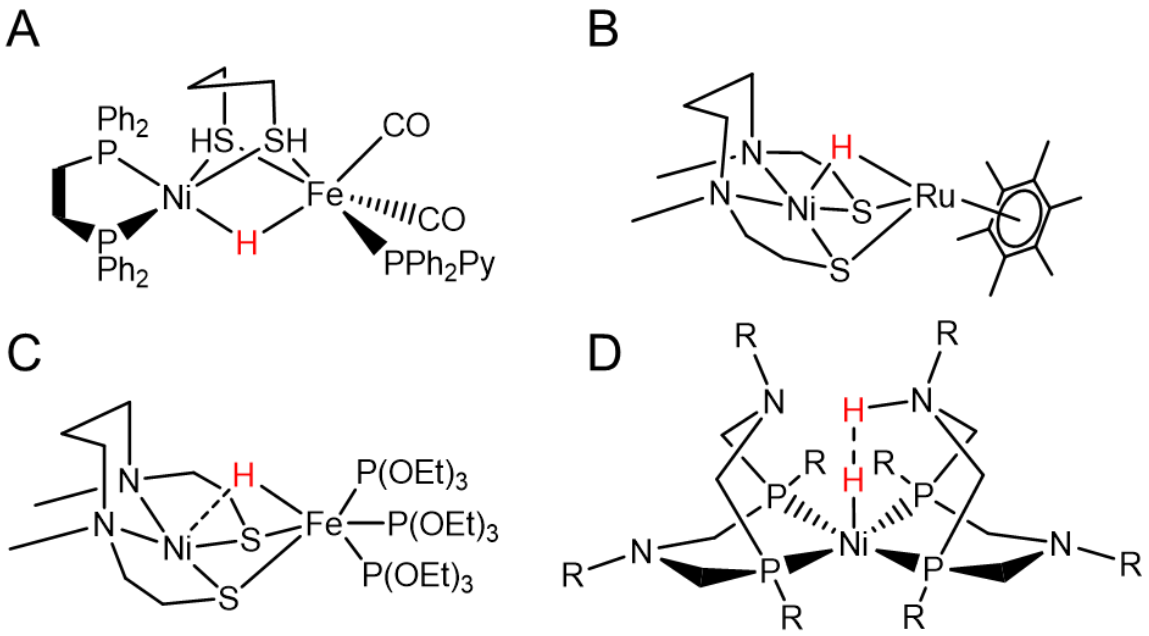


Figure 1.14: Hydrogenase model compounds. A – mimic by Barton and Rauchfuss which is active in H_2 evolution.[96] **B** – NiRu catalyst by Ogo *et al* which irreversibly activates H_2 at ambient temperatures.[97] **C** – [NiFe] mimic by Ogo *et al* reversibly activates H_2 in the presence of a strong base (oxidation) or acid (evolution).[98] **D** – generic structure of $[Ni(P^{R}_{2}N^{R}_{2})_2]^{2+}$ catalysts by the DuBois and Shaw groups showing H_2 is activated using an FLP-like mechanism, first described in ref 99.

concluded that interactions between the side chains stabilise the structure, resulting in an optimum Ni-N distance for H_2 addition. Aspartate (Asp), lysine (Lys) and serine (Ser) and dipeptides GlyPhe (Gly is glycine), PheGly and AspPhe were also added to the Cy catalyst.[101] Of all six of these complexes, the most promising catalysts with fast rates and low overpotentials are those that have Phe or a COOH group at the first amino acid in the sequence, i.e. Cy(PheGly) Cy(AspPhe) and CyAsp. As with CyPhe and CyArg, interactions between the amino acid side chains are expected to stabilise the structure in CyAsp and the additional COOH group is also believed to be involved in proton movement.[101] Although they had better rates than the complexes containing the same first amino acid, none of the dipeptides exhibited reversibility at room temperature, suggesting that the free COOH group in the CyAA complexes, which is replaced by an amide in the dipeptides, is crucial for achieving reversibility.[101] The ongoing work by Shaw demonstrates the importance of the second and outer coordination spheres in catalysts, biological or otherwise.

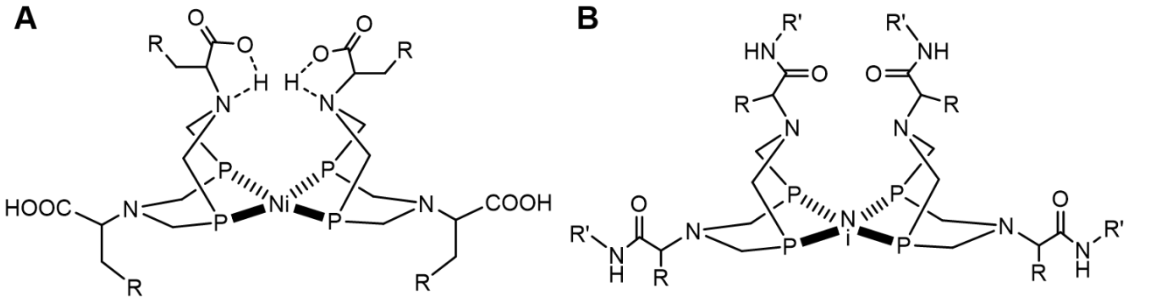


Figure 1.15: General structure of Cy complexes with amino acid or dipeptides. A – Structure of CyAA complexes. R groups of CyAsp, CyLsy and CySer are indicated. **B** – Structure of dipeptide complexes. R and R' groups are indicated for Cy(GlyPhe), Cy(PheGly) and Cy(AspPhe). Described in ref 101.

1.10.4 [NiFe]-Hydrogenases

There is agreement about the catalytic cycle of [NiFe]-hydrogenases but the identity of the base required for H_2 activation has been the subject of discussion for many years. One of the terminal Ni-cysteine residues has been assumed to fulfil this role.[5] Although a crystal structure of *Dv*MF in the Ni-R state includes a protonated cysteine,[81] this assignment may not be correct (Section 1.9). Additionally, synthetic catalysts containing Ni thiolates have not been shown to be good catalysts for H_2 activation (Section 1.10.3).

The initial sequence alignment of twelve O_2-sensitive and O_2-tolerant [NiFe]-hydrogenases revealed a strictly conserved arginine (R509 in Hyd-1);[48] further alignment of all hydrogenases (including putative sequences), indicated this arginine is present in all but one hydrogenase.[47] The guanidinium side chain of R509 is suspended approximately 4.5 Å above the Ni active site (Figure 1.16), a distance suitable for H_2 activation by an FLP

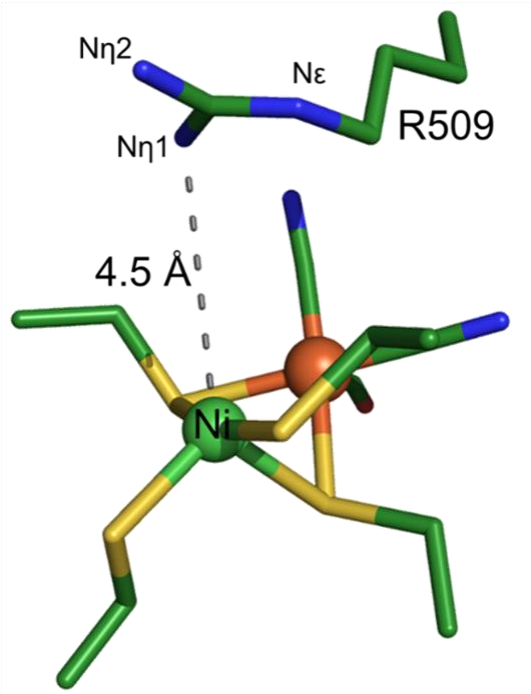


Figure 1.16: The conserved arginine (R509) in [NiFe]-hydrogenases, shown in *Ec*Hyd 1. The guanidinium headgroup of R509 is suspended above the Ni-Fe active site such that the Nη1 is 4.5 Å from the Ni. Only the guanidinium side chain of R509 is shown. In this structure, Hyd-1 was aerobically purified and so crystallised in the 'as isolated' state. Thus, the active site was in the Ni-B state. The oxygen ligand has been removed computationally using PyMOL to ensure the Ni-R509 distance is clear. PDB: 5A4M

mechanism. The H_2 oxidation activity of a Hyd-1 variant R509K was only 1% of native Hyd-1.[48] Previous attempts to make R509 variants in *Thiocapsa rosepersicina*[51] and *Desulfovibrio fructosovorans*[102] produced immature or no enzyme, respectively. As a result, the role of R509 has been proposed to be in forming and stabilising the active site, for example through hydrogen bonds with one of the CN^- ligands. However, the angle between the Fe-CN ligand and the Nη of R509 is not optimised for a hydrogen bonding (the most stable H-bonding interactions for HCN are linear, i.e. C≡N$^-$···H-X).[103] A crystal structure of *Ec*R509K showed that the variant was fully matured and the active site could be superposed on native Hyd-1,[48] so the resulting decrease in H_2 oxidation activity is not due to purification of immature protein but suggests a more significant role for R509 in H_2 activation.

A catalytic base must be able to cycle between the protonated and deprotonated states, and so arginine is typically not considered to be a good base due to the high pK_a (12.5)[104] of the free amino acid, which suggests it would be permanently protonated at physiological pH. However, it is recognised that the pK_a of amino acids within a protein structure may be perturbed when compared with their free pK_a values. Although rare, this is not the first example of an arginine in catalysis. For example, arginine functions as a base in pectate/pectin lyases and fumarate reductase,[105] and arginine appears to have a role in Photosystem II.[106] In [NiFe]-hydrogenases, the metal hydride is expected to be sufficiently basic and thus be capable of deprotonating arginine during H_2 evolution as Ni-H complexes typically have pK_as in the range 10 – 26.[107-108]

Eyring analyses and kinetic isotope experiments lent further support to the proposal that R509 is the catalytic base in H_2 activation.[47] The activation enthalpy ($\Delta H^‡$) for H_2 oxidation is more favourable for R509K than native Hyd-1 and consequently the reduction in rate is due to the significantly less favourable activation entropy ($\Delta\Delta S^‡$ of –52 J K^{-1} mol^{-1}). The less favourable $\Delta S^‡$ may be explained by increased flexibility of the lysine side chain compared

with arginine, as seen in the temperature factor analysis of the crystal structures. The H_2/D_2 kinetic isotope effect (KIE) for Hyd-1 and R509K were measured to be 1.4 and 1.1 at pH 6 and 0 V (*vs*. SHE), respectively. Whilst these values indicate that H–H is not the rate determining step, they may reflect the differences in the pK_as of free arginine and lysine (10.5):[104] assuming a mechanism in which residue 509 is the base in H_2 splitting, deprotonation of the base is required before the next catalytic cycle begins; given the lower pK_a, this deprotonation should be less rate-limiting for lysine. This explanation is also fitting with the lower $\Delta H^{\ddagger}$ observed for R509K. It should be noted that R509K had the same response to O_2 and CO as native Hyd-1.[47]

1.11 Topics addressed in this thesis

This thesis addresses the importance of conserved residues close to the active site in Hyd-1. Chapter 3 focuses on the role of conserved aspartates, D118 and D574, which form a 'canopy' above the active site with the crucial R509. This includes a detailed exploration of the fundamental properties of Hyd-1 and canopy variants, including the steady state H_2 oxidation turnover frequency, the Michaelis constant and O_2-tolerance. Additionally, crystal structures of two variants, D574N and D118N/D574N have been produced. Chapter 4 explores the role of the highly conserved glutamate E28. This residue has been shown to have a role in proton transfer but PFE experiments with two variants E28D and E28Q described here indicate that the role of this residue is more complex.

2 Experimental Methods and Theory

2.1 Solutions

All solutions were prepared using distilled water for enzyme purification or ultrapure water (Millipore, 18 MΩ cm) for Protein Film Electrochemistry, EPR spectroscopy and solution assays.

2.2 Molecular Biology Methods

2.2.1 Strains, Plasmids and Oligonucleotide Primers

Strains used in this work were produced by Emily Brooke (EJB), Dr Rhiannon M. Evans (RME) or Matthew Fisher (MF), detailed in Table 2.1. Plasmids used in the pMAK cycle (Section 2.2.4) are detailed in Table 2.2. Oligonucleotide primers used in Polymerase Chain Reactions (Section 2.2.3) are presented in Table 2.3. All primers were purchased from Invitrogen (Thermo Fisher Scientific).

Table 2.1: Strains used in this research

Strain	Description	Source/Made by
DH5α	High Efficiency Cloning strain.	New England Biolabs. These are commercially purchased, competent cells for DNA cloning. They were also used as a stock for competent cells made in-house.
FTH004	MC4100 with *hyaA* his_6 tag	Ref 7
RMESW014	As FTH004, *hyaB* D118A	RME
RME011	As FTH004, *hyaB* R509K	RME
EJB001	As FTH004, *hyaB* D574N	EJB
MF002	As FTH004, *hyaB* D118N	MF This was used solely to make the strain EJB002
EJB002	As FTH004, *hyaB* D118N/D574N	EJB
EJB003	As FTH004, *hyaB* D118E	EJB/RME
EJB004	As FTH004, *hyaB* D118V	EJB/RME
RME017	As FTH004, *hyaB* E28D	RME
RME018	As FTH004, *hyaB* E28Q	RME

Table 2.2: Plasmids used in this research. 'Cam^R' is resistance to chloroamphenicol, 'ori' is the origin of replication.

Plasmid	Description	Source/Made by
pMAK-hyaB-WT	From pMAK705. Cam^R, temperature sensitive Ori, carries native *hyaB* with 500 bp flanks	F. Sargent
pMAK-hyaB-D574N	Cam^R, temperature sensitive origin of replication, carries *hyaB* D574N with 500 bp flanks	EJB
pMAK-hyaB-D118V	Cam^R, temperature sensitive origin of replication, carries *hyaB* D118V with 500 bp flanks	EJB/RME
pMAK-hyaB-D118E	Cam^R, temperature sensitive origin of replication, carries *hyaB* D118E with 500 bp flanks	EJB/RME

Table 2.3: Oligonucleotide Primers used in this research

Primer name	Sequence 5'- → -3'	Function
HyaB_D574N_F	GTACTCTGCACAGCTTTAACCCGTGCCTCG CCTGTTC	Forward primer for mutation of D574 to Asn
HyaB_D574N_R	GAACAGGCGAGGCACGGGTTAAAGCTGTG CAGAGTAC	Reverse primer for mutation of D574 to Asn
HyaB_D118V_F	CTGGCAACGCTCTGGTGCCACGTGCATCT GGTGCACTTC	Forward primer for mutation of D574 to Val
HyaB_D118V_R	GAAGTGCACCAGATGCACGTGGCACCAGA GCGTTGCCAG	Reverse primer for mutation of D574 to Val
HyaB_D118E_F	CTGGCAACGCTCTGGTGCCACGAACATCT GGTGCACTTC	Forward primer for mutation of D574 to Glu
HyaB_D118E_R	GAAGTGCACCAGATGTTCGTGGCACCAGA GCGTTGCCAG	Reverse primer for mutation of D574 to Glu
pMAK_overlap_F	CGGTCCAATGATCGAAGTTAGGCTGGTAA GAGCCG	Primer to linearise pMAK plasmid for Gibson
pMAK_overlap_R	CGGCTCTTACCAGCCTAACTTCGATCATTG GACCG	Primer to linearise pMAK plasmid for Gibson
hyaB_F	TATTGAATTCGCGCCATCATTACTTACATG GTGACCTTTG	Forwards primer for colony PCR of hyaB gene
HyaB_R	TATTGAATTCCGGCGCAAAAATAGCGTACT GGCTGTGTTCGC	Reverse primer for colony PCR of hyaB gene

2.2.2 Cell Growth and Culture

Culture Medium and Antibiotics for Cell Growth

Cells were grown in Lysogeny Broth (or Luria-Bertani medium, LB. A pre-made mixture was purchased from Melford and prepared to a concentration of 25 g L^{-1} in distilled water, giving final concentrations of 10 g L^{-1} tryptone, 5 g L^{-1} yeast extract and 10 g L^{-1} sodium chloride. All LB was autoclaved prior to use. Solid media plates were made using the same LB medium, and agar (Melford) was added to a concentration of 2% (w/v) prior to autoclaving. Where required, chloroamphenicol (Cam, Duchefa Biochemie, > 98%) was used at a final concentration of 25 μg mL^{-1} from a stock solution of 25 mg mL^{-1} in 100 % ethanol. Resulting mixtures are referred to as LB/Cam25.

Glycerol Stocks

All strains produced for this thesis were preserved as glycerol stocks using the following protocol. A single colony was used to inoculate 5 mL of LB medium and grown at 37 ^{o}C with shaking. After 16 hours, the cells were harvested by centrifugation at 4 ^{o}C for 10 minutes at 3000xg. The supernatant was removed and the cell pellet was resuspended in 50% (v/v) glycerol (Thermo Fisher Scientific), which was prepared with distilled water and autoclaved before use. The cell suspension was flash frozen in liquid N_2 and stored at −80 ^{o}C.

All plasmids were also preserved in DH5α cells as glycerol stocks. A single transformant was picked into LB/Cam25 and grown at 30 ^{o}C with shaking overnight. The cell pellet was harvested and preserved in glycerol as described above.

2.2.3 Methods for Genetic Engineering

Preparation of Competent Cells

For transformations using DNA from Gibson Assembly (page 40), DH5α purchased from New England Biolabs (NEB) were used (Table 2.1). In all other cases, competent DH5α or FTH004 were prepared in-house using the RbCl method detailed below.

LB medium (5 mL) was inoculated with a single colony and grown overnight at 37 °C with shaking. This culture (50 μL) was used to inoculate fresh LB medium (50 mL) and grown to an OD_{600nm} of 0.4 to 0.6 in a sterile conical flask. This culture was incubated on ice for 30 minutes before harvesting the cells by centrifugation at 4 °C for 10 minutes at 3000 xg. The cell pellet was resuspended in buffer TFB I (Table 2.4) and incubated on ice for a minimum of 15 minutes. The cells were harvested using a further centrifugation step and resuspended in buffer TFB II. Finally, the cell suspension was incubated on ice for 15-30 minutes before flash freezing in liquid N_2 in 50 μL aliquots, which were stored at −80 °C.

Table 2.4: Buffers for preparation of competent cells using RbCl methods. Buffers were prepared using distilled water and were filtered sterilised before use. Chemicals were purchased from Melford, Sigma Aldrich and Thermo Fisher Scientific.

Buffer Name	Composition
TFB I	30 mM potassium acetate (KOAc), 100 mM RuCl, 10 mM CaCl, 50 mM $MnCl_2$, 3 mM hexamminecobalt(III) chloride, 15% (v/v) glycerol
	pH adjusted to 5.8 using acetic acid
TFB II	10 mM MOPS, 10 mM RuCl, 75 mM CaCl, 15% (v/v) glycerol
	pH adjusted to 6.5 using KOH

Transformation of Plasmid DNA

All plasmids used were derived from the pMAK705 plasmid, which contains a temperature-sensitive origin of replication and thus replicates only at 30 °C. Unless otherwise stated, 1 μL of plasmid DNA was added to 50 μL of competent cells. The cell-DNA mixture

was incubated on ice for 30 minutes before being 'heat shocked' in water at 37 °C for 30 s and subsequently incubated on ice for 2 minutes. LB medium (1 mL) was added and the transformed cells allowed to recover at 30 °C with shaking. After 1.5 hours, the culture was centrifuged at 5223xg for 5 minutes, and most of the supernatant removed, leaving approximately 100 μL. The cell pellet was resuspended in the remaining LB medium and spread onto an LB/Cam25 agar plate to select for transformants. The plate was grown at 30 °C for 16 hours and stored at 4 °C when not in use.

Polymerase Chain Reaction for Site Directed Mutagenesis

The Polymerase Chain Reaction (PCR) is a method for amplifying DNA and can be used to introduce point mutations. Typically, this is achieved using 'quick change' PCR in which a plasmid is amplified using a set of complementary primers containing the mutation. When using this method to introduce mutations to pMAK plasmids, there were problems with non-specific annealing resulting in a mixture of PCR products. Instead a protocol using the 'Gibson Assembly' method[109], which is used to assemble two or more fragments of linear DNA with overlapping ends, was optimised.

For pMAK-hyaB-variant plasmid, two sets of primers were used (Table 2.3) to create linear fragments from the pMAK-hyaB-WT plasmid as shown in Figure 2.1, each containing the mutation at one end. The reaction mixture and method are outlined in Table 2.5 and Table 2.6, respectively. High-fidelity polymerase Q5 (NEB) was used to minimise random mutations generated during PCR. Gel electrophoresis (page 39) was used to determine whether fragments of the correct size were generated (Figure 2.2). A restriction digestion with DpnI (NEB) was then used to digest template DNA: DpnI (1 μL) was added to the PCR mixture and incubated at 37 °C. After 8 hours, DpnI was heat inactivated by incubating at 80 °C for 20 minutes to prevent 'star activity' (non-specific cutting). Following PCR Purification or gel

extraction (page 39-40), Gibson Assembly (page 40-41) was used to produce an intact plasmid containing the mutation.

Table 2.5: Reaction mixture for a 50 μL PCR using Q5 polymerase. The Reaction Buffer and GC Enhancer were supplied with the Q5 polymerase (NEB). dNTPs were also supplied by NEB. In some cases, 100 μL reactions were used to increase the DNA concentration. The component volume was doubled, except for template DNA which was always 0.5 μL.

Reaction Component	Volume / μL	Final Concentration / μM
Reaction Buffer (5x)	10	1x
GC Enhancer (5x)	10	1x
Deoxynucleotides (dNTPs) (10 mM each)	1	200
Template DNA	0.5	–
Forward Primer (10 μM)	2.5	0.5
Reverse Primer (10 μM)	2.5	0.5
Q5 Polymerase (2 units μL^{-1})	0.5	0.02 (units μL^{-1})
Ultrapure water	23	–

Table 2.6: Thermocycling conditions for PCR for Site-Directed Mutagenesis with Q5 Polymerase.

Step	Temperature / °C	Duration / s
Initial Denaturation	98	30
Amplification:		35 Cycles
Denaturation	98	30
Primer Annealing	62	30
Extension	72	30 s per kb
Final Extension	72	240

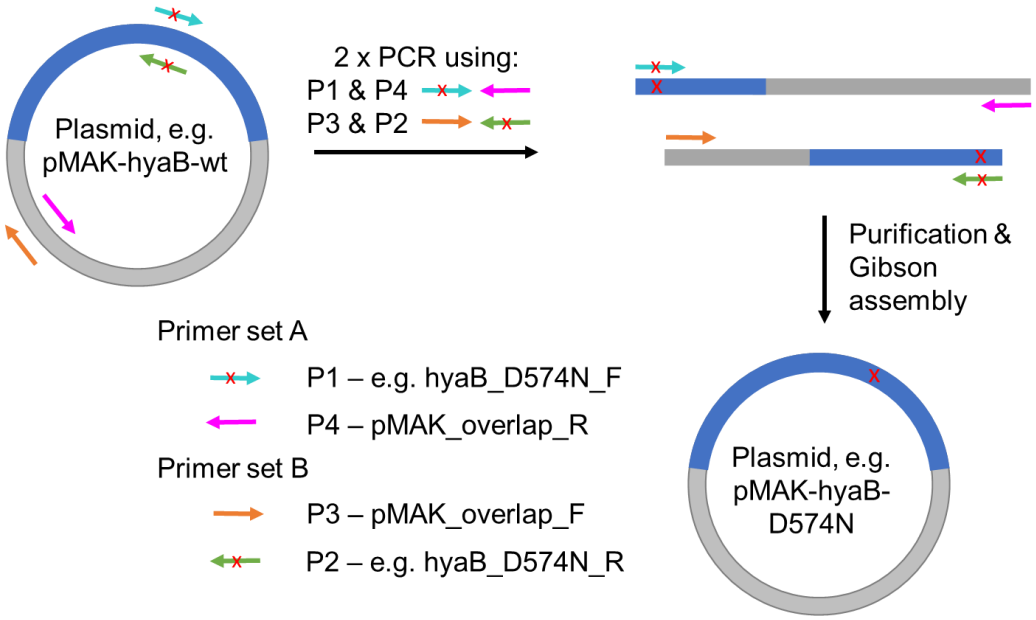


Figure 2.1: PCR to generate two linear fragments from plasmid DNA. The plasmid (pMAK-hyaB-wt) is linearised using two sets of primers (A and B). The fragments have complementary ends and each contains the mutation (marked with an X) at one end. Following PCR, the fragments are purified and Gibson assembly is used to create an intact plasmid containing the mutation.

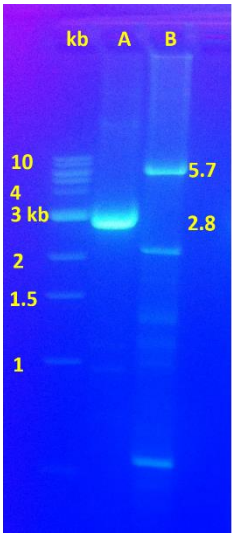


Figure 2.2: Agarose gel showing fragments of pMAK hyaB following PCR. Two PCR reactions (A and B) were run simultaneously with the plasmid pMAK-hyaB-wt and two different sets of primers: A – hyaB_D574N_F and pMAK_overlap_R; B – hyaB_D574N_R and pMAK_overlap_F. Length of desired products indicated on the right. Note that B has some additional products from non-specific annealing of primers. The ladder is shown on the left, and the length of DNA markers are indicated. 1% agarose gel, run for 60 mins at 100 mV.

Agarose Gel Electrophoresis

Agarose gel electrophoresis was used for DNA visualisation and separation of multiple PCR products (Figure 2.2). Agarose gels were prepared using 1% (w/v) agarose (Melford) dissolved in 1x TAE buffer (Table 2.7). RedSafe Nucleic Acid Staining Solution (20,000x, Intron Biotechnology) was added for visualisation of DNA under a UV lamp. A 1 kb DNA ladder (NEB) was used to quantify the size of PCR products and a Gel Loading Buffer (NEB) was used to load samples. Typically, 5 μL of reaction mixture was run on a gel, although prior to gel extraction the entire reaction mixture was loaded. Gels were electrophoresed at 100 mV for 20-60 minutes, depending on the size of the gel.

Table 2.7: Buffer used in agarose gel electrophoresis for DNA separation. Chemicals bought from Melford or Thermo Fisher Scientific.

Buffer Name	Buffer Composition
50x TAE Buffer	2 M Tris-HCl, 1 M acetic acid, 50 mM EDTA

PCR Purification

PCR purification was used to purify the PCR product from the reaction mixture. PCR Purification was carried out according to the Quiagen QIAquick PCR purification method. Buffers for this were made in-house (Table 2.8). PCR products were typically purified into 12-20 μL autoclaved ultrapure water.

Table 2.8: Buffers used in PCR Purification using Quiagen QIAquick Method. Components supplied by Melford or Fisher Chemicals

Buffer Name	Composition
PB	5 M guanidine hydrochloride, 20 mM Tris-HCl, 38% (v/v) ethanol pH adjusted to 6.6 using HCl
PE	10 mM Tris-HCl, 80% (v/v) ethanol, pH adjusted to 7.5 using HCl

Gel Extraction

When multiple products are produced during PCR, for example due to non-specific annealing of primers, a specific product can be extracted and purified from an agarose gel. 'Gel extraction' of linear DNA was performed using the Quiagen QIAquick gel extraction method. Again, the buffers were made in-house (Table 2.9). Gel extracted PCR products were typically purified into 12-20 μL autoclaved ultrapure water.

Table 2.9: Buffers for Gel Extraction of PCR products. Chemicals supplied by Melford.

Buffer Name	Composition
QG	5.5 M guanidine thiocyanate, 20 mM Tris-HCl pH adjusted to 6.6 using HCl
PB	As Table 2.8
PE	As Table 2.8

Gibson Assembly

Gibson assembly was used to create an intact pMAK plasmid containing a mutation on the *hyaB* gene. The reaction mixture (Table 2.10) was prepared using a Gibson Assembly 'Mastermix' (NEB) containing an exonuclease, a polymerase and ligase, and held at 50 ^{o}C for 4 hours. 4 μL of reaction mixture was added to 50 μL of competent DH5αs (NEB), heat shocked at 37 ^{o}C for 30 s, and allowed to recover for 4 hours at 30 ^{o}C in SOC medium (NEB). The cells were plated on LB/Cam25 agar to select for transformants. Typically, a small number of colonies were seen only after 24-48 hours growth following Gibson Assembly.

Table 2.10: Reaction mixture for Gibson Assembly. Mastermix supplied by NEB.

Reaction Component	Volume / μL
Linear DNA fragment A	1
Linear DNA fragment A	1
Gibson Assembly Mastermix	3
Ultrapure water	1

'Mini-Prep' Purification of Plasmid DNA

Following transformation, a single colony was used to inoculate 5 mL of LB/Cam25 medium and grown for a minimum of 16 hours at 30 °C with shaking. The cells were harvested by centrifugation for 10 minutes at 3000xg. Plasmid DNA was then extracted and purified using the Quiagen QIAquick Mini-prep kit and purified into 30 μL autoclaved ultrapure water. Buffers were made in-house (Table 2.11).

Table 2.11: Buffers for DNA purification by mini-prep. Chemicals supplied by Melford or Thermo Fisher Scientific.

Buffer Name	Composition
P1	50 mM Tris-HCl, 10 mM EDTA, 100 μg mL^{-1} RNase A pH adjusted to 8 using HCl
P2	0.2 mM NaOH, 1% sodium dodecyl sulfate (SDS)
N3	4 M guanidine hydrochloride, 0.5 M KOAc pH adjusted to 4.2 using glacial acetic acid
PB	As Table 2.8
PE	As Table 2.8

Sanger Sequencing of DNA

Plasmids and colony PCR products were checked for mutations using Sanger Sequencing provided by Source Bioscience. The concentration of purified DNA was determined using a nanodrop spectrophotometer and was diluted using ultrapure water as required.

2.2.4 The pMAK cycle

The complexity of [NiFe]-hydrogenase maturation requires that mutations are made on the chromosome (which subsequently encode amino acid substitutions), rather than a high copy number plasmid for gene overexpression. The pMAK705 plasmid provides resistance to Cam and the free plasmid will only replicate at 30 °C. However, when grown at 44 °C, the pMAK705 plasmid can undergo homologous recombination with the chromosome, which allows it to replicate. Subsequent growth at 30 °C 'cures' the plasmid. Thus, a series of recombination and resolution events (the 'pMAK cycle') governed by temperature/antibiotic control can, therefore, result in the mutation being made on the chromosome (Figure 2.3) if the recombination events occur at appropriate locations.[110]

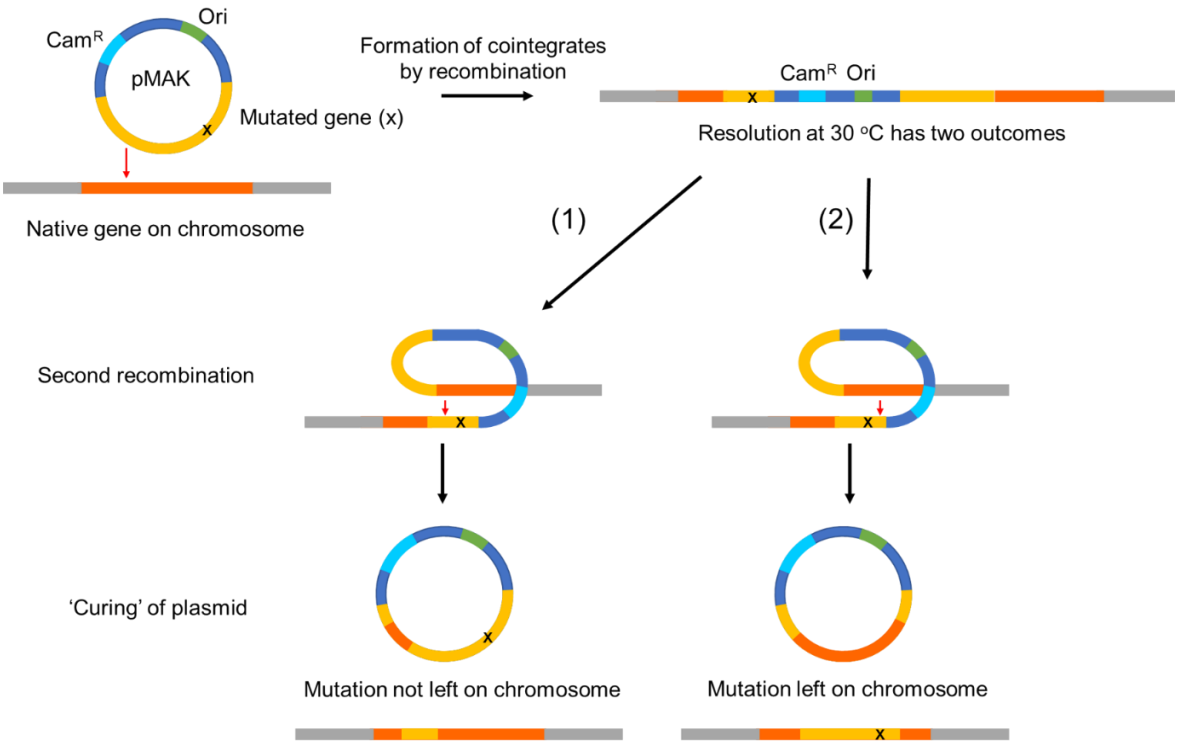


Figure 2.3: Recombination events leading to introduction of a mutation from a free plasmid onto the chromosome of *E. coli*. The first recombination event by growing at 44 °C results in the formation of cointegrates. A second recombination results in 'curing' of the plasmid and has one of two possible outcomes: (1) the free plasmid contains the mutation or (2) the mutation remains on the chromosome.

The pMAK cycle

At all stages, bacterial cultures were grown with shaking. The desired *E. coli* strain was made competent using RbCl method, e.g. FTH004 (Table 2.1). Every following step was performed in duplicate, so where it says a single colony was picked, for example, two were picked to increase the chance of success. The competent cells were transformed with the mutated pMAK-hyaB plasmid (Table 2.2) using the method outlined in Section 2.2.3, page 35) and grown overnight at 30ºC. A single colony into 5 mL LB/Cam25 and grown overnight at 30 ºC. The overnight culture was used to produce 'serial dilutions', for isolation of single colonies, as follows: 100 μL of overnight culture was mixed with 900 μL of fresh LB (the '1^{-1}' solution); the 1^{-1} solution was mixed thorough mixed, and 100 μL mixed with 900 μL fresh LB (the '1^{-2}' solution); the dilution was carried down the line to produce '1^{-3}' to '1^{-7}' solutions. The 1^{-3}, 1^{-4}, 1^{-5} and 1^{-7} dilutions were plated on LB/Cam25 agar plates. The 1^{-3}, 1^{-4} and 1^{-5} plates were grown at 44 ºC and the 1^{-7} plate at 30 ºC (control plate). After confirming there was growth on the 1^{-7}, the plate was discarded. Three lots of LB/Cam25 (10 mL) were prepared in sterile falcon tubes and 4 colonies used to inoculate each falcon tube. The colonies were picked from a combination of the 1^{-3}, 1^{-4} and 1^{-5} plates, and the cultures were grown at 30 ºC overnight. Each culture (10 μL) was used to inoculate 10 mL fresh LB/Cam25 and grown overnight at 30 ºC. After 16 hours, each culture was used to streak for single colonies on LB/Cam25 agar plates, which were grown overnight at 30 ºC. A single colony from each plate was used to inoculate 10 mL LB and the culture grown overnight at 44 ºC. Again, this colony was used to streak for single colonies on LB agar plates and overnight at 44ºC. A minimum of 25 single colonies were replica patched onto onto LB only and LB/Cam25 agar plates and grown overnight at 30 ºC. Colony PCR (page 44) was used to produce DNA to be sent for DNA sequencing (page 41). Once mutation on chromosome was confirmed, a glycerol stock was made from the positive colony.

‘Colony’ Polymerase Chain Reaction for DNA sequencing

Colony PCR uses a colony suspension as the template to produce a PCR product directly from the chromosome. A single colony was suspended in 100 μL autoclaved ultrapure water. The PCR reaction mixture and thermocycling conditions are detailed in Table 2.12 and Table 2.13, respectviely. The polymerase Taq (Invitrogen) was used. The PCR product was run on an agarose gel to ensure it was the correct size, and then PCR purified or gel extracted before sending for sequencing.

Table 2.12: Reaction mixture for a 60 μL PCR using Taq polymerase. The Reaction Buffer, Magnesium Chloride and W1 Detergent were supplied with the Taq polymerase from Invitrogen. dNTPs were supplied by NEB.

Reaction Component	Volume / μL	Final Concentration / mM
Reaction Buffer (10x)	6	1x
Magnesium Chloride (50 mM)	1.8	1.5
W1 Detergent (1%)	3	0.05 %
Deoxynucleotides (dNTPs) (10 mM each)	1	0.17
Template	1-4	–
Forward Primer (100 μM)	1	1.7
Reverse Primer (100 μM)	1	1.7
Taq Polymerase (5 units μL^{-1})	0.6	0.05 (units μL^{-1})
Ultrapure water	To 60 μL	–

Table 2.13: Thermocycling conditions for colony PCR with Taq Polymerase.

Step	Temperature / ^{o}C	Duration / s
Initial Denaturation	95	300
Amplification:		35 Cycles
Denaturation	95	30
Primer Annealing	50	30
Extension	72	30 s per 500 bp
Final Extension	72	420

2.3 Purification of Hydrogenase-1

2.3.1 Aerobic Isolation

All buffers used in purification are listed in Table 2.14. Hyd-1 was purified from the FTH004 strain, or relevant variant strain (Table 2.1). All strains were modified at *hyaA* to contain a His_6 affinity tag at the C-terminus. The cells were grown in 6 L cultures prepared as so: a single colony (per 6 L to be grown) was used to inoculate 5 mL LB starter cultures, which were grown aerobically at 37 ^oC with shaking; after approximately 6 hours, this culture was used to inoculate fresh LB medium (section 2.2.2) supplemented with 0.5% (w/v) glycerol and 0.4% (w/v) sodium fumarate and grown anaerobically at 37 ^oC. After 16 hours, the cells were harvested by centrifugation at 4785xg for 12 minutes and 4 ^oC, and the cell pellets were resuspended in Buffer I. All further steps, including centrifugation, were conducted at 4 ^oC or on ice. The cells were disrupted by French pressing three times at 20 kpsi and then centrifuged at 3000xg for 30 minutes. To isolate the membrane fraction, the supernatant was further centrifuged at 149008xg for 60 minutes. The supernatant produced from this centrifugation was discarded and the membrane pellet manually homogenised in Buffer II. A stock solution of the detergent Trition X100 (30% in Buffer II) was added such that the final concentration was 3%. The mixture was stirred for 40 minutes prior to centrifugation at 149008xg for 60 minutes, after which the cell pellets were discarded. Imidazole (Alfa Aesar) and dithiothreitol (DTT, Melford) were added to the supernatant to final concentrations of 40 mM and 1 mM, respectively. This was then loaded onto a Ni-affinity column (5 mL HisTrap Chelating HP column, GE Healthcare), which had been pre-equilibrated in a minimum of 10 column volumes of Buffer A. Once fully loaded, the column was washed with a further 200 mL Buffer A until the absorbance at 280 nm and 420 nm had stabilised. Hyd-1 was eluted using a linear imidazole gradient (Buffer B) over 16 column volumes, whilst continuing to monitor the absorbance at 280 nm and 420 nm. An example chromatogram is shown in Figure 2.4.

This was used alongside SDS-PAGE (page 47) to determine which fractions contained pure Hyd-1. These fractions were pooled and concentrated in a centrifugal concentrator (Vivaspin, 50,000 Da mwco, GE Healthcare) to a volume of approximately 1 mL. The concentrated protein was buffer exchanged into Buffer C (for electrochemistry) or EPR Buffer (for EPR spectroscopy) using a PD-10 desalting column (GE Healthcare). The urified Hyd-1 was snap frozen and stored in liquid nitrogen. The concentration of Hyd-1 was determined by the Bradford method (page 47).

Table 2.14: Buffers for Hyd-1 Purification. All components were supplied by Melford, Alfa Aesar or Thermo Fisher Scientific.

Buffer Name	Composition
Buffer I	100 mM Tris-HCl, 1 mM EDTA, 50 mM NaCl, (1 mM DTT,) lysozyme, DNase, titrated to pH 7.5 using HCl
Buffer II	100 mM Tris-HCl, 350 mM NaCl, 1 mM DTT, titrated to pH 7.5 using HCl
Buffer A	20 mM Tris-HCl, 350 mM NaCl, 60 mM Imidazole, 1 mM DTT, 0.02% Triton X100, titrated to pH 7.2 using HCl
Buffer B	20 mM Tris-HCl, 350 mM NaCl, 750 mM Imidazole, 1 mM DTT, 0.02% Triton X100, titrated to pH 7.2 using HCl
Buffer C	20 mM Tris-HCl, 350 mM NaCl, 1 mM DTT, 0.02% Triton X100, 10% (v/v) glycerol, titrated to pH 7.2 using HCl
EPR Buffer	100 mM MES, 100 mM NaCl, 1 mM DTT, 10% (v/v) glycerol, titrated to pH 6 using NaOH and HCl

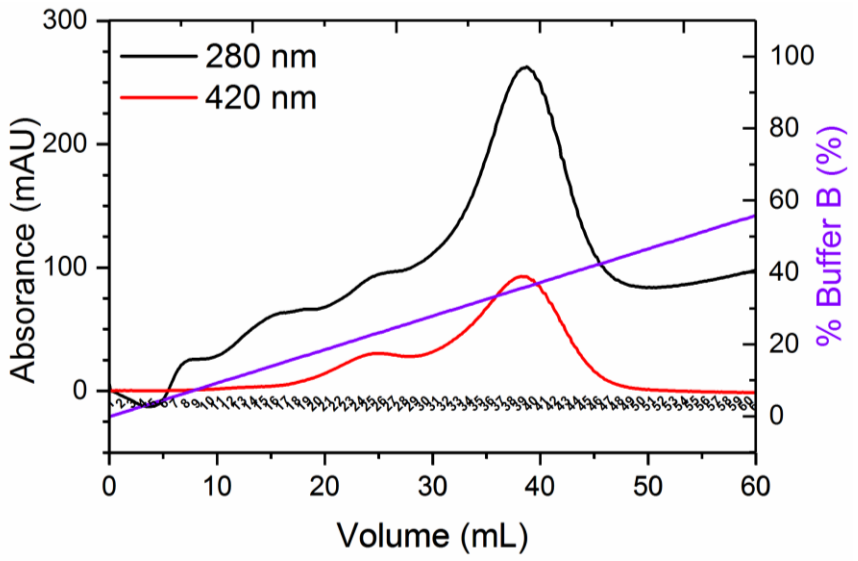


Figure 2.4: Chromatogram from Ni-affinity chromatography of the Hyd-1 variant D118N/D574N. D118N/D574N was eluted using a linear gradient of imidazole over 16 column volumes whilst the absorbance at 280 nm and 420 nm was monitored. Prep size: 42 L

SDS-PAGE for Protein Separation

Sodium Dodecyl Sulfate (SDS) Polyacrylamide Gel (PAGE) is a technique that allows separation of proteins by size. Protein (10 μL) was combined with 10 μL of loading buffer (Table 2.15) containing freshly added DTT and denatured at 98 °C for 1 minute. This mixture (10 μL) was loaded onto a pre-made SDS gel (Invitrogen) and electrophoresed for 50 minutes in 1x MOPS Buffer (Table 2.15) at 200 mV; a pre-stained protein ladder (NEB) was included to allow determination of the protein bands based on molecular weight. The gel was stained using Instant Blue (Expedeon) for 15 minutes to reveal protein bands. An example for native Hyd-1 is shown in Figure 2.5.

Table 2.15: Buffers for SDS-PAGE. Buffer components supplied by Melford, Alfa Aesar or Thermo Fisher Scientific.

Buffer Name	Composition
Gel Loading Dye	106 mM Tris-HCl, 141 Tris base, 2% SDS, 10% Glycerol, 0.51 mM EDTA, 0.22 Serva Blue G250, 0.175 mM Phenol Red, pH 8, excess DTT
20x MOPS Buffer	50 mM MOPS, 50 mM Tris, 0.1% SDS, 1 mM EDTA, titrated to pH 7.7 using HCl

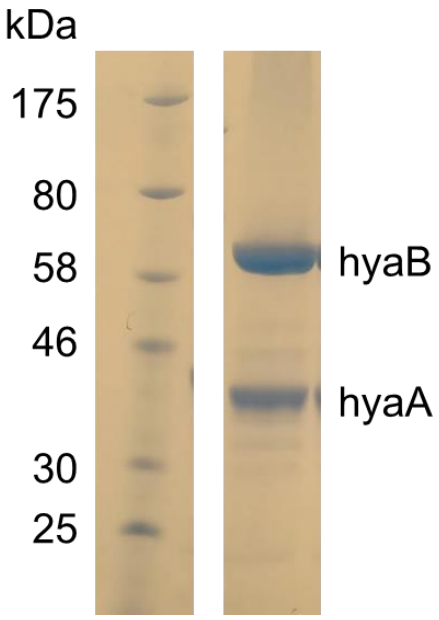


Figure 2.5: Denaturing electrophoresis (SDS-PAGE) of native Hyd-1. Protein was loaded following Ni-affinity chromatography. Protein bands corresponding to hyaA and hyaB are indicated.

Bradford Method for Determining Protein Concentration

Concentration of Hyd-1 and variants was determined using the Bradford method.[111] Bradford reagent (0.8 mL, Sigma Aldrich) was added to 0.5 mL of sample and incubated for 15 minutes at room temperature. The absorbance at 595 nm was measured and the concentration determined from a standard curve produced using Bovine Serum Albumin (Sigma Aldrich). Several Hyd-1 samples, with different dilution factors, were prepared to ensure an average concentration (and therefore a standard deviation) could be calculated.

2.4 Crystallography of Hyd-1 Variants

All crystallisation was performed in collaboration with Professor Simon E. V. Philips and Dr Stephen B. Carr at RCaH.

2.4.1 Aerobic Isolation for X-Ray Crystallography

For X-Ray Crystallography, further purification steps were required. Additional buffers are described in Table 2.16. SDS-PAGE was performed after each column to determine purity. A linear gradient of imidazole was applied over 20 column volumes to allow better separation of Hyd-1 and impurities. The fractions were pooled, concentrated to a maximum volume of 0.75 mL and dialysed into dialysis buffer overnight. Subsequent steps were performed at the Research Complex at Harwell (RCaH) under the supervision of Dr Stephen Carr. The sample was further purified using a Size Exclusion Column (Gel Filtration Superdex200 increase 10/300 GL column, GE Healthcare) equilibrated in Dialysis Buffer. Protein that did not contain the cytochrome *b* was applied to a hydroxyapatite column (Bio Gel HTP hydroxyapatite, Biorad) in Buffer HTI, and eluted using a linear phosphate gradient with Buffer HTII over 10 column volumes. Fractions containing the dimer of heterodimers $(HyaAB)_2$ were pooled, concentrated to approximately 1 mL and dialysed overnight in dialysis buffer. The concentration of the protein was determined using the Bradford method (page 48) and the sample concentrated or diluted using dialysis buffer until its concentration was within the range 4.5 to 5 mg mL^{-1}.

Table 2.16: Additional buffers required for Hyd-1 purification for X-Ray Crystallography. Components were supplied by Melford, Fisher Chemicals or Sigma Aldrich.

Buffer Name	Composition
Dialysis Buffer	20 mM Tris-HCl, 150 mM NaCl, 1 mM DTT, 0.02% n-dodecyl β-D-maltoside (DDM)
HTI	10 mM potassium phosphate dibasic (K2HPO4)/potassuium phosphate monobasic (KH2PO4), 150 mM NaCl, 1 mM DTT, 0.02% DDM, pH 7.2
HTII	500 mM K2HPO4/ KH2PO4, 150 mM NaCl, 1 mM DTT, 0.02% DDM pH 7.2

Crystallisation

Hyd-1 variants D574N and D118N/D574N were crystallised for X-Ray diffraction using the sitting-drop vapour diffusion method as described in ref 48. Protein solution (1.5 μL) was mixed with 1.5 μL crystallisation buffer (Table 2.17) and incubated at 25 ^{o}C. A series of pH and PEG 3350 (Hampton Research) conditions were used to promote crystallisation: the pH was varied in the range 5.7 – 6.0 and the PEG from 20 – 23% (w/v). For both variants, rod shaped crystals were produced. Crystals were transferred to a solution of mother liquor (Table 2.17) and flash frozen in liquid nitrogen.[48]

Table 2.17: Buffers used in Crystallisation of Hyd-1 variants. All components were supplied by Sigma-Aldrich except for PEG 3350 which was supplied by Hampton research.

Buffer Name	Composition
Crystallisation buffer	100 mM Bis-Tris, 200 mM $LiSO_4$, 150 mM NaCl, pH 5.7 – 6.0, 20 – 23% (w/v) PEG 3350
Mother liquor	As crystallisation buffer but with an additional 2% PEG, 5 mM $K_3[Fe(CN)_6]$, 20% (v/v) glycerol

Data Collection

Data were collected at Diamond light source beamlines I02 and I04-1. Data collection and refinement was performed by Dr Stephen Carr according to reference 48. All structures were deposited in the protein data bank (PDB). Accession codes are: 5A4I – D574N, 5ADU – D118N/D574N. Structures of E28D and E28Q will be released to the PDB in August..

2.5 Mediator-based Solution Assays for H_2 Oxidation by Hydrogenase

The steady-state hydrogen oxidation activity of variants was measured using a conventional solution assay. The reduction of methylene blue (Aldrich) at 600 nm was monitored using an Ocean Optics S2000 fibre optic spectrometer controlled by OOIBase32 software (Ocean Optics). All measurements were conducted at 25 ^{o}C in an anaerobic glove box (< 3 ppm O_2, Belle Technologies), and enzymes were activated for 16 – 32 hours under a flow of H_2 prior to use. Methylene blue was made to a stock concentration of 50 μM in pH 6.0 potassium phosphate buffer (50 mM K_2HPO_4 and KH_2PO_4, Fisher Scientific) and diluted to a working concentration of 25 μM. The working solution (5 – 10 mL) was continuously purged with H_2 in a sealed glass vial for a minimum of 10 minutes prior to the experiment. H_2-saturated methylene blue (1 mL) was then transferred to a sealed cuvette and the change in absorbance monitored to ensure it was stable. Whilst continuing to monitor the absorbance, 5 μL of activated enzyme was injected into the sealed cuvette using a gas-tight Hamilton syringe. The solution was stirred continuously throughout to ensure a homogenous distribution of enzyme within the cuvette. The turnover frequencies were taken from the initial velocities, where the change in absorbance was linear, and are expressed as μmol H_2 oxidised per minute per mg enzyme (μmol H_2 min^{-1} mg^{-1}) and apparent turnover rate *k* (s^{-1}). The extinction coefficient for methylene blue was 22400 cm^{-1} M^{-1}.[112] Enzyme solutions were 0.1 – 5 mg mL^{-1}, as determined by Bradford assay (page 48).

2.6 Electrochemical Theory

2.6.1 Overview of Protein Film Electrochemistry

Protein film electrochemistry (PFE) is routinely used in the study of redox proteins.[113] In PFE, the protein is directly adsorbed onto a conductive surface in a (sub)monolayer and the applied potential *E* is controlled externally. The enzyme activity is then measured as a current (i) which is directly proportional to the turnover frequency. Precise potential control means PFE is an excellent technique for studying the thermodynamics and kinetics of an electron transfer event.[16]

PFE has several advantages over conventional solution assays.[113] A miniscule amount of protein is required, often only 0.5 μL, depending on the sample concentration. Direct adsorption of a protein on a conductive surface eliminates diffusion and the need for mediators. Immobilisation on a solid surface also provides a convenient method for changing the environment surrounding the protein, for example, the pH can be changed or non-volatile inhibitors removed by a buffer exchange. PFE, however, requires that the protein retains its native structure on adsorption and is orientated such that interfacial electron transfer (IET) between the electrode and enzyme is fast,[113] i.e. the electron entry/exit site is located within 14 Å[59] of the electrode surface.

In all experiments, pyrolytic graphite edge (PGE) electrodes were used (in some cases these were modified). PGE has a rough surface, likened to an 'egg box', that increases the surface area of the electrode.[113] Additionally, when abraded the carbon becomes functionalised with hydrophilic C–O groups that interact with surface groups on the enzyme.[16]

2.6.2 Three Electrode System

All electrochemical experiments require minimally a *working* electrode (WE) and a *reference* electrode (RE). The WE is used to measure the reaction of interest and its potential is monitored relative to that of the RE. A RE electrode should be an ideal, non-polarisable

electrode and thus has a fixed, known potential (at constant temperature).[114] This is only true for *small* currents; the large currents produced in many experiments, including PFE, necessitate the inclusion of a third electrode known as the *counter* electrode (CE). In the three-electrode arrangement, the current is passed between the WE and CE and the potential of the WE is measured against the RE (Figure 2.6).

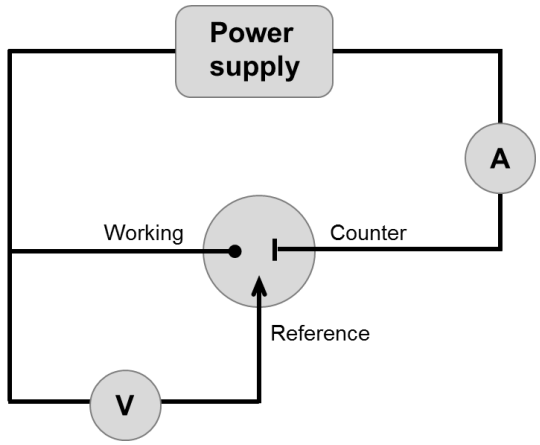


Figure 2.6: Three electode set up for Protein Film Electrochemistry. The potential of the working electrode is fixed relative to the reference electrode by a potentiostat. Current flows between the working and counter electrodes. V = voltmeter. A = ammeter.

2.6.3 Cyclic Voltammetry

In cyclic voltammetry,[114-115] the current is monitored as the potential is cycled linearly between two limits (*E*1 and *E*2) and the current at each potential is measured to produce a plot of *i* vs *E*, known as a cyclic voltammogram (CV) (Figure 2.7). The rate at which the potential is scanned is known as the *scan* (*sweep*) *rate* and is measured in V s^{-1} or mV s^{-1}. The scan from a potential *E*1 to a potential *E*2, where *E*1 < E2, is the oxidative or anodic scan and results in positive currents. The reverse scan is referred to as the reductive or cathodic scan and results in negative current. This is the European convention; some sources will use an axis that runs from high to low *E* and use positive current to denote reduction.

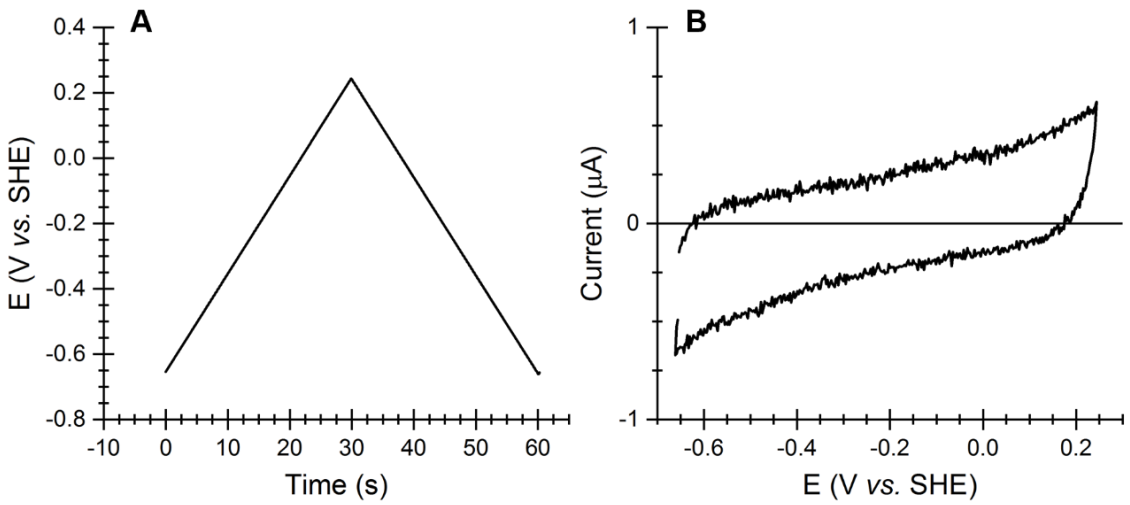


Figure 2.7: Cyclic voltammetry. A – Change in potential with time during cyclic voltammetry. **B** – A cyclic voltammogram (CV) of 'blank' pyrolytic graphite edge electrode. Cyclic voltammogram in the potential range –0.65 V to +0.24 V at a scan rate of 30 mV s^{-1}. Other conditions: pH 6, 30 °C, 100% H_2, total gas flow = 1000 scc min^{-1}, ω = 1000 rpm

Non-Faradaic Processes

In a CV, the observed current has two contributions: non-Faradaic and Faradaic processes at the electrode surface.[113-114] Non-Faradaic processes do not involve electron transfer but instead involve changes at the electrode-solution interface. This may include adsorption or desorption of solution species and changes to the electrode-solution structure.

The electrical double layer is a model that describes how the electrode-solution interface acts as a capacitor.[114-115] When a potential is applied to an electrode, an excess or deficiency of electrons accumulates at the electrode surface. The resulting charge (q^{M}) is balanced by a charge in solution (q^{S}) so that

$$q^{\mathrm{M}} = -q^{\mathrm{S}} \qquad (2.1)$$

In the solution, the charge is not due to an accumulation or deficiency of electrons but instead due to the presence of charged species and consists of several layers (Figure 2.8). Most of the charge is contained close to the electrode surface in the *inner Helmholtz plane* (IHP) and the *outer Helmholtz plane* (OHP) but the total balancing charge extends into the

solution in the *diffuse layer*. The IHP is composed of species that are specifically adsorbed to the electrode surface and the OHP contains solvated ions which are non-specifically adsorbed to the electrode surface. These species interact with the charged electrode surface through electrostatic interaction and, because of thermal motions in the solution, they are distributed across the diffuse layer and into the bulk solution.[114-115]

Non-Faradaic contributions can be seen in 'blank' experiments, i.e. an electrode with no adsorbed enzyme and/or in a solution containing no redox-active species (Figure 2.7B).[113] As the potential is raised, the double layer is altered as the electrode charge, and consequently the solution charge, changes. This is observed as current, known as *capacitive* or *charging* current which reaches a steady-state value (C_d).[114] On the reverse scan, as the potential is lowered, the capacitive current reaches a value that is equal in magnitude but which is negative ($-C_d$) so that the overall charge of the electrode- solution interface is neutral.[114] The size of the capacitive current is dependent on several factors including electrode size, scan rate, the applied potential and the composition of the solution.[113]

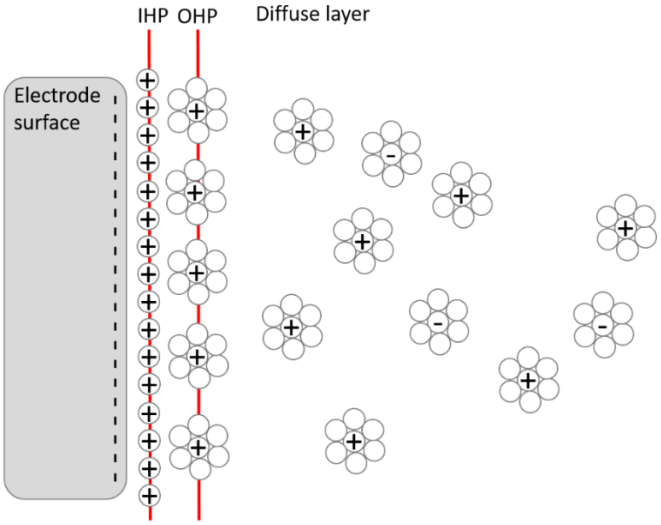


Figure 2.8: The electrical double layer at an electrode-solution interface. The accumulation of charge at the electrode surface results in the ordering of charged species in the solution. The 'Inner Helmholtz Plane' (IHP) is close to the electrode surface and is due to the ordering of ions at the electrode surface. The 'Outer Helmholtz Plane' contains solvated ions which extend into the diffuse layer due to thermal motions in solution. For more information, see refs 113-114.

Faradaic Processes

Faradaic processes are those that involve reduction or oxidation reactions.[113] Electrons flow between the electrode and a redox active species either in solution or adsorbed on the electrode surface.

Non-turnover signals involve the reduction or oxidation of redox sites within the protein but do not involve turnover of substrate. In a system that is not limited by mass-transport of redox species to or from the electrode (i.e. use of a rotating-disk electrode, Section 2.6.5), all redox centres in solution or adsorbed to the electrode surface will be reduced when the electrode is poised at a potential below the reduction potential of the redox centres. As the potential is raised, positive current is measured as the redox centres are oxidised until eventually all are oxidised and the current drops to zero. On the reverse scan, the opposite occurs as the redox sites become reduced. The resulting two peaks are centred about the reduction potential of the redox site.[114-115] For hydrogenases, non-turnover peaks are not observed. The large size of hydrogenases limits the electroactive coverage so that non-turnover signals are too small to be observed and are therefore masked by the capacitive current.[116] Additionally, PFE experiments with hydrogenase are conducted in the presence of substrate (H^+) so catalytic waves are observed instead. However, recent work by Adamson *et al* with Fourier Transformed alternating current Voltammetry has been used to determine the reduction potentials of the Fe-S clusters in Hyd-1.[62]

Catalytic currents occur as the active site converts the substrate to product through reduction or oxidation and the active sites are continually being oxidised and reduced by electron exchange with the electrode. As the driving force (potential) is increased, the enzyme continues to catalyse the oxidation or reduction of the substrate at increasingly high rates and a wave shape is seen. An example of electrocatalytic H_2 oxidation by Hyd-1 is seen in Figure 2.9.[62, 113]

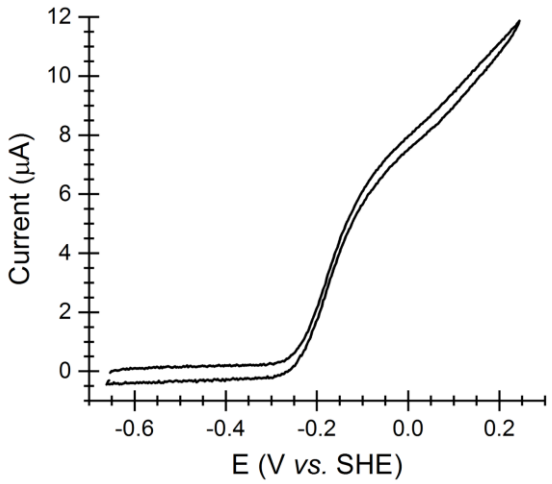


Figure 2.9: Cyclic voltammogram of native Hyd-1 on a pyrolytic graphite edge electrode. The potential was scanned from −0.65 V to +0.24 V at a scan rate of 30 mV s^{-1}. Hyd-1 has an overpotential requirement before H_2 oxidation is seen. This was discussed in Section 1.7. Other conditions: pH 6, 30 °C, 100% H_2, total gas flow = 1000 scc min^{-1}, ω = 1000 rpm

2.6.4 Chronoamperometry

In chronoamperometry,[113] the potential is held at a constant value whilst the current is measured over time to produce a plot of *i* vs *t*. The potential can also be stepped so that the current at different potentials can be measured. Chronoamperometry is often used to monitor the response of an enzyme to inhibitors over time. Cyclic voltammetry may not be appropriate in this case when the response of a particular state wants to be observed, or a particular state needs to be avoided, and in these cases chronoamperometry is used instead. An example of this would be the O_2 inhibition experiments in Chapters 3 and 4: the potential is poised below the potentials where anaerobic inactivation of the enzyme occurs; this ensures the current is not convoluted by simultaneous aerobic and anaerobic inactivation, and that it represents only the aerobic inactivation due to the presence of oxygen.

2.6.5 Mass Transport

Although rapid IET is crucial, it is not the only process that governs the rate of electron transfer in PFE. If an enzyme's inherent activity is to be observed by PFE, mass transport of

substrate to (and product from) the electrode surface should not be rate-limiting.[113] When flow of substrate to the electrode is controlled by diffusion, the electrocatalytic current will reach a maximum as the substrate at the electrode surface is depleted by the enzyme faster than it is replenished. In this situation, the rate is 'diffusion limited'. However, movement of solution species can be established by, for example, the use of Rotating Disk Electrodes (RDEs). Rotation results in solution being spun away whilst drawing fresh solution towards the electrode surface so that substrate is continually supplied to the adsorbed enzyme.[113-115]

The Koutecký–Levich equation (2.2)[114] can be used to determine the rotation rate required to ensure the transport limited (i_{lim}) current is not observed:

$$\frac{1}{i_{obs}} = \frac{1}{i_{lim}} + \frac{1}{0.62nFC_{\mathrm{O}}(D_{\mathrm{O}})^{2/3}v^{-1/6}\omega^{1/2}} \qquad (2.2)$$

where i_{obs} is the observed current, n is the number of electrons in the redox reaction, F is the Faraday constant (96 475 C mol^{-1}), C_{O} is the concentration of the species being oxidised/reduced, v is the scan rate and ω is the rotation rate. The current is measured at different rotation rates (ω) and $^{1}/_{i_{lim}}$ is plotted against $^{1}/_{\omega^{1/2}}$. In cases where different substrate concentrations ([S]) are to be used, a Koutecký–Levich plot should be generated under the lowest [S] to be used. The *y*-axis intercept provides the rotation rate at which mass-transport will no longer be limiting.

2.7 Electrochemical methods

2.7.1 Experimental set up

All PFE experiments were performed in an anaerobic glovebox (MBraun, Glove Box Technology or Belle Technology) under an N_2 atmosphere (< 3 ppm O_2). An Autolab potentiostat (PGSTAT128N) controlled using Nova software (Metrohm Autolab) was used to make electrochemical measurements. A pyrolytic graphite edge (PGE) rotating disk

electrode (RDE) constructed in-house[113] was used as the working electrode and rotated at constant speed (ω = 1000 – 3500 rpm) using an electrode rotator (Metrohm Autolab or EG&G). This was placed into a gastight, thermostatted glass electrochemical cell. The three-electrode set-up was completed with a Pt wire counter electrode and a Saturated Calomel Electrode (SCE) housed in a sidearm filled with 0.1 M NaCl connected to the main cell body by a Luggin capillary. All potentials are quoted as versus the Standard Hydrogen Electrode (SHE) and converted according to the equation $E_{SCE} = E_{SHE} + 0.241\,V$ at 25 °C.[114] A schematic is shown in Figure 2.10.

All electrochemical measurements were performed in a mixed buffer system (15 mM each of MES, CHES, TAPS, HEPES, NaOAc and 100 mM NaCl) prepared using ultrapure water (Millipore, 18 MΩ cm). This was adjusted to the desired pH at the experiment temperature. Precise gas mixtures (BOC gases) were produced using mass flow controllers (Sierra Instruments).

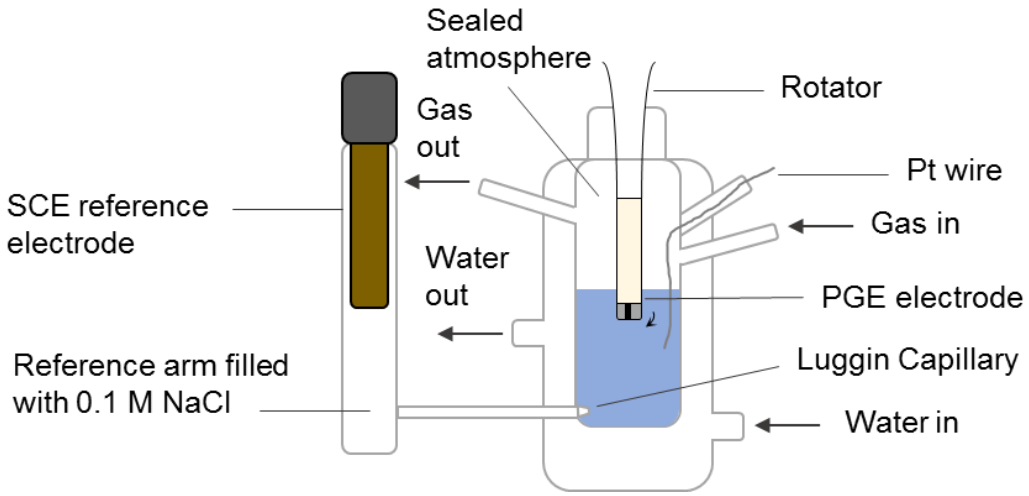


Figure 2.10: Electrochemical set up for Protein Film Voltammetry. Three-electrode set up is completed by a PGE working electrode, a platinum counter electrode and a SCE reference electrode. The reference electrode is separated from the main cell body by a reference arm, which is filed with 0.1 M NaCl. The glass cell provides a sealed, anaerobic atmosphere. The cell temperature is controlled by water bath and the headspace atmosphere can be changed using gas cylinders connected to the cell via mass flow controllers to allow precise mixing.

2.7.2 Growing an enzyme film

The PGE electrode was abraded with P400 Tufbak Durite sandpaper and rinsed under a stream of ultrapure water. The electrode was dried with tissue and a 'blank' CV recorded. The electrode was once again sanded, rinsed and dried before enzyme (0.5 – 1 μL) was pipetted directly onto the PGE disk. After 30 s, excess enzyme was removed with a flow of ultrapure water and gently dried with tissue.

2.7.3 Modification of PGE Electrodes

For the R509K and E28Q variants, weak currents were observed when a standard PGE electrode was used. A modified electrode allowing the covalent attachment of the enzyme to the electrode was used to amplify the currents. This was exemplified by Krishnan and Armstrong using a fuel cell in which Hyd-1 and bilirubin oxidase were covalently attached to the anode and cathode, respectively.[30]

Multi-walled nanotubes (MWNT, >90% carbon), 1-pyrenebutryric acid (Py) 1-ethyl-3-(3-dimethylaminopropyl)carbodiimide (EDC) and N-hydroxy sulfosuccinimide (NHSS) were all supplied by Sigma Aldrich. A suspension of MWNT was prepared in dimethylfomamide (DMF), as follows: 1 mg mL^{-1} MWNT were suspended in DMF and sonicated overnight; the suspension was further sonicated for at least 15 minutes immediately before use. Prior to modification, a 'blank' CV was recorded, as described in Section 2.7.2. The electrode was sanded, rinsed and dried once again, before being covered with the MWNT suspension and left to dry overnight. The PGE-MWNT electrode was rinsed with ultrapure water and a second 'blank' experiment was recorded. A solution of Py (10 mM in DMF) was used to coat the electrode and left for 1 hour, ensuring the electrode surface did not dry completely. The electrode was once again rinsed and then activated for 45 – 60 minutes with a fresh solution of EDC (0.4 M) and NHSS (0.1 M) in ultrapure water. The electrode was rinsed, gently dried

and then covered with enzyme (~ 10 μL) for 45 minutes. Excess enzyme was removed by rinsing under a stream of ultrapure water.

2.7.4 Enzyme film activation

Enzyme films were activated using the following protocol:

i. The electrode potential was poised at −0.65 V for 600 s

ii. Film growth was monitored by measuring the current at approximately 0 V.

iii. Steps i and ii were repeated three times before recording a cyclic voltammogram in the potential range −0.65 V to +0.24 V at a scan rate of 30 mV s^{-1}.

iv. Steps i-iii were repeated until film loss was seen in the cyclic voltammograms, indicating that the film was fully activated, or that further film activation was hidden by film loss

2.8 Electron Paramagnetic Resonance Spectroscopy

2.8.1 Theory of EPR Spectroscopy

Electron Paramagnetic Resonance (EPR) spectroscopy[117] (or Electron Spin Resonance, ESR) is often employed in the study of metalloproteins, including hydrogenases.[16] EPR spectroscopy can, however, only be used to study samples that have a single or multiple unpaired electrons, i.e. the sample is paramagnetic. Thus, for [NiFe]-hydrogenases, not all of the catalytic states discussed in Section 1.9 appear in an EPR spectrum.

Electrons have spin ($s = {}^{1}/_{2}$) and when exposed to an external magnetic field the degenerate spin states ($m_s = \pm {}^{1}/_{2}$) split (the Zeeman effect, Figure 2.11). The energy separation between the two varies with the magnetic field (2.3):

$$\Delta E = g_e \mu_B B_0 \qquad (2.3)$$

where g_e is the electron *g*-factor (2.0023), μ_B is the Bohr magneton and B_0 is the strength of the external magnetic field. Absorption or emission of a photon (*hv*), typically in the microwave region, can induce an electron to transition between the two. In an EPR experiment, the microwave frequency is fixed and the field is varied until the energy gap matches the applied frequency. EPR data is presented as the first derivative of the absorbance spectrum.[117]

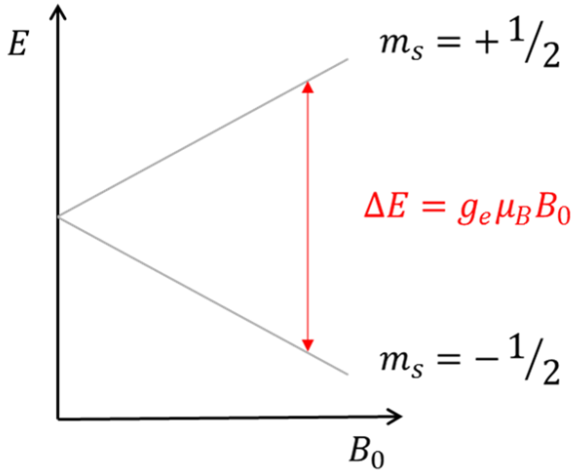


Figure 2.11: Zeeman splitting of electron spin states in a magnetic field. When placed in an external magnetic field, the previously degenerate states are split. This splitting varies with the strength of the external field (B_0).

2.8.2 EPR Spectroscopy Methods

Experiments were performed in a EMX X-band Continuous Wave EPR Spectrometer (Bruker) at the CÆSR facility (Oxford). This was equipped with an X-band Super High Sensitivity resonator (Bruker) and cooled with a helium flow cryostat (Oxford Instruments). Samples were prepared in an anaerobic glovebox (Belle Technologies, < 3 ppm O_2) in a thermostatted glass cell (made in-house). Mass flow controllers were used to obtain consistent glass flow. Samples were removed from the cell using a gas-tight Hamilton syringe. Low precision (4 mm) EPR tubes were used. Data analysis was performed using the programmes developed by Professor Wilfred R. Hagen, described in ref 117.

3 The Role of D118 and D574 in *Ec*Hyd-1

3.1 Introduction to Proton Transfer in [NiFe]-hydrogenases

Hydrogen cycling ($H_2 \rightleftharpoons 2H^+ + 2e^-$) by hydrogenases requires movement of both electrons and protons between the active site and the protein surface, where they are transferred to redox partners. Detailed studies of the electron transfer chain – the Fe-S clusters[14-15, 28, 67-68] – have been performed but relatively little is known about the proton transfer (PT) pathway(s).[5] It should be recognised that multiple PT pathways may exist in the [NiFe]-hydrogenases: different routes may be important if other pathways are unavailable or their use may be dependent on the reaction direction (H_2 oxidation/evolution).

3.2 Mechanism of Proton Transfer

PT in proteins occurs by two mechanisms: the 'Grotthuss' mechanism[118-120] and the proton tunnelling.[119, 121-122] Although Grotthuss' original publication did not specifically describe proton transfer, it is often used to explain proton movement in both bulk solution and proteins via proton 'hopping' (Figure 3.1). In solution, hydrogen bonding results in the formation of chains of water molecules. This chain will have an electrochemical gradient which favours the movement of H^+ (left to right in Figure 3.1). As a proton approaches the first water molecule in the chain, a covalent H–O bond forms. As a result, one of the other water protons is shared with the next water molecule in the chain. The proton 'hopping' step propagates in this manner along the chain until the proton leaves the last water molecule in the chain. The proton that leaves the chain, however, is not the same proton that entered the water chain. There is also a reversal of the dipole moment of the chain such that all the waters in the chain need to reorient for further proton transfers.[118]

These water 'wires' can be seen independent from bulk solution in the tunnels and cavities of many proteins. Here, they are often punctuated by charged or polar residues which are capable of hydrogen bonding, including but not limited to glutamate, aspartate, histidine and

lysine. These residues provide a hydrophilic environment for water molecules inside the hydrophobic protein and are often directly involved in proton transport.

PT by quantum mechanical tunnelling has also been explored in the literature and is relevant to situations where there is a large barrier to proton transfer, for example if a PT pathway includes residues resistant to ionisation.[121-122] The nature of the putative PT pathway (water molecules, charged residues) explored here, however, indicates the Grotthuss mechanism is more relevant to this thesis.

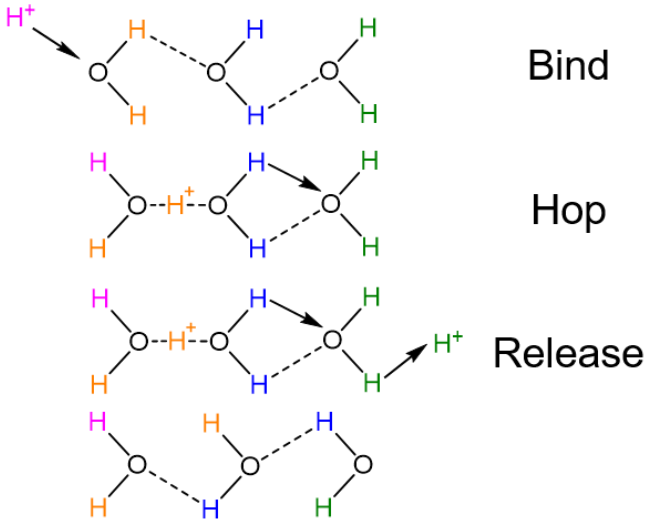


Figure 3.1: The Grotthuss Mechanism of proton transport through a chain of water molecules. As a proton (magenta) approaches a chain of water molecules connected by hydrogen bonds, an H–O covalent bond is formed and one of the 'original' water protons (orange) is shared by the next water molecule in the chain. The proton propagates along the chain until it leaves the last water molecule in the chain. The proton that leaves (green) is not the same proton that enters the chain. Once the proton has been transferred, the dipole moment of the chain is reversed and the water must reorient for subsequent proton transfers. For more information, see refs 117-119.

3.3 Proposed Proton Transfer Pathways

Although a specific PT mechanism does not yet exist for [NiFe]-hydrogenases, there are several models based on both experimental and computational studies. Some of these are shown in Figure 3.2. Although there are similarities between the models (see below), there is no consensus in the literature about the identity of the PT networks. Defining extended PT

networks may be difficult in enzymes in which there are multiple PT route: once a proton moves past the first transfer site(s), multiple networks may be available and changing any one residue could result in one network being used in favour of another.

When the first crystal structure of a [NiFe]-hydrogenase was published in 1995,[37] the authors proposed a PT network comprised of several histidine residues and a glutamate but a higher resolution structure showed that one of the histidines is in fact leucine.[35] Aspects of this pathway were used by Teixeira *et al*, who analysed several putative networks to design a single PT network (Figure 3.2A).[52] In Hyd-1, glutamate-46 (small subunit, $E46_S$) is replaced by an aspartate and, although this is a conservative substitution, the shorter carboxylate

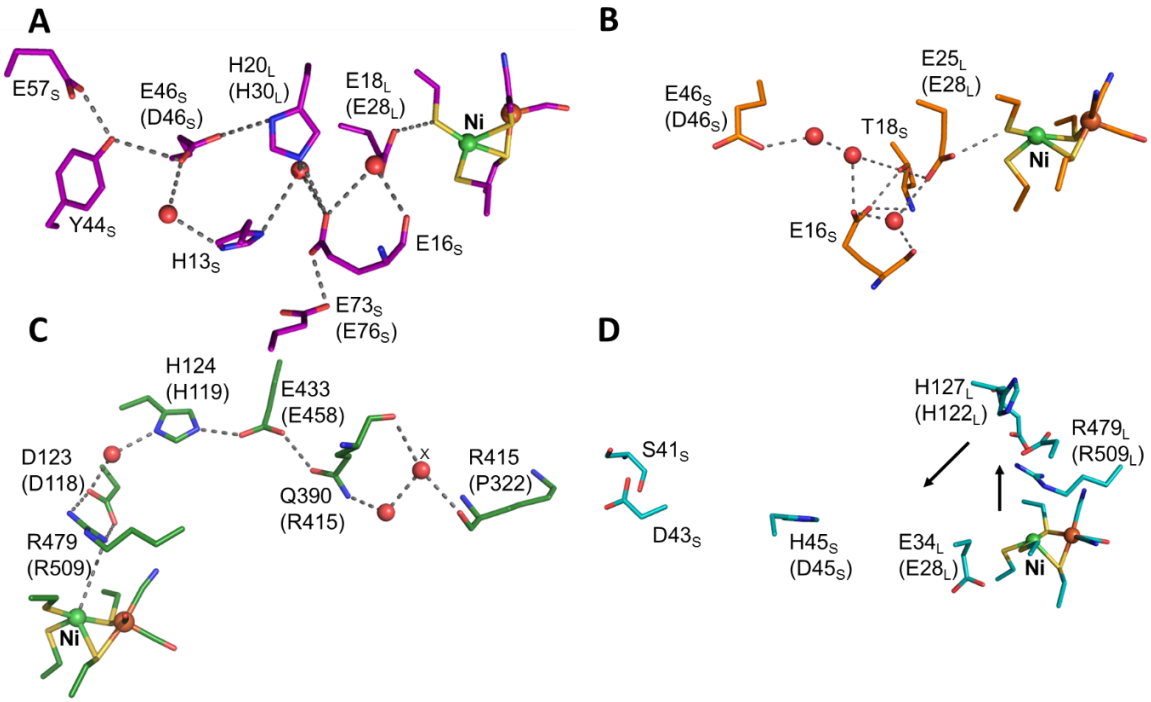


Figure 3.2: Proton transfer pathways proposed for [NiFe]-hydrogenases. Residue numbers are given for the [NiFe]-hydrogenase used in the study. Any differences in numbering or residue identity in *Ec*Hyd-1 is given in parentheses. L or S designates large or small subunits. Where L or S isn't specified, residue number refers to large subunit. Metal ions and water molecules are shown as spheres. Waters not present in Hyd-1 are marked with X. **A** – Pathway by Teixeira *et al* in *Desulfovibrio gigas* (PDB: 2FRV) in ref 52 **B** – Pathway by Fdez. Galván in *Desulfovibrio fructosovorans* (PDB: 1YQW) in ref 53. **C** – Pathway by Szőri-Dorogházi *et al* in *Desulfovibrio vulgaris* Miyazaki F (PDB: 1WUL) in ref 51. **D** – Pathway by Sumner and Voth in *Desulfovibrio vulgaris* Miyazaki F (PDB: 4U9F) in ref 122. Arrows indicate direction of proton transfer expected in this pathway.

chain of Asp is rotated away from the active site in the crystal structure. Disruption of the hydrogen bond network in this manner could retard the PT rate but without experimental results it is impossible to say if there is a significant effect on PT. One of the pathways proposed by Fdez. Galván *et al* in the *Desulfovibrio fructosovorans* (*Df*) [NiFe]-hydrogenase also includes the acid at 46 (Figure 3.2B).[53] Other features of Teixeira's route are also retained, specifically the glutamates E18/25 and E16, but Fdez. Galván did not extend the pathway completely to the protein surface. Additionally, the histidine/glutamate network between the active site and $E46_S$ used by Teixeira was replaced with a conserved threonine ($T18_S$) in the small subunit.

The role of T18 was recently explored by Abou-Hamdan *et al* who measured the structural, kinetic and spectroscopic properties of several $T18_S$ variants in the *Df* [Ni-Fe]-hydrogenase:[50] all variants had disrupted hydrogen bond networks and decreased H_2 oxidation/evolution activity to varying extents; one variant, T18G, had negligible H_2 oxidation/evolution activity but high rates of hydrogen-deuterium exchange (catalysing the reaction $D_2/H^+ \rightarrow HD \rightarrow H_2$) which requires PT. These results, supported by data from EPR and FT-IR spectroscopies, indicate that T18 is not directly involved in PT. Instead, the authors concluded that T18 stabilises the local active site structure so that both electron transfer and PT remain fast.[50] This is further supported by the work of Greene *et al*, which demonstrates the role of the conserved E28 in the Ni-C to Ni-S transition (Section 4.1.1).[84]

The second route proposed by Fdez. Galván *et al* includes the C-terminal Mg(II) ion.[53] Although a C-terminal Mg(II) is seen in many [NiFe]-hydrogenase structures, in the structure used by Fdez Galván (PDB: 1YQW) the metal ion in this position is Fe and was changed to Mg(II) for the computational studies. This is not the sole instance in which the Mg(II) ion has been implicated in PT (via its water ligands) as it has been suggested to mediate PT between periplasmic hydrogenases and their *in vivo* redox partner (cytochrome c_3).[76]

Many of the proposed routes assume that the Ni-coordinating terminal cysteine-576 (Hyd-1) accepts the proton from H_2 splitting, forming the metal-hydride. Work in the early 2000s with variants of the *Df* [NiFe]-hydrogenase revealed that a highly conserved glutamate (E28 in Hyd-1, E25 in *Df*), the carboxylate of which is 3.4 Å from the cysteinate-S, is crucial for activity and acts as a 'proton gate'.[49] The two variants E28D and E28Q were active in *para*/*ortho*-H_2 conversion (H–H bond breaking/making, no PT) but showed reduced and negligible H_2 oxidation activity, respectively. These results clearly suggest that E28 is involved in proton movement but not the H_2 activation reaction, i.e. the base is not affected. Recent work, however, has indicated that R509 is the most likely candidate to act as a base, instead[48] and, from here it is unlikely a proton would enter a PT pathway via C576 due to the angle and distance between R509 and C576/E28. This appears to contradict the work by Dementin *et al* with E28. However, if we consider the mechanism of H_2 activation involving R509 by [NiFe]-hydrogenases it becomes apparent that two (minimally) PT networks may be used (viewed as H_2 oxidation): the first transports the 'initial' proton from R509 immediately following H–H bond breaking (pink, Figure 3.3); the proton formed from oxidation of the Ni-hydride follows a different pathway (blue, Figure 3.3) which includes E28.

In the literature, there are two examples of PT networks that begin at R509. Szőrzi-Dorogházi *et al* noted four conserved histidine residues in the sequence alignment of membrane-bound hydrogenases and a series of variants, including R509 and D118 mutants, were created in the [NiFe]-hydrogenase from *Thiocapsa roseopersicina*.[51] The biggest change in H_2 oxidation/evolution activity in the His variants was seen for variants of H119, whilst the D118/R509 variants showed no activity in either reaction. It should be noted that the authors did not recognise the importance of R509 and concluded that it is involved solely in proton transfer rather than having a direct role in H_2 activation. Based on these experimental results, a known structure of the *Dg* [NiFe]-hydrogenase was used to propose an extended PT network beginning at R509 (Figure 3.2C). The change in residues 415 (Q390

→ R415) and 322 (R415 → P322) in Hyd-1 should not disrupt this pathway as the amine head group and backbone carbonyl of lysine and proline, respectively, can still participate in hydrogen bonding. Sumner and Voth also proposed a pathway that includes R509 (Figure 3.2D).[123] However, rather than continuing towards the protein surface in this direction, the pathway continues at a right angle to the active site, and it is unclear how the proton moves from H122 to residue 45 (*Ec* D45, *Dv*MF H45) as there is no obvious hydrogen bond network connecting them.

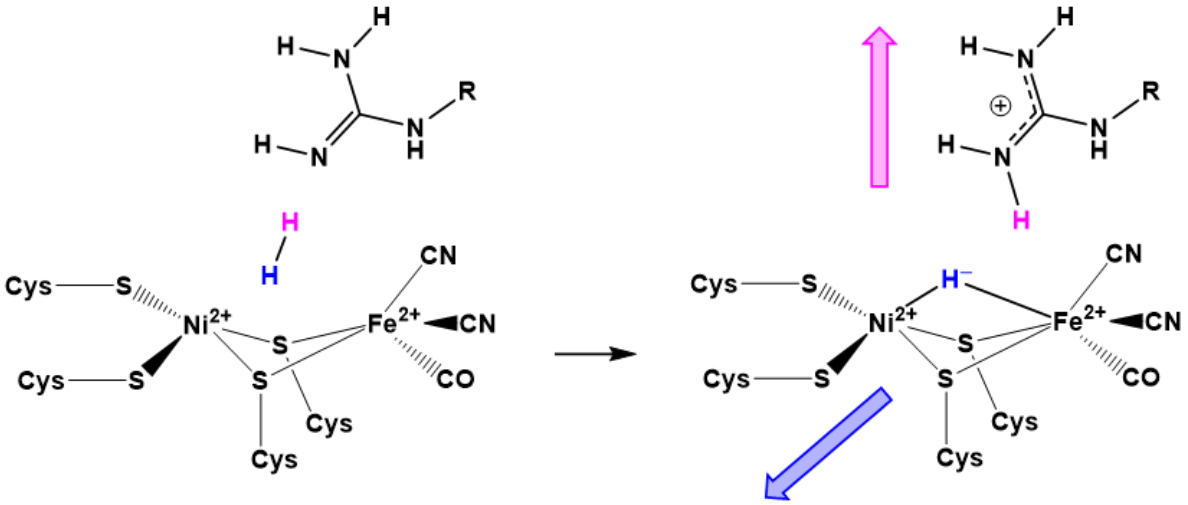


Figure 3.3: Direction of proton transfer networks away from the active site. Hydrogen oxidation forms two protons: hydrogen is split heterolytically to form the first proton on R509 (pink H) and a hydride at the active site (blue H), which is subsequently oxidised to form the second proton. The two protons can leave the active site by two different routes, the general direction of which are shown by the arrows.

3.4 The 'First Proton' Transfer Network

Directly above the active site of Hyd-1, R509 forms a 'canopy' with the conserved aspartates D118 and D574 (Figure 3.4).[48] D574 is strictly conserved across the [NiFe]-hydrogenases, except in Group 4F[6] where it is conservatively substituted for glutamate.[47] There is greater variation in residue 118, although in many cases a polar residue (serine, asparagine, glutamate) is present. Notably, all known [NiFeSe]-hydrogenases have a serine in this position.[47] The high level of conservation for D118 and D574 suggests that they have

a function in the [NiFe]-hydrogenases, yet neither have been the specific focus of any published [NiFe]-hydrogenase research. Their proximity to R509 (Figure 3.4) would allow the carboxylate side chains to form salt bridges or hydrogen bonds with the guanidinium headgroup and suggests two possible roles: 1) they mediate proton transfer to/from the active site and/or 2) they are structural and contribute to 'preorganisation' of the active site prior to catalysis.

Some work on the active site canopy has already begun using the variants D118A and R509K. The latter was discussed in Section 1.10.4 and a large decrease in H_2 oxidation turnover frequency (R509K has approximately 1% the H_2 oxidation activity of native Hyd-1) indicated that R509 is the base in H_2 activation by [NiFe]-hydrogenases. The variant D118A had a H_2 oxidation rate of approximately 26% of native Hyd-1. Although this is a significant drop in rate, it is still high enough to indicate that D118 is not crucial for H_2 oxidation by Hyd-

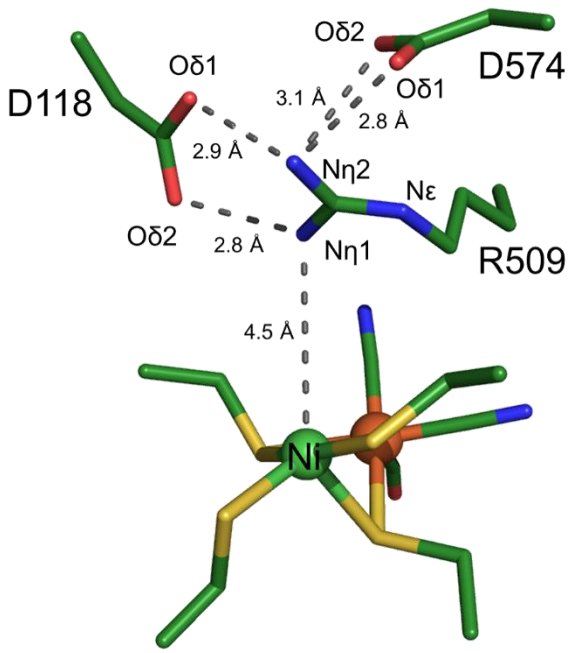


Figure 3.4: The active site 'canopy' of Hyd-1, including the conserved D118 and D574. The active site canopy includes the crucial base R509 and the aspartates D118 and D574, which are highly and strictly conserved, respectively. Both D118 and D574 are close enough to the guanidinium headgroup to form salt bridges and 'pre-organise' the active site for H_2 activation. Alternatively, D118 and D574 may participate in proton transfer. In this structure, Hyd-1 crystallised in the oxidised Ni-B state but the oxygen has been removed for this representation. PDB: 5A4M

1. The D → A substitution, however, resulted in a very high $K_M^{H_2}$ in D118A – 164 μM at 0 V *vs.* SHE compared to 20 μM for native Hyd-1. Despite this, D118A could sustain H_2 oxidation in an atmosphere of 10% H_2 and 10% O_2. In this thesis, work on the active site canopy is continued and data for variants of D118 and D574 is discussed.

3.5 Contributions to this chapter

Several variants are discussed in this chapter. In all cases, data for native Hyd-1 is included and is the combination of multiple repeats by myself (EJB), Dr Rhiannon M. Evans (RME) and Sara A. M. Wehlin (SAMW) at the Department of Chemistry, University of Oxford. Details of who produced each variant is available in Section 2.2.1. The primary focus of this chapter is D574N and the double mutant D118N/D574N but some data for D118E and D118V is also included (see below). EJB performed all electrochemistry and solution assays for D574N and D118N/D574N. Crystal structures for D574N and D118N/D574N were produced as follows: protein purification was performed by EJB and Elena Nomerotskaia (EN); crystal trays were set up by EJB, EN and Dr Steven B. Carr (SBC, Research Complex at Harwell, RCaH), and data collection and structure refinement was performed by SBC and Prof Simon E. V. Philips (RCaH). Structure analysis was performed by EJB with guidance from SBC. Data for variants D118E and D118V were collected by Edward Mallett (EM, University of Oxford) under my supervision and data collection is still underway. At times, data for D118A and R509K is also shown as it provides useful comparisons. The data for D118A and R509K were collected by SAMW and RME. The H_2 production studies (Section3.6.5) which were performed by Gerri M. Roberts under my supervision for all variants.

3.6 Results

3.6.1 Rates and pH optima

The steady-state rate of H_2 oxidation for each variant at pH 6 and 25 °C was measured using conventional solution assay with methylene blue as an electron acceptor. Prior studies have used benzyl viologen[15-16] but the higher reduction potential of methylene blue provides a greater driving force for H_2 oxidation. The initial velocity was used and expressed as the turnover frequency k_{cat} (s^{-1}) or μmol H_2 oxidised min^{-1} mg^{-1} enzyme. The rates of D118V, D118E, D574N and D118N/D574N were 0.9%, 6%, 82% and 20% of native Hyd-1, respectively (Table 3.1). The extremely low rate of H_2 oxidation for D118V (even lower than that of R509K) is surprising given that the data for D118A and D118N/D574N indicate this residue is unlikely to be crucial for activity. The high $K_{\mathrm{M}}^{\mathrm{H_2}}$ (Section 3.6.3) of D118V/E should be noted when considering their rates: saturating conditions (defined as 5x $K_{\mathrm{M}}^{\mathrm{H_2}}$) are required for the observed V_{max}, and thus $K_{\mathrm{M}}^{\mathrm{H_2}}$, to be representative of the real values; at 25 °C, however, 100% H_2 gives a H_2 concentration 780 μM in solution, which is lower than 'saturating conditions' (~1000 μM) and the data may not be accurate for these variants.

Table 3.1: Kinetic data for Hyd-1 and canopy variants. The turnover frequency is given as *k* and the % of native Hyd-1. For all variants, except D118V and D118E, the data is determined from multiple repeats on at least three different preps. The data for D118V and D118E is, therefore, subject to repeat. Note that data for R509K and D118A was produced by Sara Wehlin and Dr Rhiannon Evans and is provided here as a useful comparison for the other variants.

	Native	**D118A***	**D118V**	**D118E**	**D118N/D574N**	**D574N**	**R509K***
k (s^{-1})	257±30	66±10	2.4	14.5	50±3	212.2±38	3.3±1.1
% of Native	100	25.8	0.9	5.6	19.6	82.5	1.3
pH optimum	7	7	n.d.	n.d.	6	6	5
E_{Switch} (V *vs.* SHE)	0.242	0.148	n.d.	0.246	0.085	0.097	0.198

A change in the pH optima of Hyd-1 might be seen in D574N and D118N/D574N as the amide side chain of asparagine (Asn) is non-ionisable. The pH optima were determined electrochemically: the H_2 oxidation current of a single enzyme film was measured at a single potential (0 V for Hyd-1, −0.1 V for D574N and D118N/D574N, see below) in H_2 saturated buffer until the current stabilised; this was repeated for each pH in the range 3.0 – 9.0 and the cell solution was periodically returned to pH 6 so that film loss could be accounted for. There is a shift of one pH unit, from pH 7 for native Hyd-1 to pH 6 for both D574N and D118N/D574N (Table 3.1 and Appendix 6.2).

3.6.2 Electrocatalytic Window and E_{Switch}

At high potential, [NiFe]-hydrogenases are anaerobically inactivated as Ni-B is formed. There is a corresponding drop in the H_2 oxidation current as enzyme in the Ni-B state can no longer oxidise H_2. Thus, we observe a 'window' for H_2 oxidation which is defined by the onset potential E_{Onset} and 'E_{Switch}', the potential at which Ni-B is reductively reactivated.[124] To determine the potential window and $E_{Switch,}$ the enzyme films were first completely inactivated by holding the potential at +0.39 in pH 9 and an atmosphere of 100% Ar. After 10 000 s, the cell solution and headspace atmosphere were returned to pH 6 and 100% H_2, respectively. The potential was then scanned from high to low (+0.39 V to −0.60 V) at a very slow scan rate (0.1 mV s^{-1}).

The electrocatalytic windows for H_2 oxidation of native Hyd-1, D574N and D118N/D574N are shown in Figure 3.5A. The onset potential for all enzymes is the same for all variants as expected, given that the distal cluster controls the potential at which H_2 oxidation (or evolution) is seen.[62, 66, 69] E_{Switch} is obtained from the potential at which the minimum in the first derivative of the voltammogram is observed[14] and the data are given in Table 3.1. Differences in E_{Switch} allow us to compare the stability of Ni-B: a higher E_{Switch} indicates less reductive power is required to reductively reactivate the enzyme and thus Ni-B is less stable.

Ni-B increases in stability in the following order: native Hyd-1 ~ D118E < D574N < D118N/D574N. This is observed in the voltammograms for both D574N and D118N/D574N as the H_2 oxidation current begins to fall at much lower potentials than for Hyd-1 as Ni-B is formed. The particularly low E_{Switch} for D118N/D574N results in significant inactivation at relatively low potentials and, as a result, some data ($K_M^{H_2}$ and $\Delta H^{\ddagger}$) were restricted to potentials < 0 V. For D118N/D574N, E_{Switch} results in almost complete inactivation under conditions which do not normally favour Ni-B formation. This can be seen in Figure 3.5B, which shows that only negligible current remains at +0.24 V for D118N/D574N at pH 6 and under 100% H_2.

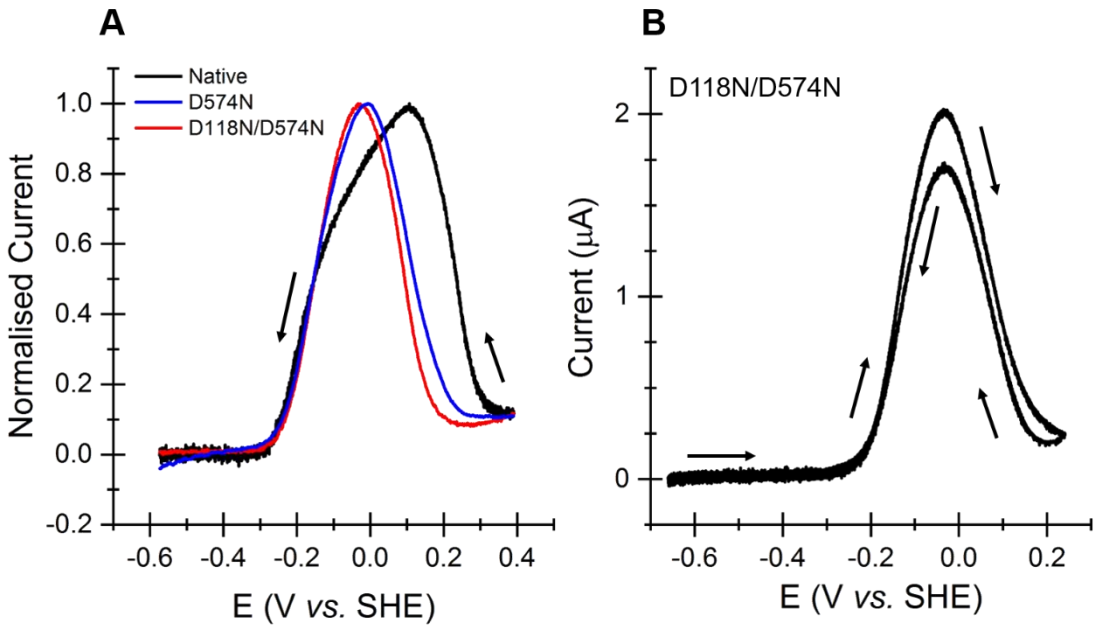


Figure 3.5: Electrocatalytic profile for H_2 oxidation by Hyd-1 and variants. A – Electrocatalytic profile of Hyd-1, D574N and D118N/D574N. The enzyme films were inactivated at pH 9 and 100% Ar by poising the potential at 0.39 V for 10,000 s. Following this, the cell buffer solution was 'exchanged' with pH 6 and the gas returned to 100% H_2. The potential was then scanned from +0.39 V to –0.60 V at a scan rate of 0.1 mV s^{-1}. E_{Switch} is the potential at which the steepest gradient occurs. **B** – Full cyclic voltammogram of D118N/D574N at 0.1 mV s^{-1} without any prior inactivation. The current is nearly completely lost. Conditions for both: pH 6, 100% H_2, total gas flow = 1000 scc min^{-1}, ω = 3000 rpm. Black arrows denote direction of potential scan.

3.6.3 Michaelis constant and activation enthalpies

The Michaelis constant, K_M, is a fundamental property describing an enzyme's affinity for substrate (Appendix 6.3). To determine $K_M^{H_2}$, cyclic voltammograms (CVs) were scanned between –0.65 V and +0.24 V at a scan rate of 5 mV s^{-1} whilst varying the H_2 in the range 0.3 – 100% H_2. Ar was used as a carrier gas, and the experiments were conducted at pH 6 and 30 °C. Prior to recording each CV, equilibration at each H_2 concentration was monitored using chronoamperometry at 0 V for Hyd-1 and –0.1 V for D574N and D118N/D574N. CVs were recorded in 100% H_2 periodically so that film loss could be accounted for. For D118E and D118V, significant film loss was seen during CVs so the current was monitored using chronoamperometry at different potentials. A Hanes-Woolf analysis was used to determine $K_M^{H_2}$. An example of the cyclic voltammograms and the subsequent Hanes-Woolf analysis is shown in Appendix 6.3. The potential-dependence of $K_M^{H_2}$ is shown in Figure 3.6. The $K_M^{H_2}$ for native Hyd-1 shows only a minor increase with potential and a similar trend is seen for D574N. For D118N/D574N and D118E, however, there appears to be a greater dependence on potential, although for D118N/D574N the trend is hidden by the inactivation at high potential. This reflects the large potential dependence seen previously for D118A.[47] Additionally, the $K_M^{H_2}$ for D118V at 0 V is more than ten times that of native Hyd-1 (215 μM and 20 μM, respectively) and, although it has not yet been determined experimentally, it suggests there is also a large potential dependence for this variant.

The activation enthalpy $\Delta H^{\ddagger}$ for H_2 oxidation was also determined for each variant using the temperature-dependence of the H_2 oxidation current. CVs were measured between –0.65 V and +0.24 V at a scan rate of 5 mV s^{-1} at different temperatures between 10 and 45 °C under 100% H_2. The temperature equilibration was monitored by recording CVs at a scan rate of 30 mV s^{-1} until they overlapped. The results of an Eyring analysis (Appendix 6.4) are shown in Figure 3.7. For Hyd-1, D574N and D118N/D574N, the current reflects the

turnover rate as the $K_M^{H_2}$ for these variants are sufficiently low that saturating conditions are achieved at 100% H_2. Rotation was also used to ensure mass transport was not rate limiting. Whilst $\Delta H^{\ddagger}$ appears to be largely potential independent for native Hyd-1, a steady decrease in $\Delta H^{\ddagger}$ as the potential increases is observed for all other variants. However, this trend is minimal for D574N and the $\Delta H^{\ddagger}$ at high potential are close to that of native Hyd-1. For D118E and D118V, there is a substantial decrease $\Delta H^{\ddagger}$ with increasing potential and this trend mirrors the substantial increase in $K_M^{H_2}$ with potential.

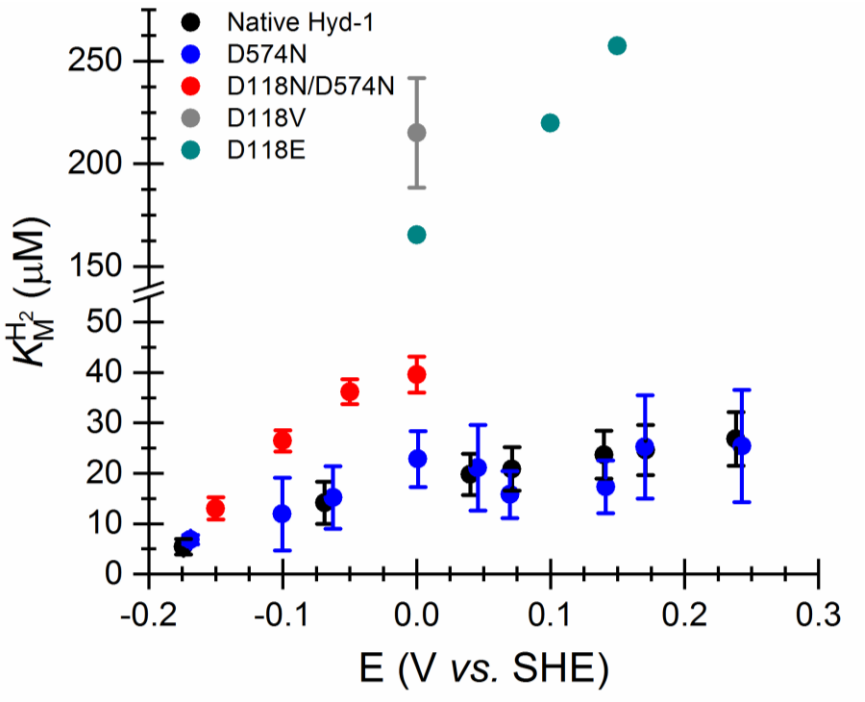


Figure 3.6: Potential dependence of $K_M^{H_2}$ for native Hyd-1 and canopy variants. Cyclic voltammograms were measured at a scan rate of 5 mV s^{-1} in the potential range –0.65 to +0.24 V, whilst varying the H_2 from 0.3 – 100% using Ar as a carrier gas. Equilibration in the different [H_2] was monitored by measuring the current at 0 V (Hyd-1) or –0.1 V (D574N and D118N/D574N). Cyclic voltammetry could not be used for D118V and D118E because significant film loss was seen during potential cycling. Instead, chronoamperometry at different potentials was used. To account for film loss, the headspace atmosphere was returned to 100% H_2 periodically. $K_M^{H_2}$was determined using a Hanes-Woolf analysis. Other conditions: pH 6, total gas flow = 1000 scc min^{-1}, ω = 3000 rpm.

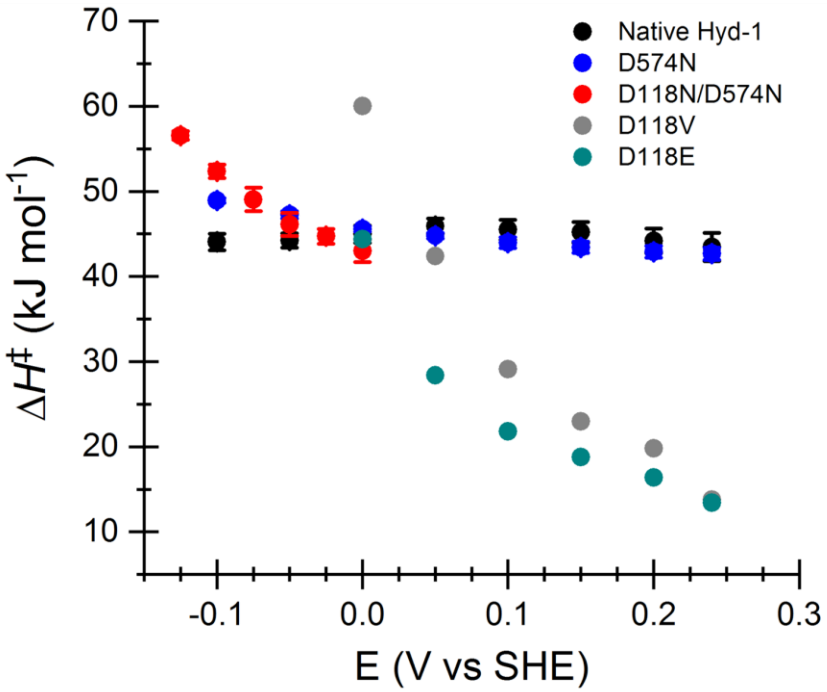


Figure 3.7: Potential dependence of *ΔH‡* for native Hyd-1 and canopy variants. Cyclic voltammograms in the potential range –0.65 V to +0.24 V were measured at a scan rate of 5 mV s^{-1}, whilst varying the temperature between 10 and 45 °C. Equilibration at each temperature was monitored by recording CVs at 30 mV s^{-1} until they overlapped. CVs were recorded at 30 °C periodically so film loss could be accounted for. Δ*H‡* were calculated by an Eyring analysis. Other conditions: pH 6, total gas flow = 500 scc min^{-1}, ω = 1000 rpm.

3.6.4 Oxygen Tolerance

A subclass of [NiFe]-hydrogenases, including Hyd-1, are capable of H_2 oxidation in the presence of O_2.[14-15] The effect of a *transient* burst of O_2 on native Hyd-1, D574N and D118N/D574N is shown in Figure 3.8. The potential was scanned from –0.40 V to +0.24 V at a scan rate of 0.5 mV s^{-1}. At +0.030 V an aliquot of O_2-saturated buffer was injected so that the final O_2 concentration was 154 μM. Rapid rotation, a high gas flow rate and the slow scan rate ensured all O_2 was flushed from the cell before the reverse scan began. For native Hyd-1, the current drops immediately following the introduction of O_2 but some current remains as the enzyme continues to oxidise H_2. Additionally, the current begins to recover before the scan direction is reversed. For both D574N and D118N/D574N, however, the

current is lost completely once O_2 is introduced and does not begin to recover until the scan has reversed.

The effect of a prolonged flow of O_2 on each enzyme was also assessed. The current response at 0 V was recorded as the O_2 was stepped from 0% to 10% (for Hyd-1) whilst maintaining a headspace atmosphere of 10% H_2 throughout. These results are shown in Figure 3.9. Hyd-1 can sustain H_2 oxidation in even 10% O_2. For D574N and D118N/D574N, however, there is a total loss of H_2 oxidation current at 6% and 4% O_2, respectively. For all enzymes, the current recovers spontaneously once the flow of O_2 is stopped and the H_2 is returned to 100%, indicating that only Ni-B/Ready states are formed under O_2/H_2 mixtures. This was further supported by the fact that minimal current at 0 V was recovered following potential steps to low potential (not shown).

E_{Switch} has already been discussed in the context of *anaerobic* inactivation but it is also relevant to *aerobic* inactivation. When O_2 is injected at +30 mV, native Hyd-1 has 210 mV driving force for Ni-B reactivation, whilst D574N and D118N/D574N have only 67 mV and 55 mV driving force, respectively. Thus, the 'O_2 injection' and 'O_2 flow' experiments were repeated at 210 mV below E_{Switch} to assess the contribution of E_{Switch} to the O_2-tolerance of D574N and D118N/D574N (−113 mV and −125 mV respectively). These are shown in Figure 3.8 and Figure 3.9.

For the 'O_2 injection' experiment, both enzymes recover immediately when O_2 is injected at the lower potential, although a second fall in current is observed as high potential drives Ni-B formation. However, the recovery is less significant for D574N. When the 'O_2 flow' experiment was repeated at lower potentials, D118N/D574N could sustain H_2 oxidation in 10% O_2. Again, D574N showed a greater sensitivity to O_2 as a steady state H_2 oxidation current was not achieved at each O_2 step and negligible H_2 oxidation current remained at 10% O_2.

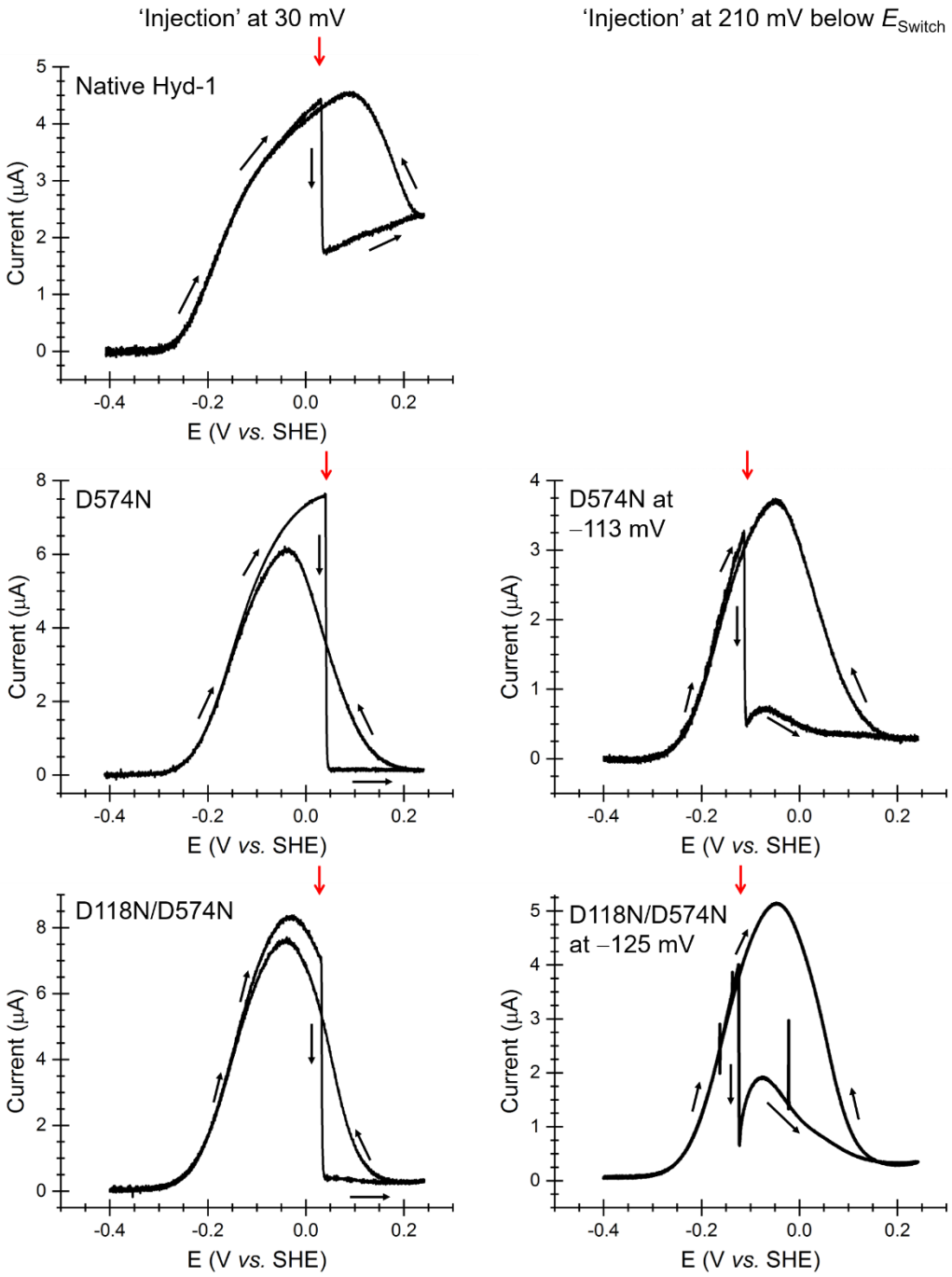


Figure 3.8: Response of H_2 oxidation to native Hyd-1, D574N and D118N/D574N to a transient burst of O_2. Left panel – Injection of O_2-saturated buffer at 30 mV. **Right panel** – for D574N and D118N/D574N, O_2 saturated buffer was injected at 210 mV below E_{Switch}. All experiments were performed as follows: cyclic voltammograms were scanned from −0.40 V to +0.24 V at a scan rate of 0.5 mV s^{-1}; at the specified potential, an aliquot of O_2-saturated buffer was injected so that the final concentration of O_2 was 154 μM. Other conditions: pH 6, 30 °C, total gas flow = 1000 scc min^{-1}, ω = 3000 rpm. Black arrows denoted direction of potential scan.

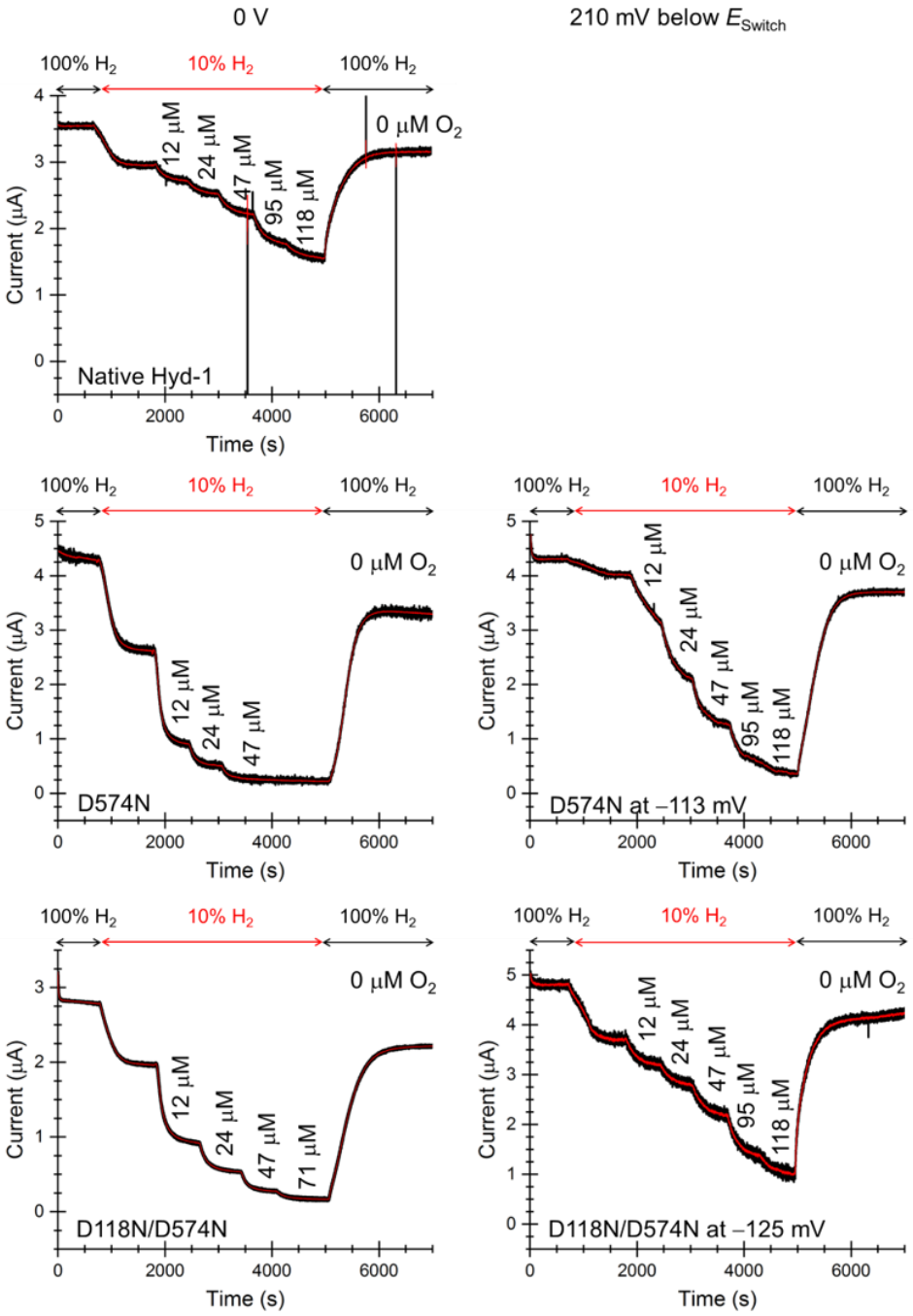


Figure 3.9: Response of H_2 oxidation by native Hyd-1, D574N and D118N/D574N to prolonged O_2 exposure. Left panel – 'O_2 flow' experiments performed at 0 V. **Right panel** – 'O_2 flow' repeated at 210 mV below E_{Switch} for D574N and D118N/D574N. All experiments were performed as follows: the current was monitored at the specified potential under 100% H_2 before switching to 10% H_2; after approximately 1100 s, O_2 was introduced and stepped from 1% to 10% (maximally); to ensure each variant was exposed to O_2 for the same length of time, the O_2 flow was stopped at 5000 s and the H_2 returned to 100%. All enzymes recovered spontaneously once the O_2 was stopped indicating that only Ni-B was formed, and differences in the starting and ending currents are attributable to film loss. The data was smoothed to highlight the potential steps. Other conditions: pH 6, 30 °C, total gas flow = 1000 scc min^{-1}, ω = 3000 rpm.

All [NiFe]-hydrogenases are reversibly inhibited by CO although the O_2-tolerant [NiFe]-hydrogenases are less sensitive than their standard counterparts.[16] The sensitivity of the variants to CO was determined by measuring the current response at –0.06 V as the CO concentration was stepped from 1% to 20%, whilst maintaining 20% H_2. A plot of $i_{\mathrm{max}}/i_{\mathrm{t}}$ versus [CO], where i_{max} is the current in 0% CO and i_{t} is the current at each CO step once stabilised, is shown in Figure 3.10. Although the double mutant is slightly more sensitive to CO, neither variant had a meaningful change in CO sensitivity and neither approached that of Hyd-2.

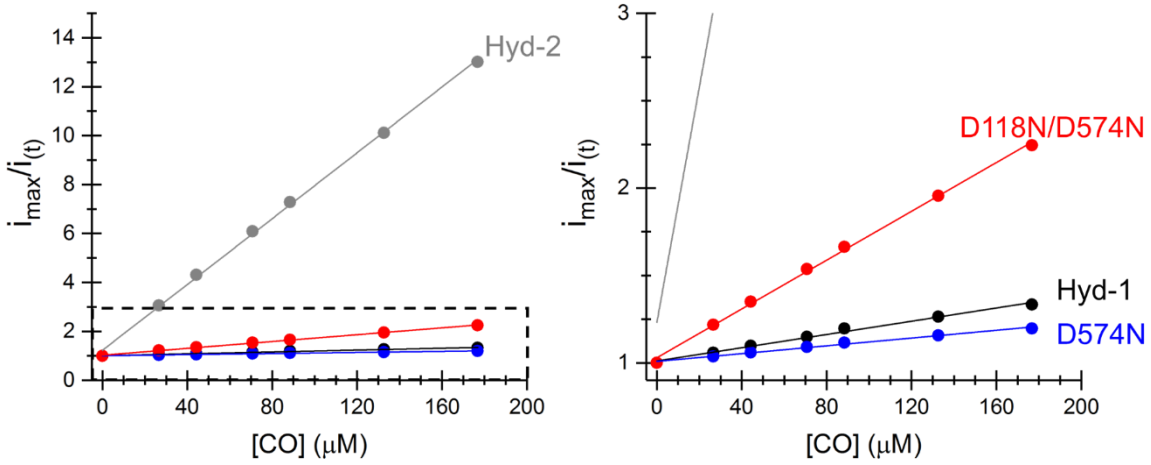


Figure 3.10: Sensitivity of native Hyd-1 and canopy variants to CO. Left panel – comparison of native Hyd-1 and variants with the standard [NiFe]-hydrogenase *Ec*Hyd-2 which is highly sensitive to CO. **Right panel** – enlargement data in dashed box to highlight differences in the canopy variants. The CO sensitivity was measured as follows: the current response at -0.06 V was measured in 20% H_2 for approximately 700 s before introducing CO; the CO was then stepped from 1% to 20% whilst maintaining 20% H_2; after 6200 s the CO flow was stopped and the current in 20% H_2 measured for a further 2000 s. Other conditions: pH 6, 30 °C, total gas flow = 1000 scc min^{-1}, ω = 3000 rpm.

3.6.5 H_2 Production

O_2-tolerant enzymes have previously been assumed to be active only in H_2 oxidation (Section 1.7). A model by Hexter *et al*[66] proposed that this is due to the difference in the potential of the electron entry/exit site (the distal cluster) and the equilibrium potential of the H^+/H_2 couple ($E_{eq}(H^+/H_2)$). Given that $E_{eq}(H^+/H_2)$ changes with both pH and $p(H_2)$ according to the Nernst equation (Appendix 6.1) but the potential of Fe-S clusters are largely pH

independent, Murphy *et al*[69] demonstrated that Hyd-1 can become a proficient H_2 producer at low pH and low partial pressures of H_2 ($p(H_2)$). The model for catalytic bias and the role of the distal cluster has been further substantiated by the work of Adamson *et al*, who produced a variant (hyaA-R193L) that had a distal cluster with a more negative potential than that seen in native Hyd-1 (–228 mV and –176 mV, respectively). The bias towards H_2 oxidation was less in the variant than in native Hyd-1, and there was also a marked decrease in the overpotential requirement for H_2 oxidation.[62] However, the catalytic bias observed in [NiFe]-hydrogenases is not solely due to the potential of the distal cluster. It is also a consequence of strong product inhibition[5] and thus D118A may be expected to evolve H_2 at greater rates than native Hyd-1 due to its high $K_{\mathrm{M}}^{\mathrm{H_2}}$ (low product affinity). The ability of D118A and other canopy variants to evolve H_2 was therefore assessed.

Cyclic voltammograms were scanned between –0.56 V and +0.26 V at a scan rate of 10 mV s^{-1} at pH 3 and 1% H_2. For R509K a modified electrode was required to amplify the small currents (Section 2.7.3). A slower scan rate (1 mV s^{-1}) and baseline subtraction were used to compensate for the large capacitive currents associated with the increased surface area of the electrode. Additionally, corrections were made to ensure the zero-current potential was not more negative than the thermodynamic potential (Appendix 6.5). It must be noted that the currents observed are dependent on film size and cannot be used to compare the relative ability of different enzymes to produce H_2 unless coverage is known. The results are compiled in Figure 3.11.

All variants, except for D118A, exhibited H_2 evolution at pH 3 and 1% H_2. This is interesting given the high $K_{\mathrm{M}}^{\mathrm{H_2}}$ of D118A which suggests this variant is less strongly product inhibited than native Hyd-1; even R509K, which has only 1% of the H_2 oxidation activity of native Hyd-1, showed substantial H_2 evolution. Figure 3.12 shows a comparison of D118A and D574N at pH 3 – 9 and 1% H_2 (note, there is some inactivation at pH 9 for both enzymes).

The onset potential for H_2 oxidation of both enzymes shifts with pH according to the Nernst equation, that is –59 mV per increase in pH unit. The D → A substitution clearly does not affect the thermodynamics of H_2 evolution (i.e. the potential of the distal cluster) as we would expect given the distance between residue 118 and the distal cluster. For D574N, H_2 evolution is seen at pH 5 and below but there is negligible difference in the currents seen for D118A at any pH.

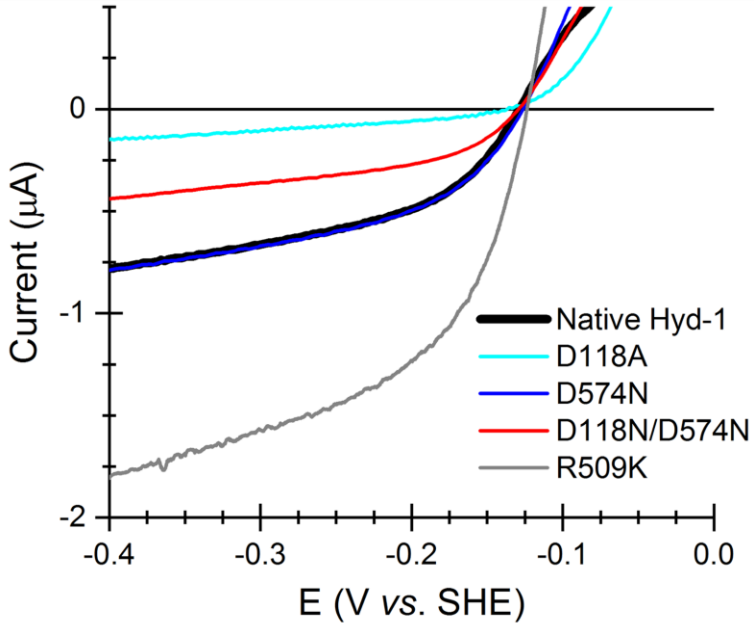


Figure 3.11: H_2 evolution by native Hyd-1 and canopy variants at pH 3 and 1% H_2. Cyclic voltammograms were scanned in the range –0.56 V to +0.26 V at 10 mV s^{-1} at pH 3 and 1% H_2 with Ar as a carrier gas. For R509K, a modified electrode was used to amplify the weak currents. Subsequently, a slower scan rate (1 mV s^{-1}) and baseline correction were required to compensate for the large capacitive currents. In all cases, the forwards and reverse scans were averaged so the zero-current potential could be identified. Note that the current amplitudes cannot be used to determine the relative ability of different enzymes to evolve H_2 as they are dependent on film size and history. Other conditions: 37 °C, total gas flow = 1000 scc min^{-1}, ω = 2000 rpm. Note: these experiments were performed by Gerri Roberts under my supervision.

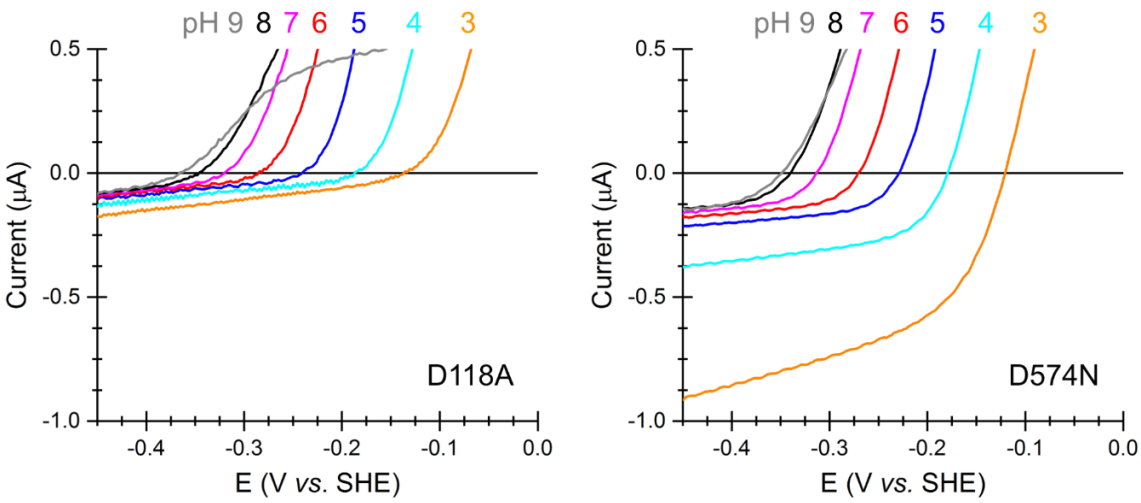


Figure 3.12: Comparison of D118A and D574N at pH 3 – 9 and 1% H_2. Cyclic voltammograms were scanned in the range –0.56 V to +0.26 V at 10 mV s^{-1} in 1% H_2 with Ar as a carrier gas. The onset potential of H_2 oxidation shifts with –59 mV (pH unit)$^{-1}$ for both enzymes but the inability of D118A to evolve H_2 in comparison with D574N is clear. In all cases, the forwards and reverse scans were averaged so the zero-current potential could be identified. Other conditions: 37 °C, total gas flow = 1000 scc min^{-1}, ω = 2000 rpm. Note: these experiments were performed by Gerri Roberts under my supervision.

3.6.6 Crystal Structures

The crystal structures of D574N and D118N/D574N were resolved to 1.23 Å and 1.1 Å, respectively (PDB: 5A4I and 5ADU). Overall both structures resemble previously published structures of [NiFe]-hydrogenases, including those of Hyd-1, and all main chain atoms could be superposed on that of native Hyd-1. The mutations did not affect the active site (Figure 3.13): the metal site was fully formed and the coordinating cysteine residues could be superposed on their equivalents in native Hyd-1. Volbeda *et al* observed oxidation of one of the metal bridging cysteines (C79), alongside a metal-bridging hydroxide, in structures of the *Df* [NiFe]-hydrogenase and this was also seen in a recent structure of a delta transmembrane variant of Hyd-1 (ΔTM).[48] This oxidation has been assigned to the previously undefined Ni-A state. D574N and D118N/D574N were also crystallised in the Ni-A state, although the amount of oxidation in the crystal was lower than was seen for native Hyd-1. For D574N and D118N/D574N, approximately 40% of C79 was oxygenated compared with 75% in the ΔTM

Hyd-1. These differences have been attributed to the time between crystallisation and cryoprotection.[48]

Given the close proximity of D118 and D574 to R509, there may be salt bridges between the carboxylate side chains and the guanidinium headgroup. Such interactions would be disrupted in the D574N and D118N/D574N variants where the negative charge of the carboxylate has been exchanged for a neutrally charged amide. A decrease in H_2 oxidation rate in these variants could, therefore, be attributed to a loss of 'pre-organisation' in the active site and increased movement of R509 such that it can no longer act as a base efficiently. It is perhaps surprising, therefore, that there is no significant movement of R509 in both D574N and D118N/D574N. In all structures, the backbone carbonyl of residue 574 is close enough to the Nε of R509 to form a hydrogen bond, which may be sufficient in stabilising the position of the guanidinium headgroup.

Changes to the conformations of the canopy side chains for both variants can be seen in Figure 3.13. In D574N, the change was minimal and results only in a slight rotation of the amide side chain to allow hydrogen bonding between the Nδ2 and Oδ1 of D118. In

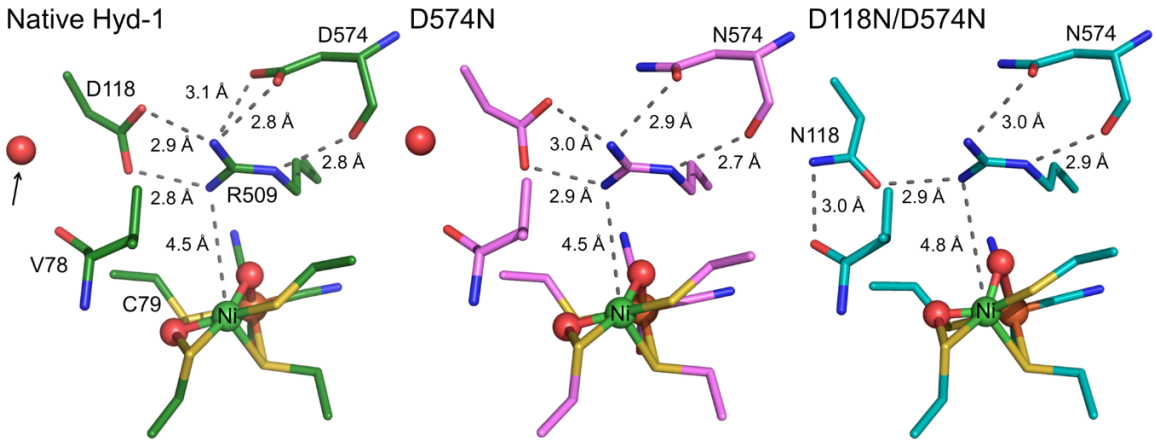


Figure 3.13: The active sites of native Hyd-1, D574N and D118N/D574N. The distances between side chains and the Ni atom are shown. The structures of native Hyd-1 and D574N include a water, indicated by an arrow, that is conserved amongst all Hyd-1 variants (and other [NiFe]-hydrogenases) but which is displaced by the rotation of N118 in D118N/D574N. PDB: 5A4M (Native Hyd-1), 5A4I (D574N), 5ADU (D118N/D574N).

D118N/D574N, the amide side chain of N118 is rotated away from R509 to minimise steric repulsion between the NHδ2 of N574 and the NHδ1 of R509. This orientation also satisfies hydrogen bonds between the Oδ1 of N118 and Nδ1 of R509, and the Nδ2 of N574 with the backbone amide of V78. A conserved water is also displaced (indicated with an arrow in Figure 3.13).

3.7 Discussion

Many functional hydrogen catalysts are active only in H_2 oxidation or evolution.[5] However, some recent hydrogenase model compounds which incorporate a second coordination sphere have exhibited reversibility.[100-101] In Hyd-1 the outer coordination spheres include D118 and D574 which form a 'canopy' above the active site with R509, and their high levels of conservation suggest they have a role in H_2 oxidation. The rate of the D118A variant (26% of native Hyd-1) indicated that whilst D118 is not crucial for activity, a significant increase in $K_{\mathrm{M}}^{\mathrm{H_2}}$ for this variant suggests it has some influence on the active site chemistry. Here, the variants D574N and D118N/D574N have been produced and investigated to further explore the role of D118 as well as the strictly conserved D574. Some data for the variants D118E and D118V is included, although further work with these variants is required.

Of the two conserved aspartates, D118 has the lower level of conservation, yet mutation of this residue has a greater effect on the rate of H_2 oxidation by Hyd-1. Indeed, the rate of D118V (< 1%) is lower than that of R509K[48] despite naturally occurring examples of valine in this position (Group 3A).[47] The decrease in turnover frequency is also more significant for the D118V and D118E (6%) variants than D118A (26%), although it is not clear why. Assuming the carboxylate of residue 118 has an active role in H_2 oxidation, we might not expect such a significant reduction in the turnover frequency of H_2 oxidation for the conservative D → E mutation as E118 could directly replace D118. Thus, the reduction in rate must be explained by structural differences having a direct or indirect consequence for

H_2 activation: any reorientation of carboxylate side chain due to the additional CH_2 group in E118 may (1) prevent it from fulfilling any active role it might have (e.g. proton transfer), (2) restrict the putative gas access channel (see below) or (3) prevent formation of crucial polar contacts. In the current set of crystal structures R509 does not move to any significant extent (within 0.3 Å of native Hyd-1), which suggests (3) is an unlikely explanation. Structural changes might also be observed in D118V given the bulky and hydrophobic nature of valine.

The order of magnitude increase and strong potential dependence of $K_{\mathrm{M}}^{\mathrm{H_2}}$ for D118A is also observed for D118E and D118V. This data supports the conclusion from D118A data that D118 is involved in controlling gas access to the active site. The large $K_{\mathrm{M}}^{\mathrm{H_2}}$ for D118A/E/V can be attributed to the relative on/off rates for H_2 binding when defining $K_{\mathrm{M}}^{\mathrm{H_2}}$ as $(k_{-1} + k_{\mathrm{cat}})/k_1$, where k_1 and k_{-1} are the on and off rates and k_{cat} is the turnover frequency. Given the strong product inhibition in [NiFe]-hydrogenases, a large $K_{\mathrm{M}}^{\mathrm{H_2}}$ would be expected to correlate with enhanced H_2 evolution if k_{-1} is large, that is if H_2 binding is *weak*. However, D118A was the only variant that did not produce H_2 at low pH and low $p(H_2)$ (note that D118E and D118V have not been assessed at the time of writing this). Instead, the high $K_{\mathrm{M}}^{\mathrm{H_2}}$ is due to a small k_1, i.e. H_2 binding is *slower* in D118A than the other variants.

The hydrophobic gas channels in [NiFe]-hydrogenases have been probed using noble gas binding and computational studies.[45-46] These channels run from the protein surface and residues E28, V78, D118 and L126 form a bottleneck that culminates at the active site (Figure 3.14). In the *Df* [NiFe]-hydrogenase, V78 and L126 were mutated to decrease the bottleneck radius, and variants had increased $K_{\mathrm{M}}^{\mathrm{H_2}}$ and altered sensitivity to CO and O_2.[125-126] These results indicate the bottleneck radius is important for regulating gas access to the active site. However, the O_2-tolerance and CO sensitivity is unchanged in the D118A variant but it is unable to evolve H_2. This suggests D118 is not simply involved in gas access.

The steady state H_2 oxidation rates of D574N (80%) and D118N/D574N (20%) are high enough to indicate that D574 is not crucial for H_2 oxidation. Additionally, it is apparent from the structures of D574N and D118N/D574N that salt bridges between D574 and R509 are not important for stabilising the position of R509. Given that this residue is strictly conserved, these results are surprising. However, O_2 inhibition studies suggest that D574 is important for Hyd-1 in the context of O_2-tolerance. O_2-tolerance relies on the ability to (1) immediately provide all four electrons required to completely reduce attacking O_2 to water and (2) rapidly reactivate the inactive Ni-B species so the enzyme can continue to oxidise H_2.[14-15, 47] The Fe-S clusters are crucial to step (1) of this mechanism and 'protect' the enzyme from becoming trapped in 'Unready' states, ensuring that Ni-B is the sole product of O_2 attack. Once this protection is in place, step (2) becomes important, and it is evident from the 'O_2 flow' experiments with Hyd-1 that there is a balance between the rate of Ni-B formation in the

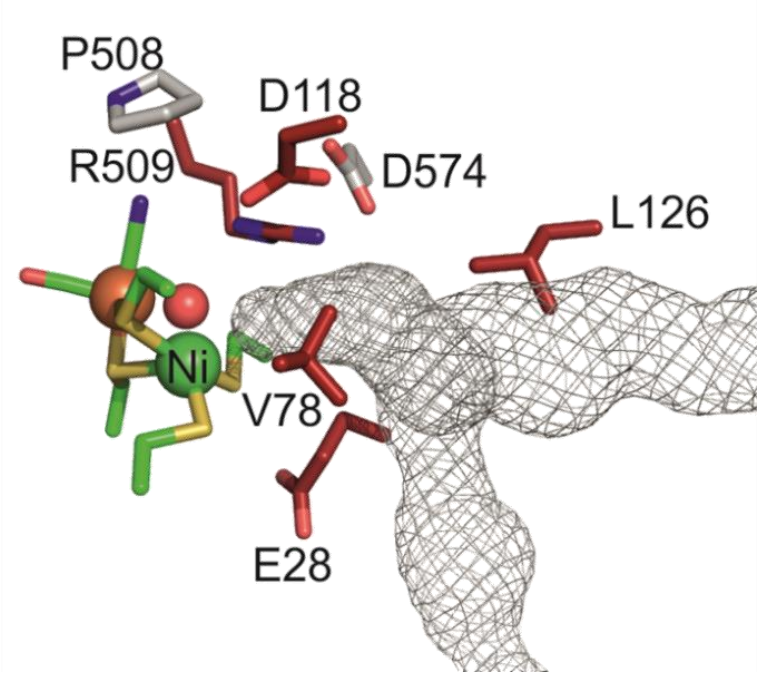


Figure 3.14: Putative gas channels in native Hyd-1, including the bottleneck residues E28, V78, D118 and L126. The two putative gas channels are shown as a mesh and were calculated using the Caver plugin for Pymol using a probe radius of 1.4 Å. Reprinted with permission from Brooke *et al*, *Biochemistry*, 2017, 56 (1), pp 132–142. Copyright 2017 American Chemical Society[47]

presence of O_2 and the rate at which the enzyme is reactivated. When a film of Hyd-1 is exposed to a continuous flow of O_2, rather than dropping to zero it reaches a steady state H_2 oxidation current as the active sites are continually oxidised and reactivated. When the O_2 is stepped to a higher concentration, a new steady state current is reached as a greater fraction of enzyme is pushed into the Ni-B state. Although D574N and D118N/D574N also achieve a steady state rate of H_2 oxidation at 0 V, the O_2 is limited to less than 6% before the current drops to zero.

To explain this observation, we must first consider the fraction of active enzyme (f)[14] and E_{Switch}. E_{Switch} is the potential at which reductive reactivation of Ni-B occurs and f is given by:[14]

$$f = \frac{rate_{\text{react}}}{(rate_{\text{react}} + rate_{\text{inact}})} \tag{3.1}$$

where $rate_{\text{react}}$ is the rate of reactivation and $rate_{\text{inact}}$ is the rate of inactivation. In Hyd-1 and the canopy variants, E_{Switch} decreases with successive removal of the negative charges: native Hyd-1 ~ D118E ~ R509K > D118A > D574N > D118N/D574N.[47] At 0 V the driving force for reductive reactivation is smaller for D574N and D118N/D574N than native Hyd-1 (+100 mV, +85 mV and +210 mV, respectively) and thus $rate_{\text{react}}$ is slower. Because the enzyme is unable to rapidly reactivate this species, at each new O_2 concentration a greater proportion of the enzyme is converted to Ni-B such that the H_2 oxidation current drops to zero before a headspace atmosphere of 10% O_2 is reached. When the experiment was repeated at lower potentials, both variants could sustain H_2 oxidation at greater O_2 concentrations. D574N appears to have a greater influence on the Ni-B stabilisation (or reactivation), as the current had dropped to zero at 10% O_2. The importance of these two residues is reflected in the E_{Switch} if we compare D118A and D574N, which have E_{Switch} potentials of 148 and 97 mV, respectively. Additionally, removal of the second negative

charge in D118N/D574N has negligible effect (13 mV) on E_{Switch}. These results signify the importance of D574 (and to a less extent, D118) in regulating the potential window for O_2-tolerant H_2 oxidation (Figure 3.15). D118 and D574 are conserved in the standard [NiFe]-hydrogenase Hyd-2 yet the E_{Switch} of Hyd-2 (+85 mV) is significantly lower than that of Hyd-1.[16] Other effects must, therefore, also be important in controlling E_{Switch}.

This work has clarified the role of D574 but the role of D118 remains elusive, beyond its having some influence on gas access to the active site. The D118E and D118V variants have already been produced and some electrochemical data has been discussed here but crystal structures and H_2 evolution studies will be crucial to understand the exact role of D118 in Hyd-1.

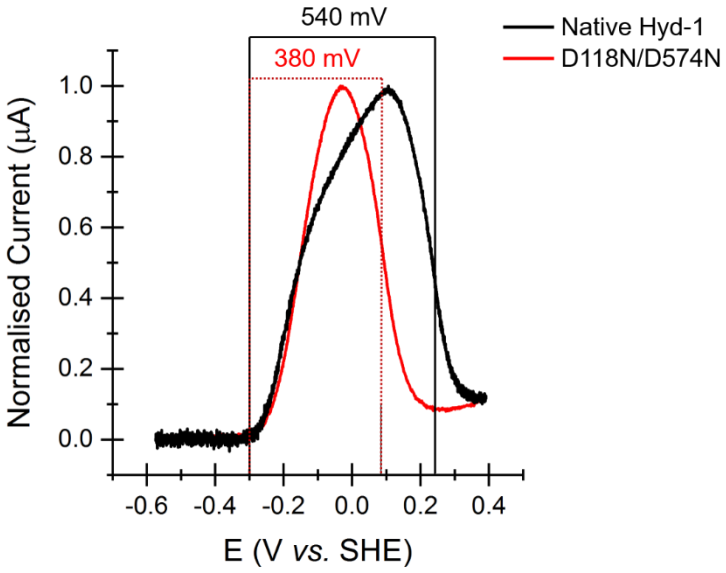


Figure 3.15: The potential window for O_2-tolerant H_2 oxidation for native Hyd-1 and D118N/D574N. The approximate potential windows are indicated and were calculated from the onset potential and ESwitch. Due to differences in E_{Switch}. Due to differences in E_{Switch} for native Hyd-1 and D118N/D574N, the potential window is far greater for native Hyd-1. Data reproduced from **Figure 3.5**

4 The role of conserved glutamate-28 in Hyd-1

4.1 Introduction

4.1.1 E28 and proton transfer

In [NiFe]-hydrogenases, glutamate-28 (Hyd-1 numbering, Figure 4.1) is *highly* conserved and has been previously implicated in proton transfer by Dementin *et al* in the *Df* [NiFe]-hydrogenase using E25D and E25Q variants (*Df* numbering).[49] The authors determined the effect of these substitutions on the different steps of H_2 activation – that is H–H bond breaking/recombination, and proton and electron transfers – by monitoring the effect of the substitutions on the following: (1) H_2 oxidation, which requires H_2 splitting, and electron/proton transfer, (2) D_2/H^+ isotope exchange, which requires H_2 splitting/recombination events and proton transfers, but not electron transfers and, (3) *para*/*ortho*-H_2 conversion, which requires H_2 splitting only. *Df* E25Q showed negligible activity (<0.1%) in both H_2 oxidation and D_2/H^+ exchange but was capable of *para*/*ortho*-H_2 conversion. On the other hand, *Df* E25D had approximately half the H_2 oxidation activity and

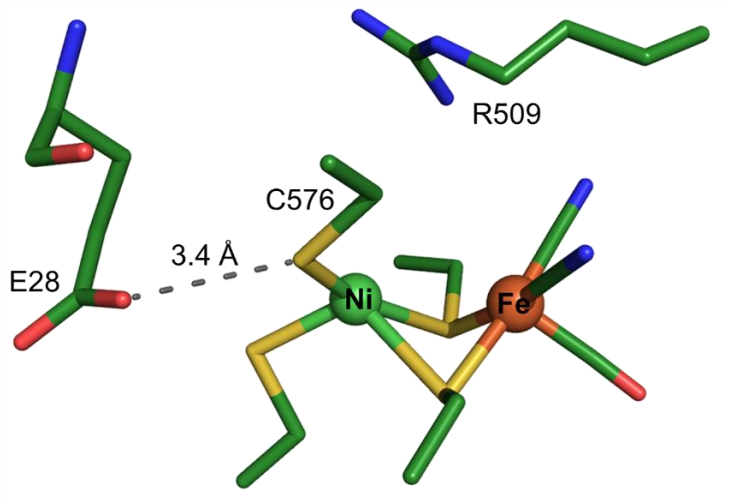


Figure 4.1: The active site of native Hyd-1 with residue E28. The distance between the Ni-thiolate ligand of C576 and the carboxylate of E28 is shown. S_{C576} is expected to be protonated in certain states of the catalytic cycle and act as a base (Section 1.10.4) or proton transfer site. R509 is included to indicate the relative position of E28 to the active site canopy (Chapter 3).

30–60% D_2/H^+ exchange activity of the native enzyme (dependent on pH). Again, the same level of *para*/*ortho*-H_2 conversion was retained in the *Df* E25D variant. *Df* E25D also had unusual spectroscopic features: signals reminiscent of Ni-L were observed in the EPR spectrum of the reduced enzyme but these signals were not photosensitive.[49] Ni-L is formed from Ni-C deprotonation, in which the hydride relocates as a proton to a nearby base leaving two electrons on the Ni to form a Ni(I) species (Section 1.9). The identity of this base remains unknown and it need not be the same base that abstracts H^+ from H_2, which is likely R509 (Figure 4.1). Three Ni-L species are seen in EPR and FT-IR spectra, indicating that multiple bases are available for the Ni-C proton.[80] Accumulation of Ni-L in the *Df* E25D variant suggests this mutation disrupts the proton transfer network close to the active site. This is supported by the observation that *Df* E25Q is essentially inactive in reactions requiring proton transfer but still capable of H_2 splitting and recombination.

Further support for E28 in proton transfer is lent by the recent work of Greene *et al* who have published several articles focusing on proton and electron transfers in [NiFe]-hydrogenases.[84-85, 88] They have demonstrated that the Ni-C to Ni-SI transition must occur via proton-coupled electron-transfer (PCET), rather than separate proton and electron transfers. Additionally, their mechanism includes the Ni-L species, which they have re-termed the 'Ni-I' state, given its role as an intermediate in the catalytic cycle, rather than simply being an artefact.[84-85, 88] Greene's proposal for the Ni-I species includes two rapidly interconverting species Ni-I^1 and Ni-I^2, which both contain a Ni-cysteine thiol but have a proton acceptor forming different hydrogen bonds.[85] Through IR and UV-Vis spectra of their E17Q variant in the soluble hydrogenase I (SHI) from *Pyrococcus furiosus* (*Pf*), Greene *et al* established that E28 acts is the proton acceptor in the Ni-C → Ni-I → Ni-SI transition, and modulates PCET (Figure 4.2).[84] For native SHI, a conversion from Ni-C to the Ni-I species, and subsequently to Ni-SI was observed in transient IR spectra. This was not the case for SHI E17Q, which remained in the Ni-I states, indicating that although the hydride photolysis was possible,

subsequent proton and electron transfer did not occur. The authors concluded that the E17Q substitution does not prevent electron transfer, for example by changing the reduction potential of the active site. Instead, proton transfer is prevented by the greatly increased pK_a of Gln compared with Glu, and this in turn abolishes PCET.[84] It should be noted that in the SHI E17Q variant, proton transfer was not completely abolished and some H_2 oxidation/evolution activity was retained. The authors proposed that the retention of activity could be due to the redirection of proton movement by a different route not including E17Q, for example via the conserved arginine discussed in Section 1.10.4.[84]

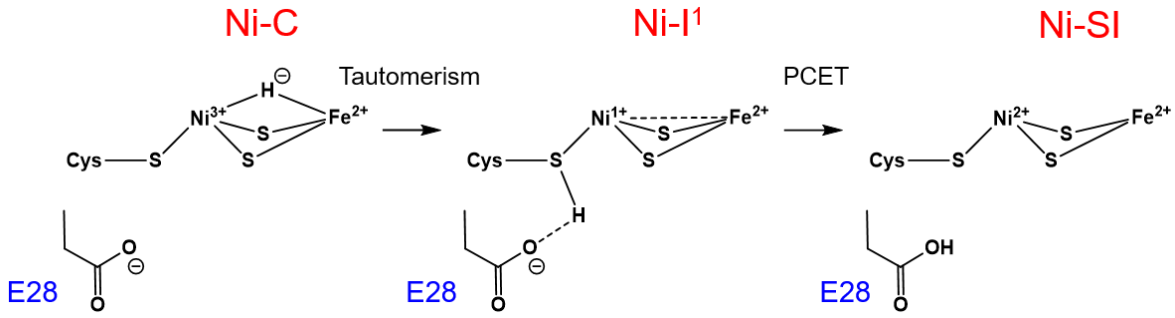


Figure 4.2: Ni-C to Ni-SI transition in [NiFe]-hydrogenases, as proposed by Greene *et al*. The Ni-C to Ni-SI transition occurs in two steps: (1) tautomerism to the rapidly interconverting Ni-I states (only Ni-I^1 is shown for clarity); (2) PCET modulated by the conserved E28 results in formation of Ni-SI. NiFe active site is shown as only the NiFe site, the bridging ligands and the terminal cysteine (C576 in Hyd-1) involved in the transition. For more information, see refs 84-85, 88.

4.1.2 In search of the Michaelis complex

The catalytic states of [NiFe]-hydrogenases (Figure 1.8) are well established and were discussed in detail in Chapter 1. These have been determined using FT-IR and EPR spectroscopies, as well as X-Ray crystallographic structures.[5] More recently, Mössbauer spectroscopy[127] and Nuclear Resonance Vibrational Spectroscopy (NRVS)[128] have also been used. Despite the wealth of information regarding the catalytic states, the 'Michaelis complex' has yet to observed. The Michaelis complex, or enzyme-substrate complex, would contain intact, bound H_2 at the active site. Thus far, there is no structural or spectroscopic data concerning the position of H_2 binding at the active site but it is expected to bind to the

Ni-SI state.[5] There are, however, several computational studies available in the literature (note that the details of the computational methods are beyond the scope of this thesis). Possible binding modes are shown in Figure 4.3. In their study of EPR silent states (Ni-SI and Ni-R), Krämer *et al* proposed two models of the Ni-R state.[129] In the first, H atoms are located on the terminal cysteine as a proton and at the metal site as a bridging hydride, a structure that is supported by the high-resolution crystal structure produced by Ogata *et al*.[81] The second Ni-R model contains H_2 bound at the Ni atom (Figure 4.3A). The consensus in the literature is that the Ni-R state contains a hydride ligand (with or without a proton at the cysteine), and so this structure may be more relevant to the active site preceding H_2 heterolysis, that is the Michaelis complex. Several other studies also conclude that Ni is the binding site. Evidence that the H_2 gas channel ends at the Ni atom, rather that the bridging position or the Fe, also lends support to these proposals.[45, 47] Others have postulated that H_2 binds to the Fe.[130] In one of these, the local energy minimum points to Fe being the initial site of H_2 binding (Figure 4.3B). However, H_2 then moves to the Ni and one H atom is shared with Fe (Figure 4.3D).[131] This appears to be the only example in which H_2 is bound to both the Ni and the Fe.

A number of these studies and results are summarised by Dong *et al* who also briefly discuss the problem with these computational studies.[130] A clear trend is seen when

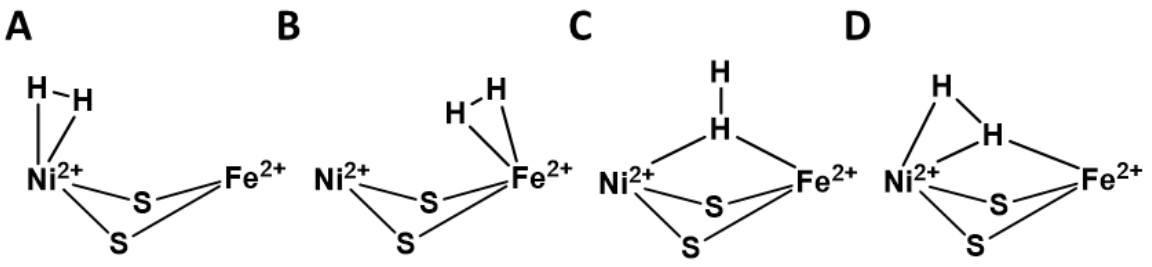


Figure 4.3: H_2 binding modes at the active site of [NiFe]-hydrogenases. A – Side-on binding to the Ni atom, Ni–(η^2-H_2) **B** – Side-on binding to the Fe atom, Fe–(η^2-H_2). **C** – H_2 bridging the NiFe active site, (μ-η^1,η^1-H_2)NiFe. **D** – the Ni coordination described in ref 130, (μ-η^2,η^1-H_2)NiFe, in which one H atom is shared with the Fe.

considering the size of the models used: studies which use larger hydrogenase models tend to favour Ni as the binding site for H_2. Given the size of [NiFe]-hydrogenases, we might expect these to be more representative of the true Michaelis complex, although none of the models approach the size of the large subunit/size of a complete hydrogenase. The results also appear to be dependent on the spin state of Ni (singlet/triplet) and the computational method used.[130]

As with proton transfer discussed in Chapter 3, elucidating the structure of the Michaelis complex is not only inherently interesting, it may also be informative for the design of functional catalysts and the mechanism of H_2 oxidation/evolution. The lack of structural and spectroscopic data for the Michaelis complex is governed by the high turnover frequencies (k_{cat}) of [NiFe]-hydrogenases, which mean that H_2 does not remain intact in the active site long enough to be captured by these techniques. However, production of a variant with sufficiently low H_2 oxidation turnover frequencies (<<1 s^{-1}) may allow the Michaelis complex to be captured using X-Ray crystallography or NRVS, but would need to be representative of the native [NiFe]-hydrogenases (i.e. fully matured with an intact active site). The Hyd-1 variant R509K (Chapters 1 and 3) has a k_{cat} reduced by two orders-of-magnitude relative to native Hyd-1 despite having a fully formed active site.[48] However, its H_2 molecules k_{cat} may still be too high (3.3 s^{-1}). In the *Df* [NiFe]-hydrogenase, the E25Q variant produced by Dementin *et al* had negligible H_2 oxidation activity[49] and the equivalent variant in Hyd-1 (E28Q) has been produced, along with an E28D variant, to assess whether it could be used to trap the elusive Michaelis complex. A recent publication by Adamson *et al* also included the Hyd-1 E28Q variant. In their PFE experiments, no H_2 oxidation or evolution current was observed and it was used to separate signals observed in FTacV experiments so that the reduction potential of the distal cluster could be determined.[62] The results here, however, suggest a more complex role for E28 than simply in proton transfer.

4.1.3 Contributions to this thesis

The E28Q and E28D strains were made by Dr Rhiannon M. Evans (RME). Solution assays were performed by myself. For E28D, all PFE was performed by Alexander Bridgeman (AB) under my supervision and were repeated by myself. For E28Q, all PFE was performed by myself. For the EPR spectroscopy, EJB produced the enzymes and prepared the samples. EPR spectra were collected with the help of Dr Kourosh H. Ebrahimi. The X-Ray crystal structures were produced as follows: EJB and AB produced enzyme samples with the help of Elena N; AB set up crystal trays with the help of Dr Stephen B Carr (SBC); SBC collected data and built models. The unusual activity at high pH and high potential of E28Q was not recognised until late in this project so data is limited at this time. Work is currently on going by RME.

4.2 Results

4.2.1 Turnover frequency and electrocatalytic profile

The steady-state H_2 oxidation turnover frequencies of E28Q and E28D (Table 4.1) were measured using conventional solution assays using methylene blue as an electron acceptor, as described in Section 3.6.1. The H_2 oxidation activities at pH 6 and 25 ^{o}C of E28Q and E28D are 0.74% and 41% of native Hyd-1, respectively. For the equivalent E28D variant in the *Df* [NiFe]-hydrogenase, there was negligible H_2 oxidation activity remaining at pH 6 and the maximal activity (~ 40%) was seen at pH 8.5.[49] The electrocatalytic profile for E28D shows an unexpected increase in overpotential for H_2 oxidation in comparison with native Hyd-1 (Figure 4.4), although at high potentials the current-potential profile can be overlain with that of native Hyd-1. This is also reflected in the E_{Switch} of E28D which is 0.245 V, compared with 0.242 V for native Hyd-1 (Section 3.6.2).

Table 4.1: Turnover frequencies of H_2 oxidation for native Hyd-1, E28Q and E28D at pH 6 and 25 ºC. Turnover frequencies are given as k_{cat} (s^{-1}) and μmol H_2 min^{-1} (mg enzyme)$^{-1}$.

	Native Hyd-1	E28Q	E28D
k_{cat} (s^{-1})	257.4 ± 30.4	1.9 ± 0.2	105.9 ± 9.1
μmol H_2 oxidised min^{-1} (mg enzyme)$^{-1}$	153.9 ± 18.2	1.15 ± 0.1	63.3 ± 5.4
% native Hyd-1	100	0.74	41

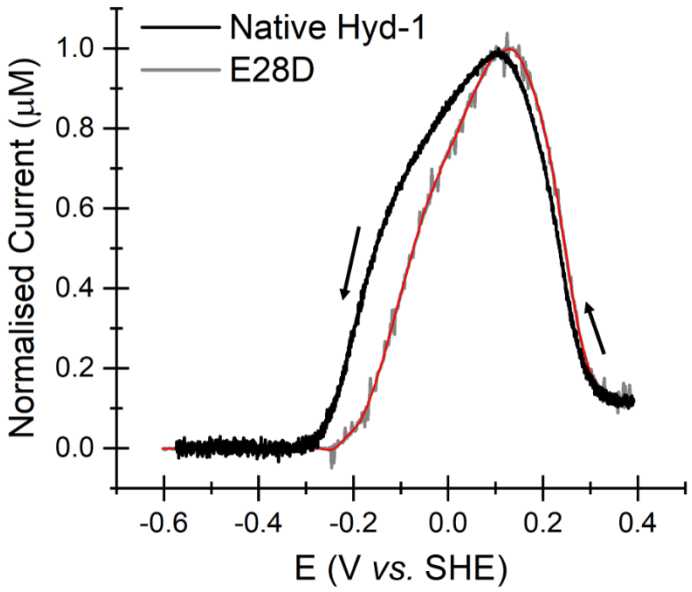


Figure 4.4: Electrocatalytic profile of native Hyd-1 and E28D. The enzyme films were inactivated at pH 9 and 100% Ar by poising the potential at 0.39 V for 10,000 s. Following this, the cell buffer solution was exchanged with pH 6 and the gas returned to 100% H_2. The potential was then scanned from +0.39 V to –0.60 V at a scan rate of 0.1 mV s^{-1}. E_{Switch} is the potential at which the steepest gradient occurs. Conditions: pH 6, 100% H_2, total gas flow = 1000 scc min^{-1}, ω = 3000 rpm.Black arrows direction of potential sweep. For E28D, a smoothed curve is shown in red. Note: data for native Hyd-1 is the data from Figure 3.5.

4.2.2 Michaelis Constant and Activation Enthalpy of E28D

The Michaelis constant ($K_M^{H_2}$) and activation enthalpy for H_2 oxidation ($\Delta H^{\ddagger}$) for E28D were determined using the methods described in Section 3.6.3 and are shown in Figure 4.5. Regarding $K_M^{H_2}$, for E28D there is a rapid increase with potential above 0 V such that at high potential the $K_M^{H_2}$ is 5-6 times greater than that of native Hyd-1. At low potential, $\Delta H^{\ddagger}$ for E28D

is raised slightly compared with native Hyd-1. However, as the potential increases Δ*H*‡ begins to drop, reflecting the increase in $K_M^{H_2}$.

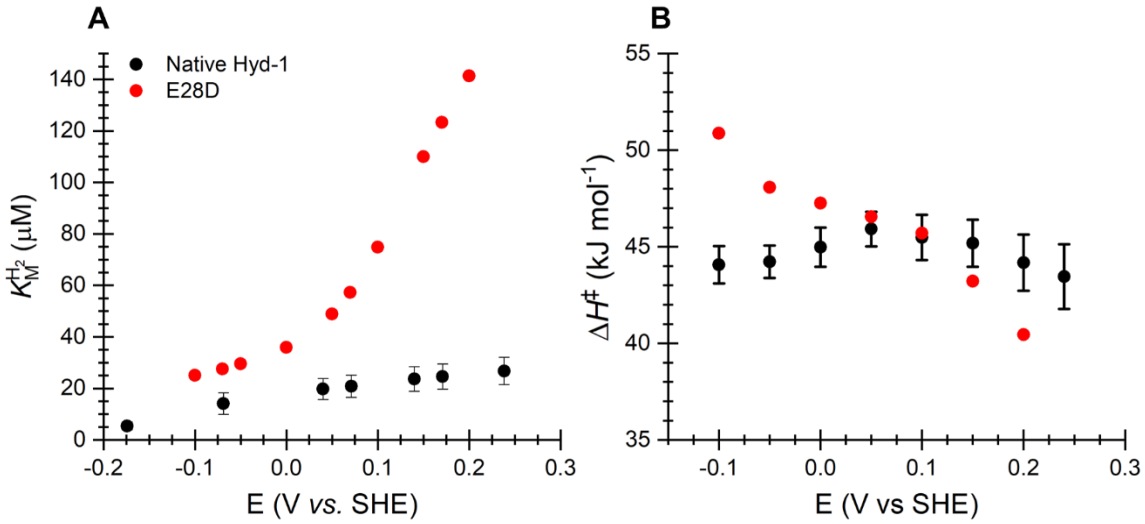


Figure 4.5: The potential dependence of the Michaelis constant $K_M^{H_2}$ and the activation enthalpy Δ*H*‡ for native Hyd-1 and E28D. A – The potential dependence of $K_M^{H_2}$. Method and native Hyd-1 data same as for Section 3.6.3 and Figure 3.6 **B** – The potential dependence of Δ*H*‡. Method and native Hyd-1 data same as for Section 3.6.3 and Figure 3.7.

4.2.3 Kinetic Isotope Effect of E28D

The H_2/D_2 kinetic isotope effect (KIE) for native Hyd-1 and E28D were measured (Figure 4.6): the current response at three potentials (0 V, +0.15 V and –0.15 V) was measured first under a flow of 100% H_2 and then 100% D_2; before changing the potential, the current was monitored until it stabilised; this was repeated three times and a fourth potential hold at 0 V under H_2 was performed; the data at 0 V under H_2 was then used to account for film loss. The KIE was calculated using i_{H_2}/i_{D_2}.

The small KIE for native Hyd-1 has been reported previously[132] and signifies that H–H bond breaking is not the rate determining step under these conditions. There is only slight

variation with potential. There is a small decrease in the KIE for E28D at all potentials: at 0 V the KIEs are 1.37 and 1.23 for native Hyd-1 and E28D, respectively.

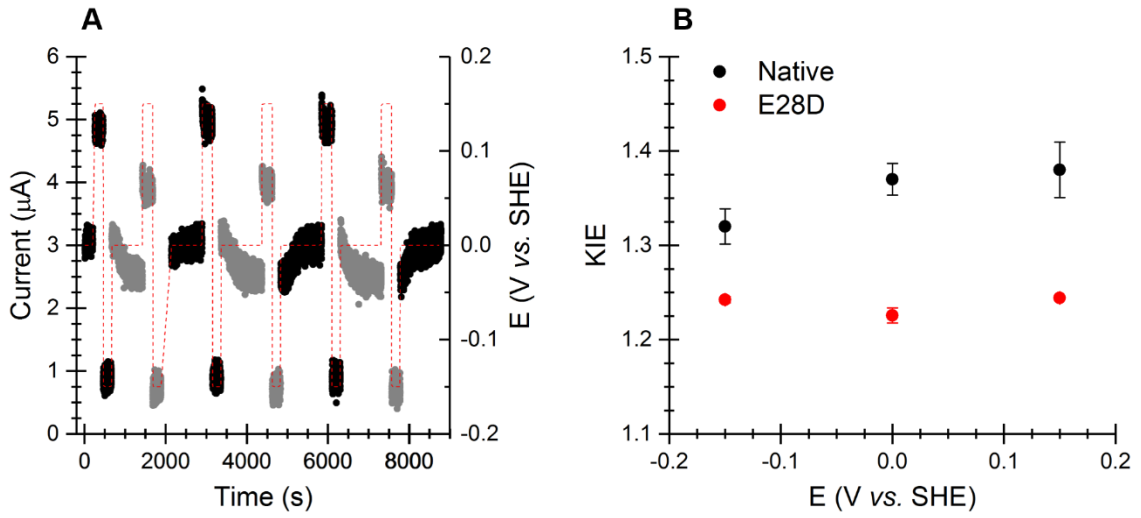


Figure 4.6: H_2/D_2 Kinetic Isotope Effect (KIE) for native Hyd-1 and E28D. A – An example experiment for E28D following film loss correction. The potential was stepped between 0 V, +0.15 V and –0.15 V (dashed red line) under a flow of H_2 (black) then D_2 (grey). The current response at 0 V under H_2 was measured four times and this data was used to correct for film loss. **B** – Potential dependence of the KIE for native Hyd-1 and E28D. The KIE was calculated using i_{H_2}/i_{D_2}. For native Hyd-1, error is the standard error of the mean calculated from three separate experiments in which the potential steps were repeated 2-3 times. For E28D, the error is the standard error or the mean of three potential step repetitions in the same experiment. Other conditions: pH 6, 30 °C, total gas flow = 200 scc min^{-1}, ω = 2000 rpm.

4.2.4 Response of E28D to O_2 and CO

Given the postulated role of E28 in proton transfer, variants with a disrupted H^+ pathway may be expected to have greater sensitivity to O_2 because H^+ is essential for rapid O_2 reduction and the formation of the Ni-B state instead of other inactive species (Section 1.8).[14-15] The 'O_2 flow' and 'O_2 injection' experiments[14] described in Section 3.6.4 were used to assess the ability of E28D to cope with attacking O_2 (Figure 4.7). It is immediately apparent that E28D has a lower tolerance for O_2 than native Hyd-1 despite negligible differences in E_{Switch} for the two enzymes. In the O_2 flow experiment, a steady-state H_2 oxidation current is not established at each O_2 step and the current does not recover once the O_2 is removed.

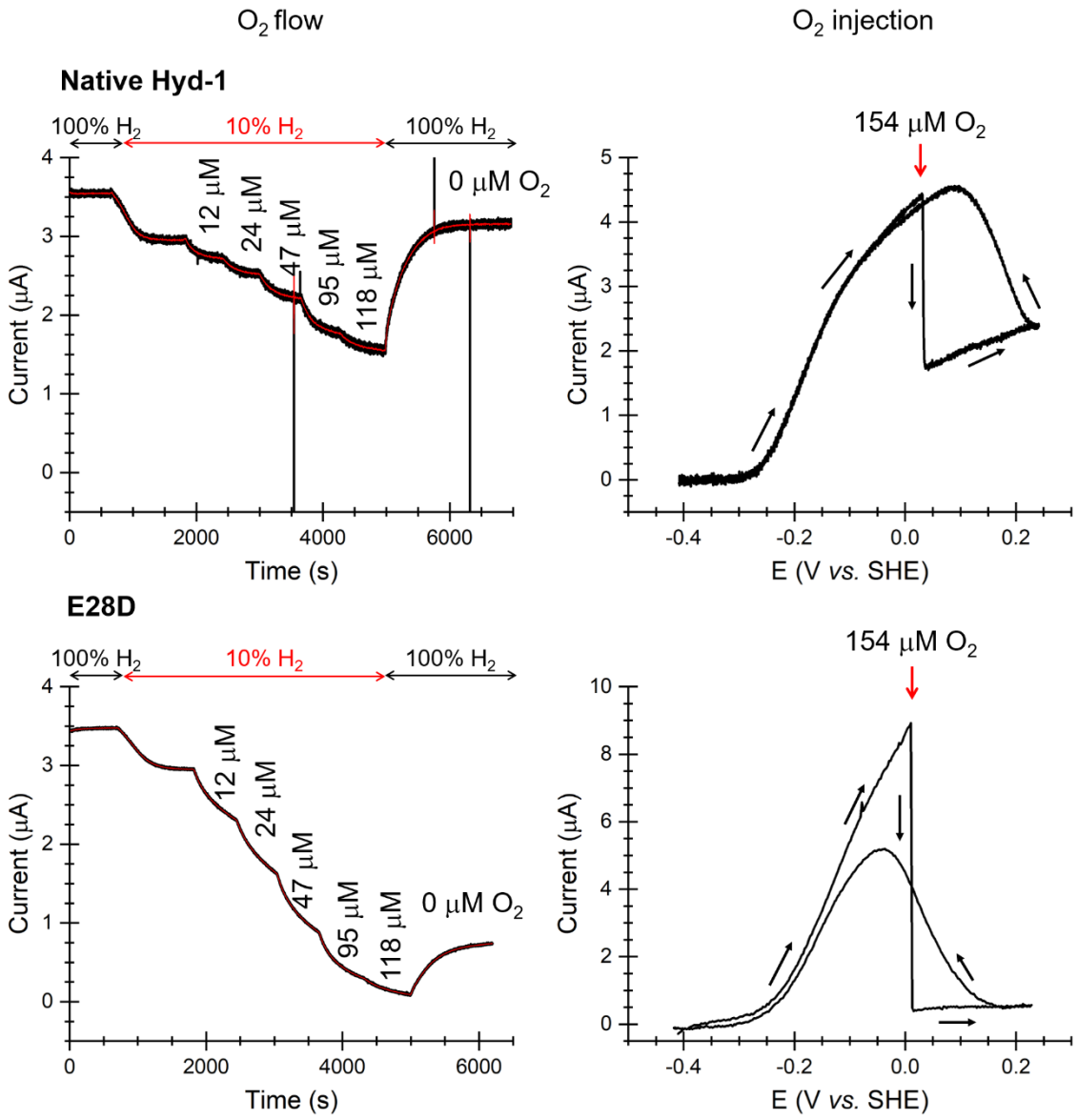


Figure 4.7: Response of native Hyd-1 and E28D to O_2. Left panel – O_2 flow experiments at 0 V for native Hyd 1 (upper) and E28D (lower). The current was monitored at 0 V under 100% H2 before switching to 10% H_2; after approximately 1100 s, O_2 was introduced and stepped from 1% to 10%; to ensure each variant was exposed to O_2 for the same length of time, the O_2 flow was stopped at 5000 s and the H_2 returned to 100%. Unlike native Hyd-1, little H_2 oxidation current is recovered for E28D once the O_2 is removed. **Right panel** – O_2 injection experiments for native Hyd-1 (upper) and E28D (lower). Cyclic voltammograms were scanned from -0.40 V to +0.24 V at a scan rate of 0.5 mV s-1; at 30 mV, an aliquot of O_2-saturated buffer was injected so that the final concentration of O_2 was 154 μM. Rapid rotation and the slow scan rate ensured all O_2 was removed before the reverse scan began. Other conditions for both: pH 6, 30 °C, total gas flow = 1000 scc min^{-1}, ω = 3000 rpm.Black arrows denote direction of potential scan. Note: data for native Hyd-1 is the data from Figure 3.8 and Figure 3.9.

This suggests a significant fraction of the enzyme is in the Ni-A state (note that it is not possible to correct for film loss during O_2 inhibition studies due to irreversible enzyme inactivation under these conditions). In the O_2 injection experiment, the H_2 oxidation current is completely lost for E28D. It does not begin to recover until the reverse scan has begun and despite the high E_{Switch}, the current does not begin to recover until the potential is lowered below 0.2 V. The E28D substitution has little impact on the CO sensitivity of Hyd-1 (Appendix 6.6).

4.2.5 pH profile of E28Q

In initial electrochemical studies with E28Q, little catalytic activity was seen within the 'standard' potential range used to study [NiFe]-hydrogenases (–0.65 V to +0.24 V). This reflects the low turnover rates seen in the solution assays (Table 4.1), using methylene blue which, at pH 6, has a redox potential of approximately 70 mV[133]. When the film size was

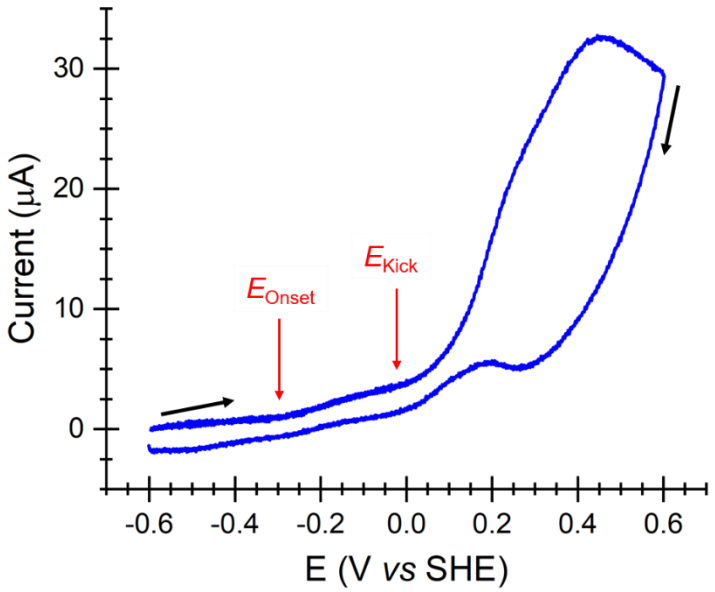


Figure 4.8: Cyclic voltammetry of E28Q at pH 6 and 37 ºC. The onset potential E_{Onset} and the threshold potential E_{Kick} are shown with arrows. Cyclic voltammograms were scanned in the range –0.60 V to +0.60 V at a scan rate of 5 mV s^{-1}. Other conditions: 100% H_2, total gas flow = 1000 scc min^{-1}, ω = 2500 rpm, film was grown on a modified electrode (Section 2.7.3). Black arrows denote scan direction.

increased using modified electrodes (Section 2.7.3) and the potential range increased, however, large H_2 oxidation currents were observed for E28Q (Figure 4.8). Initially, the H_2 oxidation current increases slowly but once a threshold potential is reached – referred to here as E_{Kick} – the current increases rapidly before inactivation occurs at high potential.

Given this unexpected result, the activity of E28Q was measured at each pH in the range 4 – 10 (pH 3 was not included due to decreased film stability). Cyclic voltammograms were recorded in the potential range –0.60 V to +0.60 V at a scan rate of 5 mV s^{-1} under 100% H_2 and at pH 6. The cell solution was then exchanged with buffer at a different pH that had been pre-equilibrated in 100% H_2. After each pH, the cell solution was returned to pH 6 so that film loss could be accounted for. The results are shown in Figure 4.9. Two characteristics are apparent in the pH dependence of E28Q. Firstly, the activity of E28Q increases with increasing pH, if we disregard inactivation. The pH optimum of E28Q has clearly increased from pH 7 in native Hyd-1,[48] although at high pH (≥ 7) inactivation is rapid and so any trends

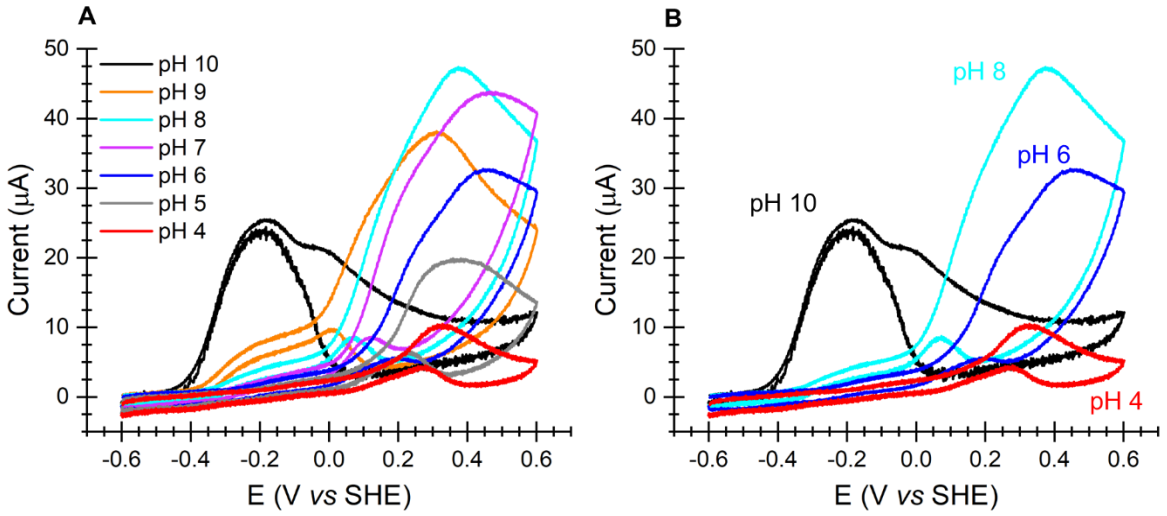


Figure 4.9: pH dependence of electrocatalytic H_2 oxidation by E28Q. A – Cyclic voltammograms recorded in pH 4 – 10. **B** – Data is identical to that in panel A but only pHs 4, 6, 8 and 10 are shown for clarity. Cyclic voltammograms were recorded in the potential range –0.60 V to +0.60 V at a scan rate of 5 mV s^{-1} under 100% H_2 and at pH 6. The cell solution was then exchanged with buffer at a different pH that had been pre-equilibrated in 100% H_2. After each pH, the cell solution was returned to pH 6 so that film loss could be accounted for. Other conditions: 37 °C, 100% H_2, total gas flow = 1000 scc min^{-1}, ω = 2500 rpm, film was grown on a modified electrode (Section 2.7.3).

are masked by Ni-B formation. At pH 10 the current takes off rapidly once H_2 oxidation begins and the current reached before E_{Kick} is far greater than at the other pHs. For pH 7-9, the initial increase in activity is much slower but once E_{Kick} is reached, the current takes off rapidly. Secondly, at pHs 4 and 5 there is no obvious rapid increase in current once the current has exceeded E_{Kick}. The occurrence of a second 'onset' potential implies that the role of E28 may not solely be due to proton transfer but it may also influence the electronics of H_2 oxidation by [NiFe]-hydrogenases. It is worth noting that the approximate pH dependence of E_{Kick} is approximately 29 mV per pH unit which signifies E_{Kick} is a $2e^-$, $1H^+$ process (Appendix 6.7).

4.2.6 Response of E28Q to O_2 and CO

The ability of E28Q to oxidise H_2 in the presence of O_2 and CO was assessed. However, due to difficulties in growing and maintaining films of E28Q, even with covalent attachment to the electrode surface, this was assessed using only injection experiments. These experiments were performed at 37 ^oC and pH 7, instead of the typical 30 ^oC and pH 6 conditions used for Hyd-1, to amplify the currents produced by E28Q films. Modified electrodes were also used but currents remain relatively weak (~10 μA) even at 37 ^oC when compared with native Hyd-1 films.

The O_2 injection method has been described elsewhere (Section 3.6.4)[14] but here the potential was altered from +30 mV to -29 mV to account for the pH change. For E28Q, the current drops immediately when O_2 is injected (Figure 4.10A). At this potential, O_2 reduction by the electrode is also observed but the current quickly returns to zero. The H_2 oxidation current does not begin to recover until the reverse scan begins, although the potential at which recovery begins is higher than that for E28D (~0.25 V).

For native Hyd-1 and variants, CO experiments are typically performed at −60 mV.[15-16] This potential is below E_{Kick} and so was also used for the CO injection (adjusted for pH 7 to −118 mV). Cyclic voltammograms were scanned from -0.45 V to +0.60 V at a scan rate of

0.5 mV s-1. At –118 mV, an aliquot of CO-saturated buffer was injected so that the final concentration of CO was 134 μM. Although a small fall in current can be seen, at this potential E28Q was able to recover immediately so a second CO injection was performed but at a potential above E_{Kick} (Figure 4.10B). The second aliquot of CO was injected at +153 mV such that the concentration of CO in the cell was increased by 115 μM. At the higher potential, the fall in current is much greater and does not begin to recover until around 0.25 V as with the O_2 injection. CVs before and after the CO injection are also shown in Figure 4.10B to demonstrate the amount of film loss seen between the CVs.

Although we expect significant inactivation of [NiFe]-hydrogenases at high potential, Figure 4.10 demonstrates the 'additional' inactivation caused by the small molecule inhibitors. For the O_2 experiment, the total loss of current signifies that all the film is

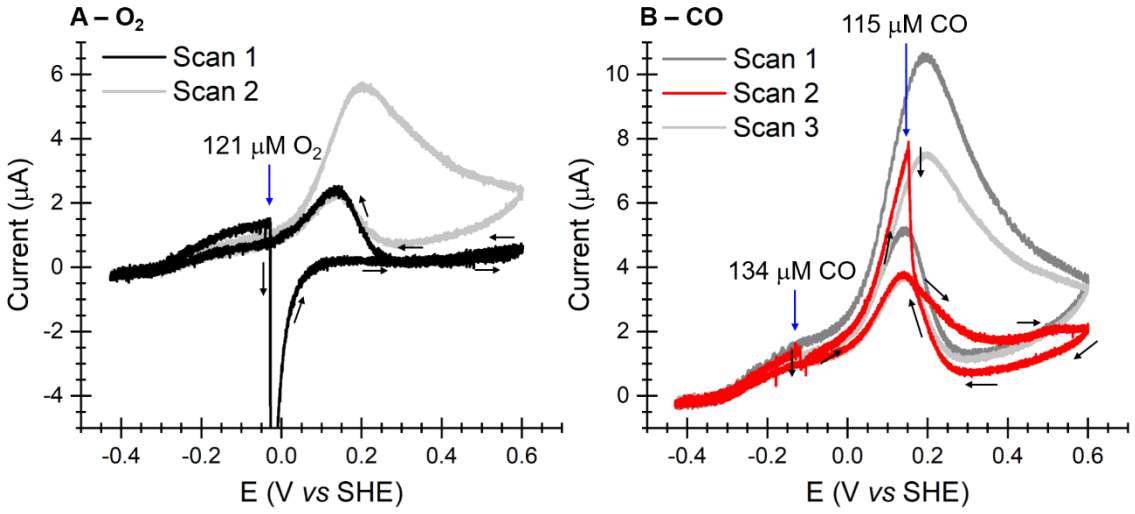


Figure 4.10: Response of E28Q in the presence of small molecule inhibitors. Blue arrows indicate injection points. Black arrows represent direction of the potential scan. **A** – O_2 injection experiment. Cyclic voltammograms were scanned from -0.45 V to +0.60 V at a scan rate of 0.5 mV s-1; at –29 mV, an aliquot of O_2-saturated buffer was injected so that the final potential of O_2 was 121 μM. O_2 reduction by the electrode can be seen. **B** – CO injection experiment. Cyclic voltammograms were scanned from –0.45 V to +0.60 V at a scan rate of 0.5 mV s^{-1}; at –118 mV, an aliquot of CO-saturated buffer was injected so that the final concentration of CO was 134 μM. As the current recovered immediately, a second aliquot of CO was injected at +153 mV such that the CO concentration was increased by 115 μM. Rapid rotation, continual flow of H_2 through the cell and the slow scan rate ensured all O_2 or CO was removed before the reverse scan began. Other conditions for both: pH 7, 37 °C, total gas flow = 1000 scc min^{-1}, ω = 3000 rpm.

inactivated. This is not the case when the enzyme is inactivated anaerobically at high potential (Figure 4.10A, Scan 2). The same is true for the CO experiment. Significant inactivation is seen at high potential for E28Q in 'before' and 'after' scans (Figure 4.10B, Scans 1 and 3 respectively) but the current at these potentials immediately following the CO injection (Scan 2) is decreased further.

4.2.7 EPR Spectra

The EPR spectra of E28D and E28Q were measured at both 70 K and 15 K (Figure 4.11). Spectra at the latter temperatures are required to measure the Fe-S clusters, which relax too rapidly to be seen at 70 K. The distal cluster is not seen in EPR spectra of Hyd-1, although the reason for this is not clear.[64] The samples are labelled 'as isolated', 'H_2 activated' and 'Ar purge' and correspond to enzyme that has been aerobically purified, enzyme that has been activated under a flow of H_2 for 48 hours and enzyme that has then been flushed with Ar for 48 hours to remove H_2, respectively. All samples were prepared in a glovebox and removed from the glass cell using a gas tight Hamilton syringe. EPR tubes were equilibrated in the relevant gas (H_2 or Ar) for at least 10 minutes prior to sample preparation.

The as isolated spectra at 70 K of both variants do not show the presence of any defined Ni states. This has been seen previously in as isolated spectra of native Hyd-1[134] and is likely due to there being a mixture of states present. For both variants, the complex signal associated with the antiferromagnetically coupled proximal superoxidised $[4Fe3S]^{5+}$ and medial oxidised $[3Fe4S]^{+}$ clusters is observed in the as isolated spectra at 15 K. In as isolated native Hyd-1, only the signal from the medial cluster is observed,[64, 134] although we must remember that the potential of the E28D and native Hyd-1 samples is unknown.

Following H_2 activation, Ni-L is observed for E28D and the active site remains in this state following the Ar purge. Interestingly, however, the distribution of Ni-L states is different compared with those seen for native Hyd-1.[86] The observation of multiple Ni-L states has

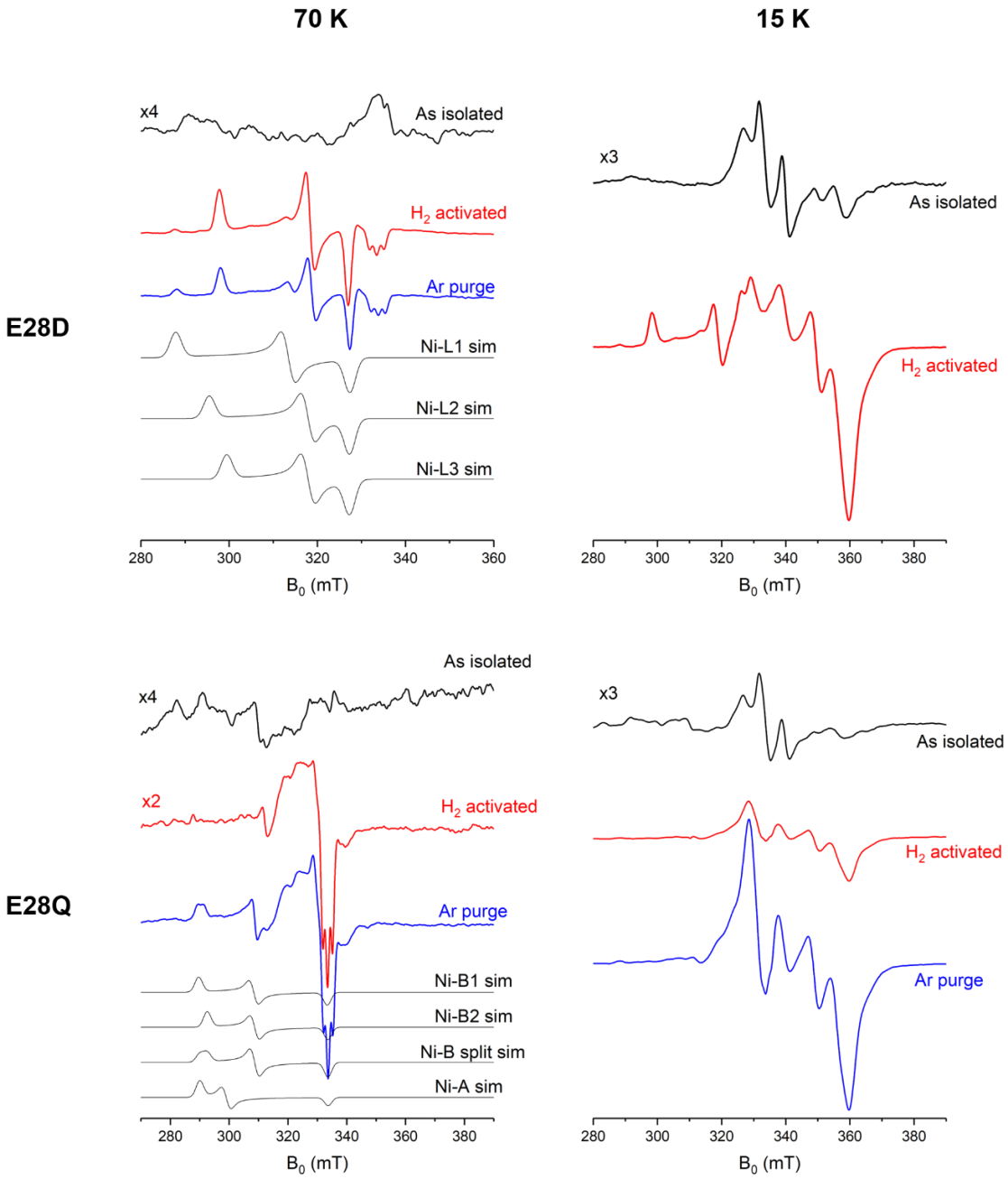


Figure 4.11: X-band EPR spectra of E28D (upper) and E28Q (lower) at 70 K (left) and 15 K (right). All samples were prepared in an anaerobic glove box. Once the 'as isolated' sample was (aerobically purified enzyme) prepared, each enzyme was activated for 48 hours under a flow of 100% H_2 before a second sample was taken ('H_2 activated'). Following this, the H_2 was flushed out using a flow of Ar for 48 hours before taking the third sample ('Ar purge'). The 70 K spectra include simulations of Ni species. A background spectrum using buffer was measured and used to do a background subtraction. All samples were frozen and stored in liquid N_2. Unfortunately, a problem with storage meant that the 'Ar purge' sample for E28D was lost between taking the 70 K and 15 K samples (taken on different days). Conditions: samples prepared at 25 ^{o}C, total gas flow = 100 scc min^{-1}, buffer conditions = 100 mM MES, 150 mM NaCl & pH 6, microwave power = 2 mW, field frequency = 9.38 GHz, 4 mm low precision tubes.

been attributed to differences in the position of protonation following hydride loss from Ni-C.[80] The three Ni-L states are simulated in the 70 K spectrum of E28D. Native Hyd-1 typically hasa higher proportion of Ni-L1 and only small fractions of the other two states.[86] For E28D, most of the sample is in the Ni-L3 state but after the Ar purge, the proportion of Ni-L1 appears to increase.

Although the states present in the 70 K spectrum of E28Q are not clear, all signals are lost following H_2 activation indicating that the enzyme is trapped in EPR silent states such as Ni-SI or Ni-R. This is in contrast to the *Df* E25Q enzyme for which Ni-C was seen in the reduced spectrum. Once the H_2 is removed, E28Q converts to the Ni-B state. As has been seen for native Hyd-1 previously, the Ni-B is a 'split' signal of two Ni-B states with different g_x values.[134]

On H_2 activation, the clusters are reduced indicating that the enzyme samples are fully activared, and only the proximal $[4Fe3S]^{3+}$ state is observed. The reduced $[3Fe4S]^{0}$ cluster is not observed by EPR spectroscopy. Unfortunately, the 70 K and 15 K spectra were recorded on separate occasions, dictated by the availability of the EPR machine, and in between a problem with storage resulted in the loss of the E28D Ar purge sample.

4.2.8 Crystal Structures

The crystal structures of E28D and E28Q were produced to 1.4 Å and 1.2 Å resolution, respectively and are the first structures of E28 variants. The structures included in the work by Dementin *et al* are not of their own variants *in vitro*[49] and, instead the mutations were introduced computationally. Overall, the structures of both variants are similar to that of native Hyd-1. For E28Q, there is also negligible impact on the active site (Figure 4.12) as there is only slight movement of Q28. However, this is not the only conformation of Q28 and an additional water molecule (red arrow) sits in the same position in approximately 30% of the enzymes in the crystal. The same oxygenation is observed on C79, as in native Hyd-1.

The changes are more drastic for E28D (Figure 4.12). The carboxylate of D28 is rotated towards the active site which results in changes to the loop containing D28. Additional waters (red arrows) are present and form a chain through the active site. A striking difference is the unusual oxygenation at the active site: the thiol of C576 is oxygenated twice. In the structures of native Hyd-1 and canopy variants, there is no oxygenation of C576 and the active site is crystallised in the Ni-A state, that is with a bridging hydroxide and sulfonate at C79.[48] Additionally, the active site does not appear to be intact as some of the metal-S bonds are broken.

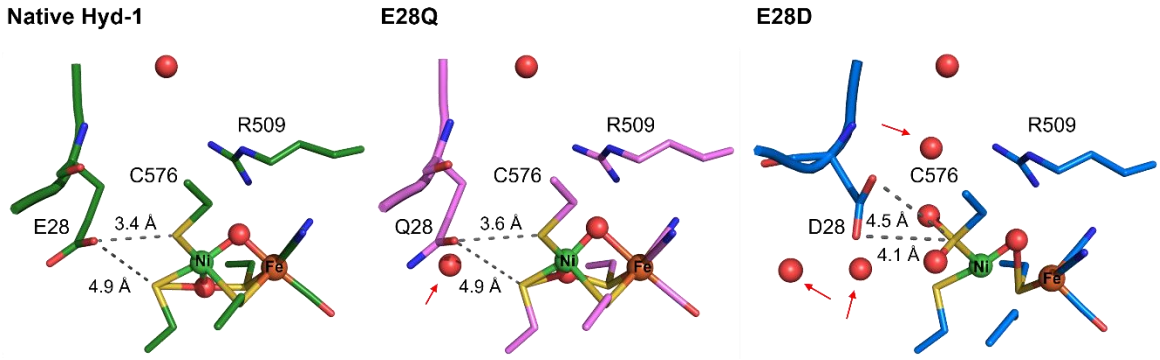


Figure 4.12: Crystal structures of native Hyd-1, E28D and E28Q. Structures of native Hyd-1, E28D and E28Q are shown in green, blue and violet respectively. The active site, R509 and residue 28 are shown. A conserved water is shown in all three structures. Red arrows indicate additional waters molecules. PDB: 5A4M (Native), 5LMM (E28Q), 5LRY (E28D).

4.3 Discussion

Glutamate-28 is highly conserved across the [NiFe]-hydrogenases, and is strictly conserved in the O_2-tolerant enzymes.[47] As a result, it has been the subject of several studies which have demonstrated that it has a role in proton transfer. The results here, however, indicate that the role of E28 is more complex.

The $K_M^{H_2}$ of E28D has a large potential dependence and increases to 5-6 times that of native Hyd-1 at 0.2 V. This was also seen for the D118 variants in Chapter 3, although for these variants the increase was even greater. Residue D118 forms part of a bottleneck to a

putative gas channel used for H_2 transport and the effect on $K_M^{H_2}$ has been postulated to be caused by changes in this bottleneck.[47] The same may be true for E28D: the carbon chain of E28 also lines this channel () and thus the rotation of D28 relative to the native residue directly affects the channel.

The H_2/D_2 kinetic isotope effect of native Hyd-1 is too low for H–H bond breaking to be the rate determining step (1.33 at 0 V) and is more likely to be attributed to a proton transfer event.[47] The reduction in the KIE for E28D variant suggests a change in the rate determining step, although as KIE > 1 it still includes a proton transfer step. Tunnelling distance is limited by mass: the heavier proton can only tunnel approximately 1 Å, whereas the maximum electron tunnelling distance is 14 Å.[135-136] To overcome this distance restriction, proton transfer pathways include closely spaced ionisable groups and water molecules. It has also been shown that carboxylate groups can use a 'swinging arm' mechanism to transport protons over greater distances (Figure 4.13).[135, 137-138] The reduced KIE in E28D could, therefore be related to a change in the mechanism of proton transfer.

Replacing E28 with aspartate or glutamine does not appear to affect the stability of Ni-B (E_{Switch}). E_{Switch} has not been measured for E28Q to date, but the reactivation of the variant following exposure to O_2 (Figure 4.10A) occurs at similar potentials to that of native Hyd-1 following aerobic or anaerobic inactivation (Figure 4.4 & Figure 4.7). O_2 flow experiments are required to fully determine the impact of the E28Q substitution on Hyd-1.

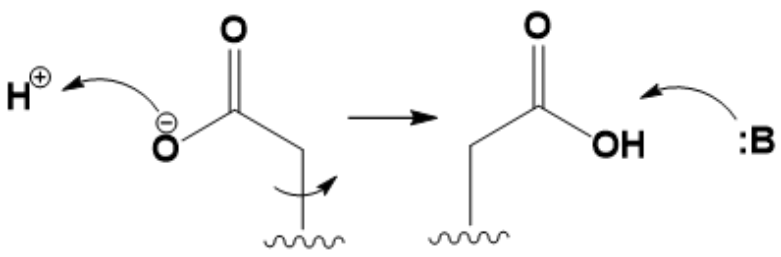


Figure 4.13: Swinging arm mechanism for proton transfer by amino acid carboxylate side chains. Once the proton is transferred to the carboxylate, the carbon chain rotates the head group so the proton can be transferred down the chain. For more information, see refs 134-136.

Despite having a similar E_{Switch} to native Hyd-1, the E28D variant has decreased O_2 tolerance: in the O_2 flow experiment, E28D did not attain steady-state H_2 oxidation activity and the current did not recover fully once the O_2 was removed. This suggests Ni-A (and other Unready states) are formed in the presence of O_2 rather than Ni-B. Additionally, E28D was unable to continue oxidising H_2 following transient exposure to O_2 and did not recover until potentials *lower* than E_{Switch} were reached (Section 4.2.1 and Figure 4.7). Although E_{Switch} was measured following the anaerobic inactivation of E28D here, for native Hyd-1 and the variant P242C (which is extremely sensitive to O_2) E_{Switch} was shown to be the same following aerobic inactivation and anaerobic inactivation. Assuming this is also true for E28D, the lack of reactivation for E28D until the electrode potential is lower than E_{Switch} suggests that species other than Ni-B are formed by E28D when O_2 attacks, even in the presence of H_2. In the structure of E28D one of the terminal cysteine residues (C576) has been oxygenated twice. Interestingly, it is the cysteine proposed to be the base in H_2 activation or the first 'step' in the proton transfer pathway to/from the active site.[5] The active site also appears to fully intact. This may be due to oxygen attack, or that E28D was not fully formed *in vivo*, but without reduced structures it is not possible to determine this. It is not possible to correlate the structure of E28D with the states being formed when O_2 is present in electrochemical experiments as H_2 is present in the latter. However, the structure demonstrates that E28D reacts with O_2 in a different manner to native Hyd-1: all recent structures of 'as isolated' (aerobically purified) native Hyd-1 and canopy variants are oxygenated at the metal-bridging cysteine-79.[47-48] This oxygenation has been attributed to the Ni-A state.[77] The O_2 data and structure support the proposal that E28 is involved in proton transport: complete O_2 reduction not only requires rapid transfer of electrons, but protons are also essential ($O_2 + 4H^+ + 4e^- \rightarrow 2H_2O$). A disrupted or slower proton transfer route would lead to the generation of Unready states and/or reactive oxygen species which react with the thiol groups at the active site.

In the electrocatalytic profile of E28D (Figure 4.4), there is a clear increase in E_{Onset} relative to native Hyd-1. Hexter *et al* proposed a model relating E_{Onset} to the potential of the electron entry/exit site $E_{entry/exit}$, and the overpotential requirement seen for O_2-tolerant [NiFe]-hydrogenases is due to the high reduction potential of the distal cluster.[66, 69] It is unlikely that E28 affects the potential of the distal cluster due to the distance between them. This is demonstrated by the work of Adamson *et al,* who measured the reduction potential of the distal cluster in native Hyd-1 and E28Q using FTacV.[62]

Abou-Hamdan *et al* explored the role of $T18^S$ (s denotes the small subunit) in the *Df* [NiFe]-hydrogenase, which is located close to the proximal cluster.[50] Originally, it was hypothesised that this residue may form part of the proton transfer pathway as the alcohol group appears to form a hydrogen bond with E28 in crystal structures. A series of $T18^S$ mutants, however, indicated that this conserved residue is not involved in proton transfer but may instead be involved in stabilising the active site so that proton and electron transfers are rapid.[50] Greene *et al* have proposed two rapidly interconverting structures for Ni-L (referred to as Ni-$I^{1/2}$ in their paper, Section 4.1.1). Both include a thiol at C576 and differ in the position of E28: for the Ni-I^2 state, E28 forms a hydrogen bond with E28, and in Ni-I^1 E28 is rotated to form a hydrogen bond with the cysteine thiol group.[84-85] In the E28D variant, the hydrogen bond with T18 is disrupted and, although a water molecule observed in the water molecule could bridge the gap, the loss of this hydrogen bond could explain the difference in the distribution of Ni-L species observed in the EPR spectra for E28D compared with native Hyd-1.[86] Following the Ar purge and removal of all E28, we would expect the active site to convert to Ni-B as H_2 oxidation is no longer catalysed. For E28D, the active site remains in the Ni-L state, although the population of Ni-L1 increases (Figure 4.11). It is not known whether Ni-L1 corresponds to a different conformation of E28 or the proton having moved elsewhere, so that it resides on E28 for example. However, E28D substitution appears to introduce a bottleneck into the

proton transfer pathway and similarly prevents the PCET required to convert the active site to Ni-C, as discussed by Greene *et al* in their SHI E17Q variant.[84-85]

The EPR results with E28Q support E28 having an impact on the active site electronics. The Fe-S clusters are fully reduced following exposure to H_2, indicating the sample is fully activated but no Ni species are observed in the 70 K spectrum. E28Q is evidently trapped in the Ni-SI state, to which H_2 binds, or the Ni-R state, which contains a bridging hydride. The work of Greene *et al* demonstrated the E28 acts as a 'gate' for the two-step Ni-C to Ni-SI transition. The first step is the tautomerisation of Ni-C to Ni-$I^{1/2}$ and PCET to form Ni-SI follows. In the SHI E17Q variant, the transition is stopped at the Ni-$I^{1/2}$ state. The EPR data for Hyd-1 E28Q suggest that the active site cannot undergo the Ni-R to Ni-C transition, which involves the oxidation of Ni(II) to Ni(III). This may be due to the higher reduction potential observed for O_2-tolerant [NiFe]-hydrogenases including Hyd-1 (Table 1.1) or may relate the complex activity seen in PFE (see below) and the increase in onset potential for H_2 oxidation seen in E28D.

Dementin *et al*'s E25Q variant in the *Df* [NiFe]-hydrogenase had negligible H_2 oxidation activity at all pHs. However, their solution assays were performed at all pH using methyl viologen which has a pH-independent potential of −430 mV.[133] This provides little driving force at low pH, and is in fact more negative than $E_{eq}(H^+/H_2)$ at pH 6, so it is unsurprising that the H_2 oxidation activity is so low. Even using methylene blue (E_{eq} ~ 70 mV) here, a low rate (< 1% of native Hyd-1) was observed despite the 350 mV of driving force (approximate) for H_2 oxidation by Hyd-1. In cyclic voltammograms, weak H_2 oxidation currents are produced by E28Q at this potential, even on a modified electrode with a large surface area. These results may alone suggest E28Q could be used in, for example, NRVS to trap the Michaelis constant. However, at higher potentials E28Q is in fact a proficient H_2 oxidiser, although it is not possible to quantitatively measure the turnover frequency for H_2 oxidation of the enzymes

at these higher potentials as native Hyd-1 would be inactivated. Cyclic voltammetry also revealed two unexpected characteristics of E28Q: (1) E28Q exhibits higher H_2 oxidation activity at high pH on an electrode; (2) as well as the typical overpotential (E_{Onset}) seen for native Hyd-1, E28Q has a second threshold potential (E_{Kick}) for H_2 oxidation. Between E_{Onset} and E_{Kick}, H_2 oxidation is seen but the increase in current (rate) with potential is slow and once E_{Kick} is met the H_2 oxidation current takes off rapidly. (1) may be explained by the higher pK_a of Gln relative to Glu. The origin of (2) is unclear but E_{Kick} has a pH dependence of −29 mV (pH unit)$^{-1}$, which corresponds to a two electron, one proton coupled event. Presumably the proton transfer is that in the Ni-L/Ni-I to Ni-SI state. The two electron transfers, however, do not correlate with this transition, unless they relate to the proximal cluster and the two electron transfers that it can mediate, and further work is required to deconvolute this.

4.4 Conclusions and future work

In their study with the equivalent E28Q variant in the soluble hydrogenase I (SHI) from *Pyrococcus furiosus* (E17Q), Greene *et al* demonstrated that E28 acts as a proton acceptor in the Ni-C to Ni-SI transition and is involved in modulating proton-coupled electron transfer (PCET). In their mechanism, Ni-C first tautomerizes to the Ni-I (Ni-L) state which includes a protonated C576. PCET follows and Ni-SI forms. The results here further demonstrate that E28 has some control over the electronics of the active site, by acting as a proton gate[84] However, the origin of E_{Kick} in the E28Q variant is not perfectly clear. Determining the redox potentials of the Fe-S clusters and the Ni species using potentiometric titrations with EPR spectroscopy[64] will be crucial for this work. Other techniques will also be useful for this work, namely protein film infrared electrochemistry (PFIRE),[80] and a technique recently developed by Ash *et al* which combines electrochemical control of single crystals and synchrotron imaging.[139]

O_2 studies and X-ray crystallographic structures with E28D indicate that this residue is crucial when O_2 attacks. This is unsurprising given the role of E28 in proton transfer. Fast delivery of protons is essential for the complete reduction of O_2 and preventing the formation of reactive oxygen species.

Initially, E28Q was produced to study the Michaelis complex with bound, intact H_2 using Nuclear Resonance Vibrational Spectroscopy. Although only low H_2 oxidation rates were observed in conventional solution assays, protein film electrochemistry indicates that (1) the rate of E28Q is too high to trap the Michaelis complex without strict potential control and (2) there are some differences in the mechanism of H_2 oxidation by E28Q (i.e. the existence of E_{Kick}) to allow a direct comparison with native Hyd-1. Instead, the variant D118V discussed in Chapter 3 may be a more suitable candidate if X-ray crystal structures indicate the enzyme is fully matured and the active site intact.

5 Bibliography

1. Tian, F.; Toon, O. B.; Pavlov, A. A.; De Sterck, H., *Science* **2005,** *308*, 1014-1017.
2. Vignais, P. M.; Billoud, B., *Chem. Rev.* **2007,** *107* (10), 4206-4272.
3. Vignais, P. M.; Billoud, B.; Meyer, J., *FEMS Microbiol. Rev.* **2001,** *25*, 455-501.
4. Bothe, H.; Schmitz, O.; Yates, M. G.; Newton, W. E., *Microbiol. Mol. Biol. Rev.* **2010,** *74* (4), 529-551.
5. Lubitz, W.; Ogata, H.; Ru, O.; Reijerse, E., *Chem. Rev.* **2014,** *114*, 4081-4148.
6. Greening, C.; Biswas, A.; Carere, C. R.; Jackson, C. J.; Taylor, M. C.; Stott, M. B.; Cook, G. M.; Morales, S. E., *The ISME Journal* **2016,** *10* (3), 761-777.
7. Dubini, A.; Pye, R. L.; Jack, R. L.; Palmer, T.; Sargent, F., *Int. J. Hydrogen Energy* **2002,** *27* (11-12), 1413-1420.
8. Sawers, G., *Antonie van Leeuwenhoek* **1994,** *66*, 57-88.
9. Self, W. T.; Hasona, A.; Shanmugam, K. T., *J. Bacteriol.* **2004,** *186* (2), 580-587.
10. Sargent, F., *The Model [NiFe]-Hydrogenases of Escherichia coli*. Elsevier Ltd.: 2016; Vol. 68, p 433-507.
11. Brøndsted, L.; Atlung, T., *J. Bacteriol.* **1994,** *176* (17), 5423-5428.
12. Atlung, T.; Knudsen, K.; Heerfordt, L.; Brøndsted, L., *J. Bacteriol.* **1997,** *179* (7), 2141-2146.
13. Volbeda, A.; Darnault, C.; Parkin, A.; Sargent, F.; Armstrong, F. A.; Fontecilla-Camps, J. C., *Structure* **2013,** *21* (1), 184-190.
14. Evans, R. M.; Parkin, A.; Roessler, M. M.; Murphy, B. J.; Adamson, H.; Lukey, M. J.; Sargent, F.; Volbeda, A.; Fontecilla-Camps, J. C.; Armstrong, F. A.; Michael, J.; Sargent, F.; Volbeda, A.; Fontecilla-Camps, J. C.; Armstrong, F. A., *J. Am. Chem. Soc.* **2013,** *135*, 2694-2707.
15. Lukey, M. J.; Roessler, M. M.; Parkin, A.; Evans, R. M.; Davies, R. A.; Lenz, O.; Friedrich, B.; Sargent, F.; Armstrong, F. A., *J. Am. Chem. Soc.* **2011,** *133* (42), 16881-16892.
16. Lukey, M. J.; Parkin, A.; Roessler, M. M.; Murphy, B. J.; Harmer, J.; Palmer, T.; Sargent, F.; Armstrong, F. A., *J. Biol. Chem.* **2010,** *285* (6), 3928-3938.
17. Pinske, C.; Jaroschinsky, M.; Linek, S.; Kelly, C. L.; Sargent, F.; Sawers, R. G., *J. Bacteriol.* **2015,** *197* (2), 296-306.
18. McDowall, J. S.; Murphy, B. J.; Haumann, M.; Palmer, T.; Armstrong, F. A.; Sargent, F., *Proc. Natl. Acad. Sci. U.S.A.* **2014,** *111* (38), 3948-3956.
19. Gupta, R. B., *Hydrogen Fuel: Production, Transport, and Storage*. CRC Press: 2008.
20. Ni, M.; Leung, M. K. H.; Sumathy, K.; Leung, D. Y. C., *Int. J. Hydrogen Energy* **2006,** *31* (10), 1401-1412.
21. Dutta, S., *Ind. Eng. Chem. Res.* **2014,** *20* (4), 1148-1156.
22. Kubas, G. J., *Chem. Rev.* **2007,** *107* (10), 4152-4205.
23. Hosseini, S. E.; Wahid, M. A., *Renew. Sust. Energ. Rev.* **2016,** *57*, 850-866.
24. Sharma, S.; Ghoshal, S. K., *Renew. Sust. Energ. Rev.* **2015,** *43*, 1151-1158.
25. Jones, A. K.; Sillery, E.; Albracht, S. P. J.; Armstrong, F. A., *Chem. Commun.* **2002,** (8), 866-867.
26. Vincent, K. A.; Cracknell, J. A.; Clark, J. R.; Ludwig, M.; Lenz, O.; Friedrich, B.; Armstrong, F. A., *Chem. Commun.* **2006,** (48), 5033-5035.

27. Reeve, H. A.; Lauterbach, L.; Lenz, O.; Vincent, K. A., *ChemCatChem* **2015,** *7* (21), 3480-3487.
28. Frielingsdorf, S.; Fritsch, J.; Schmidt, A.; Hammer, M.; Lwenstein, J.; Siebert, E.; Pelmenschikov, V.; Jaenicke, T.; Kalms, J.; Rippers, Y.; Lendzian, F.; Zebger, I.; Teutloff, C.; Kaupp, M.; Bittl, R.; Hildebrandt, P.; Friedrich, B.; Lenz, O.; Scheerer, P., *Nat. Chem. Biol.* **2014,** *10*, 378-385.
29. Fritsch, J.; Scheerer, P.; Frielingsdorf, S.; Kroschinsky, S.; Friedrich, B.; Lenz, O.; Spahn, C. M. T., *Nature* **2011,** *479*, 249-252.
30. Krishnan, S.; Armstrong, F. A., *Chem. Sci.* **2012,** *3* (4), 1015-1023.
31. Alonso-Lomillo, M. A.; Rdiger, O.; Maroto-Valiente, A.; Velez, M.; Rodríguez-Ramos, I.; Muoz, F. J.; Fernández, V. M.; Lacey, A. L. D., *Nano Lett.* **2007,** *7* (6), 1603-1608.
32. Xu, L.; Armstrong, F. A., *RSC Adv.* **2015,** (5), 3649-3656.
33. Priyadarshani, N.; Dutta, A.; Ginovska, B.; Buchko, G. W.; O'Hagan, M.; Raugei, S.; Shaw, W. J., *ACS Catal.* **2016,** *6* (9), 6037-6049.
34. Bagley, K. A.; Duin, E. C.; Roseboom, W.; Albracht, S. P. J.; Woodruffs, W. H., *Biochemistry* **1995,** *34*, 5527-5535.
35. Volbeda, A.; Garcin, E.; Piras, C.; De Lacey, A. L.; Fernandez, V. M.; Hatchikian, E. C.; Frey, M.; Fontecilla-Camps, J. C., *J. Am. Chem. Soc.* **1996,** *118* (51), 12989-12996.
36. Happe, R. P.; Roseboom, W.; Pierik, A. J.; Albracht, S. P.; Bagley, K. A., *Nature* **1997,** *385*, 126.
37. Volbeda, A.; Charon, M.-H.; Piras, C.; Hatchikian, E. C.; Frey, M.; Fontecilla-Camps, J. C., *Nature* **1995,** *373*, 580-587.
38. Parkin, A.; Goldet, G.; Cavazza, C.; Fontecilla-Camps, J. C.; Armstrong, F. A., *J. Am. Chem. Soc.* **2008,** *130* (6), 13410-13416.
39. Wombwell, C.; Caputo, C. A.; Reisner, E., *Acc. Chem. Res.* **2015,** *48* (11), 2858-2865.
40. Berggren, G.; Adamska, A.; Lambertz, C.; Simmons, T. R.; Esselborn, J.; Atta, M.; Gambarelli, S.; Mouesca, J. M.; Reijerse, E.; Lubitz, W.; Happe, T.; Artero, V.; Fontecave, M., *Nature* **2013,** *499* (7456), 66-69.
41. Higuchi, Y.; Yasuoka, N.; Kakudo, M.; Katsube, Y.; Yagi, T.; Inokuchi, H., *J. Biol. Chem.* **1987,** *262* (6), 2823-2825.
42. Volbeda, A.; Amara, P.; Darnault, C.; Mouesca, J.-M.; Parkin, A.; Roessler, M. M.; Armstrong, F. A.; Fontecilla-Camps, J. C., *Proc. Natl. Acad. Sci. U.S.A.* **2012,** *109* (14), 5305-5310.
43. Frielingsdorf, S.; Schubert, T.; Pohlmann, A.; Lenz, O.; Friedrich, B., *Biochemistry* **2011,** *50* (50), 10836-10843.
44. Chovancova, E.; Pavelka, A.; Benes, P.; Strnad, O.; Brezovsky, J.; Kozlikova, B.; Gora, A.; Sustr, V.; Klvana, M.; Medek, P.; Biedermannova, L.; Sochor, J.; Damborsky, J., *PloS one* **2012,** *8* (10), e1002708.
45. Kalms, J.; Schmidt, A.; Frielingsdorf, S.; van der Linden, P.; von Stetten, D.; Lenz, O.; Carpentier, P.; Scheerer, P., *Angew. Chem. Int. Ed.* **2016,** *55* (18), 5586-5590.
46. Montet, Y.; Amara, P.; Volbeda, A.; Vernede, X.; Hatchikian, E. C.; Field, M. J.; Frey, M.; Fontecilla-Camps, J. C., *Nat. Struct. Biol* **1997,** *4* (7), 523-526.

47. Brooke, E. J.; Evans, R. M.; Islam, S. T. A.; Roberts, G. M.; Wehlin, S. A. M.; Carr, S. B.; Phillips, S. E. V.; Armstrong, F. A., *Biochemistry* **2017,** *56* (1), 132-142.
48. Evans, R. M.; Brooke, E. J.; Wehlin, S. A. M.; Nomerotskaia, E.; Sargent, F.; Carr, S. B.; Phillips, S. E. V.; Armstrong, F. A., *Nat. Chem. Biol.* **2016,** *12*, 46-50.
49. Dementin, S.; Burlat, B.; De Lacey, A. L.; Pardo, A.; Adryanczyk-Perrier, G.; Guigliarelli, B.; Fernandez, V. M.; Rousset, M., *J. Biol. Chem.* **2004,** *279* (11), 10508-10513.
50. Abou-Hamdan, A.; Ceccaldi, P.; Lebrette, H.; Gutirrez-Sanz, O.; Richaud, P.; Cournac, L.; Guigliarelli, B.; de Lacey, A. L.; Léger, C.; Volbeda, A.; Burlat, B.; Dementin, S., *J. Biol. Chem.* **2015,** *290*, 8550-8558.
51. Szőri-Doroghzi, E.; Marti, G.; Szőri, M.; Nyilasi, A.; Rkhely, G.; Kovcs, K. L., *PLoS ONE* **2012,** *7* (4), e34666.
52. Teixeira, V. H.; Soares, C. M.; Baptista, A. M., *Proteins* **2008,** *70* (3), 1010-1022.
53. Fdez Galván, I.; Volbeda, A.; Fontecilla-Camps, J. C.; Field, M. J., *Proteins* **2008,** *73* (1), 195-203.
54. Peters, J. W.; Lanzilotta, W. N.; Lemon, B. J.; Seefeldt, L. C., *Science* **1998,** *282* (5395), 1853-1858.
55. Nicolet, Y.; Piras, C.; Legrand, P.; Hatchikian, C. E.; Fontecilla-Camps, J. C., *Structure* **1999,** *7* (1), 13-23.
56. Mulder, D. W.; Boyd, E. S.; Sarma, R.; Lange, R. K.; Endrizzi, J. A.; Broderick, J. B.; Peters, J. W., *Nature* **2010,** *465*, 248-251.
57. Cohen, J.; Kim, K.; King, P.; Seibert, M.; Schulten, K., *Structure* **2005,** *13* (9), 1321-1329.
58. Hong, G.; Pachter, R., *ACS Chem. Biol.* **2012,** *7* (7), 1268-1275.
59. Page, C. C.; Moser, C. C.; Chen, X.; Dutton, P. L., *Nature* **1999,** *402* (2), 47-52.
60. Dementin, S.; Belle, V.; Bertrand, P.; Guigliarelli, B.; Lacey, A. L. D.; Fernandez, V. M.; Rousset, M.; Le, C., *J. Am. Chem. Soc.* **2006,** *128* (16), 5209-5218.
61. Petrenko, A.; Stein, M., *Int. J. Mol. Sci.* **2017,** *18* (1), 100.
62. Adamson, H.; Robinson, M.; Wright, J. J.; Flanagan, L. A.; Walton, J.; Elton, D.; Gavaghan, D. J.; Bond, A. M.; Roessler, M. M.; Parkin, A., *J. Am. Chem. Soc.* **2017**.
63. Rousset, M.; Montet, Y.; Guigliarelli, B.; Forget, N.; Asso, M.; Bertrand, P.; Fontecilla-Camps, J. C.; Hatchikian, E. C., *Proc. Natl. Acad. Sci. U.S.A.* **1998,** *95* (20), 11625-11630.
64. Roessler, M. M.; Evans, R. M.; Davies, R. A.; Harmer, J.; Armstrong, F. A., *J. Am. Chem. Soc.* **2012,** *134*, 15581-15594.
65. Pandelia, M.-E.; Nitschke, W.; Infossi, P.; Giudici-Orticoni, M.-T.; Bill, E.; Lubitz, W., *Proc. Natl. Acad. Sci. U.S.A.* **2011,** *108* (15), 6097-6102.
66. Hexter, S. V.; Grey, F.; Happe, T.; Climent, V.; Armstrong, F. A., *Proc. Natl. Acad. Sci. U.S.A.* **2012,** *109* (29), 11516-11521.
67. Goris, T.; Wait, A. F.; Saggu, M.; Fritsch, J.; Heidary, N.; Stein, M.; Zebger, I.; Lendzian, F.; Armstrong, F. A.; Friedrich, B.; Lenz, O., *Nat. Chem. Biol.* **2011,** *7*, 310-318.

68. Shomura, Y.; Yoon, K.-S.; Nishihara, H.; Higuchi, Y., *Nature* **2011,** *479* (7372), 253-256.
69. Murphy, B. J.; Sargent, F.; Armstrong, F. A., *Energy Environ. Sci.* **2014,** *7* (4), 1426-1433.
70. Léger, C.; Jones, A. K.; Roseboom, W.; Albracht, S. P. J.; Armstrong, F. A., *Biochemistry* **2002,** *41* (52), 15736-15746.
71. Goldet, G.; Wait, A. F.; Cracknell, J. A.; Vincent, K. A.; Ludwig, M.; Lenz, O.; Friedrich, B.; Armstrong, F. A., *J. Am. Chem. Soc.* **2008,** *130* (33), 11106-11113.
72. Lacey, A. L. D.; Fernández, V. M.; Rousset, M.; Cammack, R., *Chem. Rev.* **2007,** *107* (10), 4304-4330.
73. Schfer, C.; Bommer, M.; Hennig, S. E.; Jeoung, J.-h.; Dobbek, H.; Lenz, O., *Structure* **2016,** *24* (2), 285-292.
74. Cracknell, J. A.; Wait, A. F.; Lenz, O.; Friedrich, B.; Armstrong, F. A., *Proc. Natl. Acad. Sci. U.S.A.* **2009,** *106* (49), 20681-20686.
75. Lamle, S. E.; Albracht, S. P. J.; Armstrong, F. A., *J. Am. Chem. Soc.* **2004,** *126* (45), 14899-14909.
76. Fontecilla-Camps, J. C.; Volbeda, A.; Cavazza, C.; Nicolet, Y., *Chem. Rev.* **2007,** *107* (10), 4273-4303.
77. Volbeda, A.; Martin, L.; Barbier, E.; Gutiérrez-Sanz, O.; De Lacey, A. L.; Liebgott, P.-P.; Dementin, S.; Rousset, M.; Fontecilla-Camps, J. C., *J. Biol. Inorg. Chem.* **2015,** *20* (1), 11-22.
78. Carepo, M.; Tierney, D. L.; Brondino, C. D.; Yang, T. C.; Pamplona, A.; Telser, J.; Moura, I.; Moura, J. J. G.; Hoffman, B. M., *J. Am. Chem. Soc.* **2002,** *124* (2), 281-286.
79. Wulff, P.; Thomas, C.; Sargent, F.; Armstrong, F. A., *J. Biol. Inorg. Chem.* **2016,** *21* (1), 121-134.
80. Ash, P. A.; Hidalgo, R.; Vincent, K. A., *ACS Catal.* **2017,** *7* (4), 2471-2485.
81. Ogata, H.; Nishikawa, K.; Lubitz, W., *Nature* **2015,** *520*, 571-575.
82. Carr, S. B.; Phillips, S. E. V., 2016.
83. Kampa, M.; Pandelia, M.-E.; Lubitz, W.; van Gastel, M.; Neese, F., *J. Am. Chem. Soc.* **2013,** *135* (10), 3915-3925.
84. Greene, B. L.; Vansuch, G. E.; Wu, C. H.; Adams, M. W. W.; Dyer, R. B., *J. Am. Chem. Soc.* **2016,** *138* (39), 13013-13021.
85. Greene, B. L.; Wu, C. H.; Vansuch, G. E.; Adams, M. W. W.; Dyer, R. B., *Biochemistry* **2016,** *55* (12), 1813-1825.
86. Murphy, B. J.; Hidalgo, R.; Roessler, M. M.; Evans, R. M.; Ash, P. A.; Myers, W. K.; Vincent, K. A.; Armstrong, F. A., *J. Am. Chem. Soc.* **2015,** *137* (26), 8484-8489.
87. Tai, H.; Nishikawa, K.; Suzuki, M.; Higuchi, Y.; Hirota, S., *Angew. Chem. Int. Ed.* **2014,** *53* (50), 13817-13820.
88. Greene, B. L.; Wu, C.-H.; McTernan, P. M.; Adams, M. W. W.; Dyer, R. B., *J. Am. Chem. Soc.* **2015,** *137* (13), 4558-4566.
89. Kubas, G. J.; Ryan, R. R.; Swanson, B. I.; Vergamini, P. J.; Wasserman, H. J., *J. Am. Chem. Soc.* **1984,** *106* (2), 451-452.
90. Kubas, G. J., *J. Organomet. Chem.* **2014,** *751*, 33-49.
91. Stephan, D. W., *J. Am. Chem. Soc.* **2015,** *137* (32), 10018-10032.
92. Stephan, D. W.; Erker, G., *Angew. Chem. Int. Ed.* **2010,** *49* (1), 46-76.

93. Welch, G. C.; Juan, R. R. S.; Masuda, J. D.; Stephan, D. W., *Science* **2006,** *314*, 1124-1126.
94. Hamza, A.; Stirling, A.; Rokob, T. A.; Pápai, I., *Int. J. Quantum Chem* **2009,** *109* (11), 2416-2425.
95. Megarity, C. F.; Esselborn, J.; Hexter, S. V.; Wittkamp, F.; Apfel, U. P.; Happe, T.; Armstrong, F. A., *J. Am. Chem. Soc.* **2016,** *138* (46), 15227-15233.
96. Barton, B. E.; Rauchfuss, T. B., *J. Am. Chem. Soc.* **2010,** *132* (42), 14877-14885.
97. Ogo, S.; Ryota, K.; Uehara, K.; Kure, B.; Nishimura, T.; Menon, S. C.; Harada, R.; Fukuzumi, S.; Higuchi, Y.; Ohhara, T.; Tamada, T.; Kuroki, R., *Science* **2007,** *316* (5824), 585-588.
98. Ogo, S.; Ichikawa, K.; Kishima, T.; Matsumoto, T.; Nakai, H.; Kusaka, K.; Ohhara, T., *Science* **2013,** *339* (6120), 682-684.
99. Helm, M. L.; Stewart, M. P.; Bullock, R. M.; Dubois, M. R.; Dubois, D. L., *Science* **2011,** *333* (6044), 863-866.
100. Dutta, A.; DuBois, D. L.; Roberts, J. A. S.; Shaw, W. J., *Proc. Natl. Acad. Sci. U.S.A.* **2014,** *111* (46), 16286-16291.
101. Boralugodage, N. P.; Arachchige, R. J.; Dutta, A.; Buchko, G. W.; Shaw, W. J., *Catal. Sci. Technol.* **2017,** *7* (5), 1108-1121.
102. DeLacey, A. L.; Fernandez, V. M.; Rousset, M.; Cavazza, C.; Hatchikian, E. C., *J. Biol. Inorg. Chem.* **2003,** *8* (1), 129-134.
103. Domagała, M.; Grabowski, S. J., *Chem. Phys.* **2009,** *363* (1-3), 42-48.
104. Voet, D.; Voet, J. G., *Biochemistry*. Fourth ed.; John Wiley & Sons, Inc: 2011.
105. Guillén Schlippe, Y. V.; Hedstrom, L., *Arch. Biochem. Biophys.* **2005,** *433* (1), 266-278.
106. Hong, J. H.; Dilbeck, P.; Debus, R. J.; Burnap, R. L., *Biochemistry* **2007,** *46* (43), 11987-11997.
107. Morris, R. H., *J. Am. Chem. Soc.* **2014,** *136* (5), 1948-1959.
108. Schilter, D.; Camara, J. M.; Huynh, M. T.; Hammes-Schiffer, S.; Rauchfuss, T. B., *Chem. Rev.* **2016,** *116* (15), 8693-8749.
109. Gibson, D. G.; Smith, H. O.; Iii, C. A. H.; Venter, J. C.; Merryman, C., *Nature Methods* **2010,** *7* (11), 901-903.
110. Hamilton, C. M.; Aldea, M.; Washburn, B. K.; Babitzke, P.; Kushner, S. R., *J. Bacteriol.* **1995,** *171* (9), 4617-4622.
111. Bradford, M. M., *Anal. Biochem.* **1976,** *72* (1-2), 248-254.
112. Arp, D. J.; Burris, R. H., *Biochemistry* **1981,** *20* (8), 2234-2240.
113. Evans, R. M.; Armstrong, F. A., *Electrochemistry of metalloproteins: protein film electrochemistry for the study of E. coli NiFe -hydrogenase-1*. Humana Press: Totowa, NJ. , 2014; Vol. 1122.
114. Bard, A. J.; Faulkner, L. R., *Electrochemical Methods: Fundamentals and Applications*. Second ed.; John Wiley & Sons. Inc: USA, 2001.
115. Fisher, A. C., *Electrode Dynamics*. Oxford University Press: New York, USA, 2009.
116. Vincent, K. A.; Parkin, A.; Armstrong, F. A., *Chem. Rev.* **2007,** *107* (10), 4366-4413.
117. Hagen, W. R., *Biomolecular EPR Spectroscopy*. CRC Press: Boca Raton, FL, USA, 2009.

118. Cukierman, S., *Biochim. Biophys. Acta, Bioenerg.* **2006,** *1757* (8), 876-885.
119. Wraight, C. A., *Biochim. Biophys. Acta, Bioenerg.* **2006,** *1757* (8), 886-912.
120. Brzezinski, P.; Ädelroth, P., *Curr. Opin. Struct. Biol.* **2006,** *16* (4), 465-472.
121. Liang, Z.-X.; Klinman, J. P., *Curr. Opin. Struct. Biol.* **2004,** *14* (6), 648-655.
122. Salna, B.; Benabbas, A.; Sage, J. T.; van Thor, J.; Champion, P. M., *Nat. Chem.* **2016,** *8*, 874-880.
123. Sumner, I.; Voth, G. A., *J. Phys. Chem. B* **2012,** *116* (9), 2917-2926.
124. Vincent, K. A.; Parkin, A.; Lenz, O.; Albracht, S. P. J.; Fontecilla-Camps, J. C.; Cammack, R.; Friedrich, B.; Armstrong, F. A., *J. Am. Chem. Soc.* **2005,** *127* (51), 18179-18189.
125. Liebgott, P.-P.; de Lacey, A. L.; Burlat, B.; Cournac, L.; Richaud, P.; Brugna, M.; Fernandez, V. M.; Guigliarelli, B.; Rousset, M.; Léger, C.; Dementin, S., *J. Am. Chem. Soc.* **2011,** *133* (4), 986-997.
126. Dementin, S.; Leroux, F.; Cournac, L.; de Lacey, A. L.; Volbeda, A.; Léger, C.; Burlat, B.; Martinez, N.; Champ, S.; Martin, L.; Sanganas, O.; Haumann, M.; Fernandez, V. M.; Guigliarelli, B.; Fontecilla-Camps, J. C.; Rousset, M., *J. Am. Chem. Soc.* **2009,** *131* (29), 10156--10164.
127. Kochem, A.; Bill, E.; Neese, F.; van Gastel, M., *Chem. Commun.* **2015,** (51), 2099-2102.
128. Ogata, H.; Krämer, T.; Wang, H.; Schilter, D.; Pelmenschikov, V.; van Gastel, M.; Neese, F.; Rauchfuss, T. B.; Gee, L. B.; Scott, A. D.; Yoda, Y.; Tanaka, Y.; Lubitz, W.; Cramer, S. P., *Nat. Commun.* **2015,** *6*, 7890.
129. Krämer, T.; Kampa, M.; Lubitz, W.; van Gastel, M.; Neese, F., *ChemBioChem* **2013,** *14* (14), 1898-1905.
130. Dong, G.; Phung, Q. M.; Hallaert, S. D.; Pierloot, K.; Ryde, U., *Phys. Chem. Chem. Phys.* **2017,** *19* (16), 10590-10601.
131. Siegbahn, P. E.; Tye, J. W.; Hall, M. B., *Chem. Rev.* **2007,** *107* (10), 4414-4435.
132. Lamle, S. E.; Vincent, K. A.; Halliwell, L. M.; Albracht, S. P. J.; Armstrong, F. A., *Dalton Trans.* **2003,** *0*, 4152-4157.
133. Cammack, R.; Fernandez, V. M.; Hatchikian, E. C., *Methods Enzymol.* **1994,** *243* (1989), 43-68.
134. Roessler, M. M. EPR Investigations of Iron-Sulfur Cluster Relays in Enzymes. St. John's College, University of Oxford, 2011.
135. Chen, K.; Hirst, J.; Camba, R.; Bonagura, C. A.; Stout, C. D.; Burgess, B. K.; Armstrong, F. A., *Nature* **2000,** *405* (June), 814-817.
136. Glover, S. D.; Parada, G. A.; Markle, T. F.; Ott, S.; Hammarström, L., *J. Am. Chem. Soc.* **2017,** *139* (5), 2090-2101.
137. Hirst, J., *Proc. Natl. Acad. Sci. U.S.A.* **2003,** *100* (3), 773-775.
138. Pankhurst, K. L.; Mowat, C. G.; Rothery, E. L.; Hudson, J. M.; Jones, A. K.; Miles, C. S.; Walkinshaw, M. D.; Armstrong, F. A.; Reid, G. A.; Chapman, S. K., *J. Biol. Chem.* **2006,** *281* (29), 20589-20597.
139. Ash, P. A.; Carr, S. B.; Reeve, H. A.; Skorupskaite, A.; Rowbotham, J. S.; Shutt, R.; Frogley, M. D.; Evans, R. M.; Cinque, G.; Armstrong, F. A.; Vincent, K. A., *Chem. Commun.* **2017,** (43), 5858-5861.

6 Appendices

6.1 Nernst Equation

For a redox reaction, a species with a standard reduction potential E^o will be reduced by a species with a lower E^o. Consider a redox reaction between two species A and B

$$A_{\mathrm{ox}} + B_{\mathrm{red}} \rightleftharpoons A_{\mathrm{red}} + B_{\mathrm{ox}} \tag{6.1}$$

which can be split into the constituent half reactions, including a number (n) of electrons (e^-):

$$A_{ox} + ne^- \rightleftharpoons A_{\mathrm{red}} \tag{6.2}$$

$$B_{\mathrm{red}} \rightleftharpoons B_{\mathrm{ox}} + ne^- \tag{6.3}$$

The reaction quotient Q for the reaction is given by:

$$Q = \frac{[A_{\mathrm{red}}][B_{\mathrm{ox}}]}{[B_{\mathrm{red}}][A_{\mathrm{ox}}]} \tag{6.4}$$

At equilibrium conditions, Q is equal to the equilibrium constant *K*. Under standard conditions, the standard Gibbs free energy of the reaction, ΔG^o, can be related to both and Q and the standard cell potential E^o_{cell}.

$$\Delta G^o = \mathrm{RT}\ln Q \tag{6.5}$$

$$\Delta G^o = -nFE^o_{\mathrm{cell}} \tag{6.6}$$

where R is the gas constant (8.314 J K^{-1} mol^{-1}), T is the temperature in K, n is the number of electrons, F is the Faraday constant (96 485 C mol^{-1}) and $E^o_{\mathrm{cell}} = E^o_{\mathrm{A}} - E^o_B$ for a reaction in which A is reduced by B Under non-standard conditions, the Gibbs free energy can be found using:

$$\Delta G = \Delta G^o + \mathrm{RT}\ln Q \tag{6.7}$$

We can substitute (6.6) into (6.7):

$$-nFE_{\mathrm{cell}} = -nFE^o_{\mathrm{cell}} + \mathrm{RT}\ln Q \tag{6.8}$$

where E_{cell} is the cell potential under non standard conditions. This can be rearranged to give the 'Nernst equation' describing the change in cell potential with the reaction:

$$E_{\mathrm{cell}} = E^o_{\mathrm{cell}} - \frac{RT}{nF}\ln Q \tag{6.9}$$

We can also arrive at the Nernst equation for reactions (6.2) and (6.3):

$$E_A = E_A^o - \frac{RT}{nF}\frac{[A_{\text{red}}]}{[A_{\text{ox}}]} \tag{6.10}$$

$$E_B = E_B^o + \frac{RT}{nF}\frac{[B_{\text{ox}}]}{[B_{\text{red}}]} \tag{6.11}$$

This can be applied to a redox event involving protons H^+ (6.12) to determine the pH-dependence of the reaction:

$$A_{ox} + ne^- + m\text{H}^+ \rightleftharpoons A_{\text{red}}\text{H}_m \tag{6.12}$$

$$E_{eq} = E^o + \frac{RT}{nF}\frac{[A_{\text{ox}}][\text{H}^+]^m}{[A_{\text{red}}\text{H}_m]} \tag{6.13}$$

We can convert this to log, using *T* as 298 K:

$$E_{eq} = E^o + 2.303\frac{RT}{nF}\log\frac{[A_{\text{ox}}][\text{H}^+]^m}{[A_{\text{red}}\text{H}_m]} \tag{6.14}$$

$$E_{eq} = E^o + 2.303\frac{RT}{nF}\log\frac{[A_{\text{ox}}]}{[A_{\text{red}}\text{H}_m]} + 2.303\frac{RT}{nF}\log[\text{H}^+]^m \tag{6.15}$$

$$E_{eq} = E^o + 2.303\frac{RT}{nF}\log\frac{[A_{\text{ox}}]}{[A_{\text{red}}\text{H}_m]} + 2.303\frac{RTm}{nF}(-\text{pH}) \tag{6.16}$$

$$E_{eq} = E^o + \frac{0.059}{n}\log\frac{[A_{\text{ox}}]}{[A_{\text{red}}\text{H}_m]}\boxed{-\frac{m}{n}0.059\ \text{pH}} \tag{6.17}$$

So for a $2e^-, 2\text{H}^+$process, E increases by 59 mV per decrease in pH unit and for a $2e^-, 1\text{H}^+$ there is a an increase in E by 29 mV per decrease in pH unit, and so on.

The Nernst equation for the equilibrium potential for the H^+/H_2 ($E_{eq}(H^+/H_2)$ couple is as follows:

$$2\text{H}^+ + 2e^- \rightleftharpoons \text{H}_2 \tag{6.18}$$

$$E_{eq}(\text{H}^+/\text{H}_2) = E^o + \frac{RT}{nF}\frac{[\text{H}^+]^2}{p(\text{H}_2)} \tag{6.19}$$

6.2 pH dependence of native Hyd-1 and canopy variants

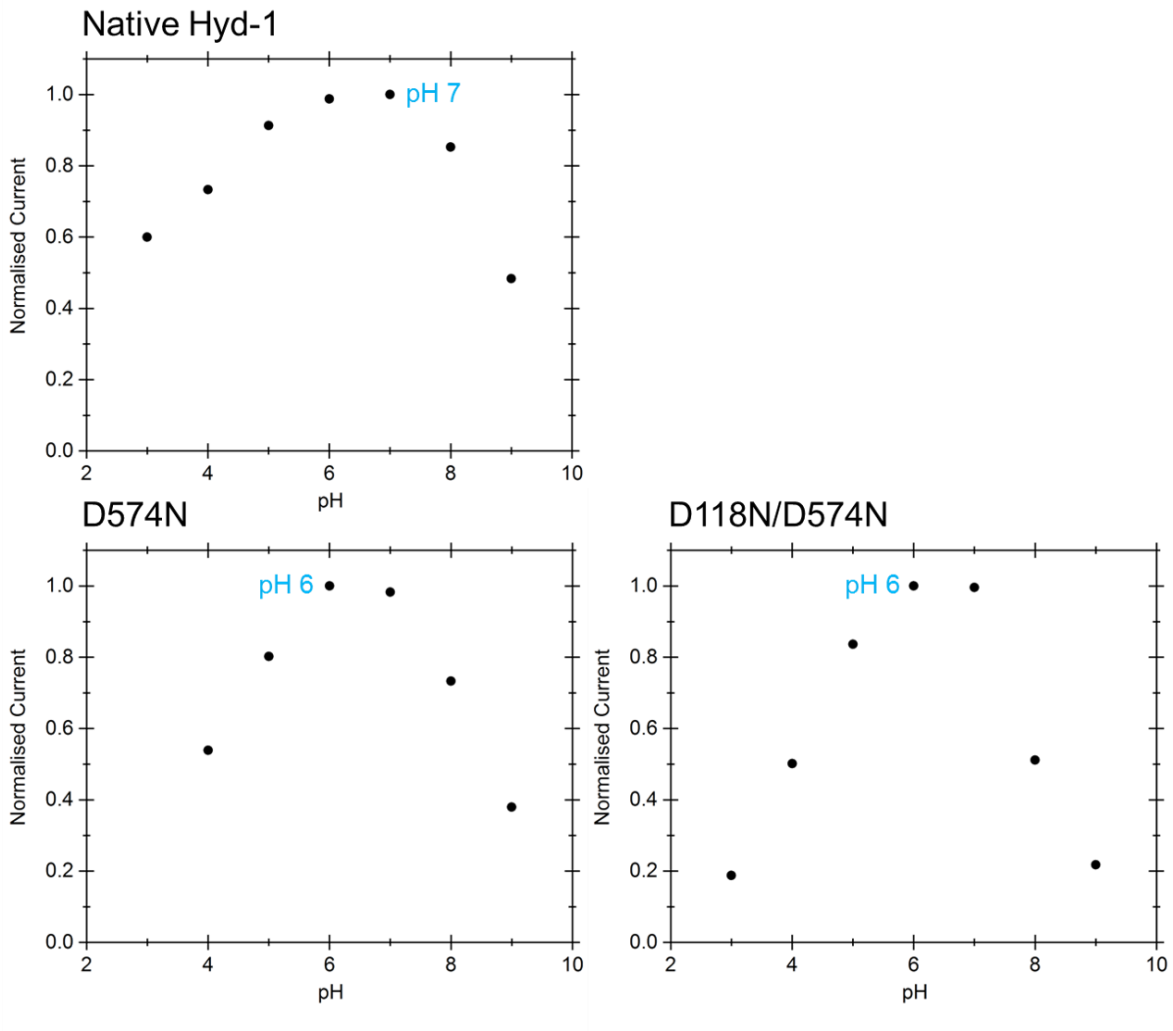


Figure 6.1: pH dependence of native Hyd-1, D574N and D118N/D574N. The pH dependence was measured using chronoamperometry at a single potential. For native Hyd-1, this was at 0 V but the low E_{Switch} for D574N and D118N/D574N meant that a lower potential was required (–0.1 V). For D574N, significant film loss was seen at pH 3 so the current was not recorded. The pH optimum of native Hyd-1 was pH 6, and pH 7 for both D574N and D118N/D574N.

6.3 Michaelis-Menten Kinetics and Hanes-Woolf Analysis

Michaelis-Menten kinetics is a model often used to describe enzyme kinetics based on a two-step reaction mechanism, described by the rate constants k_1, k_{-1} and k_{cat}. The latter is often referred to as k_2.

$$\mathrm{E} + \mathrm{S} \underset{k_{-1}}{\overset{k_1}{\rightleftharpoons}} \mathrm{ES} \overset{k_{\mathrm{cat}}}{\rightarrow} \mathrm{E} + \mathrm{P} \tag{6.20}$$

E refers to the free enzyme, S is substrate, ES is the enzyme-substrate complex and P is the product. The overall rate equation for the formation of the ES is:

$$\frac{d[\mathrm{ES}]}{dt} = k_1[\mathrm{E}][\mathrm{S}] - (k_{-1} + k_{cat})[\mathrm{ES}] \tag{6.21}$$

Using the steady-state approximation, that is that the concentration of ES is constant and thus the formation of ES is the same as the depletion of ES, we get:

$$\frac{d[\mathrm{ES}]}{dt} = 0 \tag{6.22}$$

and

$$k_1[\mathrm{E}][\mathrm{S}] = (k_{-1} + k_{cat})[\mathrm{ES}] \tag{6.23}$$

As we cannot measure $[\mathrm{ES}]$ or $[\mathrm{E}]$, we can relate these to the total enzyme concentration $[E_0]$. The total enzyme concentration is equivalent to the initial enzyme concentration, which is known.

$$[\mathrm{E}_0] = [\mathrm{E}] + [\mathrm{ES}] \tag{6.24}$$

Rearranging (6.24) for $[\mathrm{E}]$ and substituting into (6.23):

$$k_1([\mathrm{E}_0] - [\mathrm{ES}])[\mathrm{S}] = (k_{-1} + k_{cat})[\mathrm{ES}] \tag{6.25}$$

Again, we can rearrange (6.25) for $[\mathrm{ES}]$:

$$k_1([\mathrm{E}_0][S] = [\mathrm{ES}](k_{-1} + k_{cat} + k_1[\mathrm{S}]) \tag{6.26}$$

$$\frac{k_1([\mathrm{E}_0][\mathrm{S}]}{k_{-1} + k_{cat} + [\mathrm{S}]} = [\mathrm{ES}] \tag{6.27}$$

The Michaelis constant K_{M} is defined as:

$$K_{\mathrm{M}} = \frac{k_{-1} + k_{cat}}{k_1} \tag{6.28}$$

therefore

$$\frac{[\mathrm{E_0}][\mathrm{S}]}{K_{\mathrm{M}} + [\mathrm{S}]} = [\mathrm{ES}] \tag{6.29}$$

The velocity of the reaction ν (6.20), that is the rate of product P formation the reaction, at t_s can be found using:

$$\nu = \left(\frac{d[P]}{dt}\right)_t = k_{cat}[\mathrm{ES}] \tag{6.30}$$

Thus, the initial velocity ν_0 is defined as:

$$\nu_0 = \frac{k_{cat}[\mathrm{E_0}][\mathrm{S}]}{K_{\mathrm{M}} + [\mathrm{S}]} \tag{6.31}$$

The maximum velocity $V_{\max}$ occurs when the enzyme is saturated with substrate, i.e. when $[\mathrm{ES}] = [\mathrm{E_0}]$:

$$V_{\max} = k_{cat}[\mathrm{E_0}] \tag{6.32}$$

The Michaelis-Menten equation is found from substituting (6.32) into (6.31):

$$\nu_0 = \frac{V_{\max}[\mathrm{S}]}{K_{\mathrm{M}} + [\mathrm{S}]} \tag{6.33}$$

As well as assuming steady-state conditions, this model also assumes that the substrate concentration $[\mathrm{S}]$ is much greater than the enzyme concentration $[\mathrm{E_0}]$ such that all enzyme is converted to the enzyme substrate complex ES

$$[\mathrm{S}] \gg [\mathrm{E_0}] \tag{6.34}$$

The Michaelis constant is often used as an affinity constant, such that a small K_{M} means that an enzyme has a high affinity for its substrate. In fact, K_{M} is closer to a dissociation

constant K_{D} when we assume that the second step (6.20) of the reaction, that is the conversion of $[\mathrm{ES}]$ to $\mathrm{E} + \mathrm{P}$, is much slower than the first step:

$$k_{-1} \gg k_{cat} \tag{6.35}$$

so,

$$K_{\mathrm{D}} = \frac{[\mathrm{E}][\mathrm{S}]}{[\mathrm{ES}]} = \frac{k_{-1}}{k_1} \tag{6.36}$$

and we can redefine K_{M} as

$$K_{\mathrm{M}} = \frac{k_{-1}}{k_1} + \frac{k_{cat}}{k_1} \tag{6.37}$$

$$K_{\mathrm{M}} = K_{\mathrm{D}} + \frac{k_{cat}}{k_1} \tag{6.38}$$

So, when (6.35) is true:

$$K_{\mathrm{M}} \approx K_{\mathrm{D}} \tag{6.39}$$

The Hanes-Woolf representation was used to determine K_{M} here to ensure consistency with previous studies, as this has been used for Hyd-1 and variants in the past. A Hanes-Woolf plot uses a rearrangement of the Michaelis-Menten equation:

$$\frac{[\mathrm{S}]}{\nu} = \frac{[\mathrm{S}]}{V_{\max}} + \frac{K_{\mathrm{M}}}{V_{\max}} \tag{6.40}$$

Using the current i under different [H_2] as the velocity ν, we get the form:

$$\frac{[\mathrm{H_2}]}{i} = \frac{[\mathrm{H_2}]}{i_{\max}} + \frac{K_{\mathrm{M}}}{i_{\max}} \tag{6.41}$$

Thus, plotting ${}^{[\mathrm{H_2}]}/_{i}$ versus $[\mathrm{H_2}]$ gives a slope of ${}^{1}/_{V_{\max}}$ and an intercept of ${}^{K_{\mathrm{M}}}/_{V_{\max}}$. For native Hyd-1 and variants discusses in this thesis, this was performed at several electrode potentials. A Hanes-Woolf analysis requires the data be linear and, in some cases, particularly when the K_{M} was found to be high, the data at low [H_2] was omitted. An example of PFE data for the Hyd-1 variant D574N is shown in Figure 6.2 and the subsequent Hanes-Woolf plot is shown in Figure 6.3. This data gave a $K_{\mathrm{M}}^{\mathrm{H_2}}$ of 15.4 μM at 0 V.

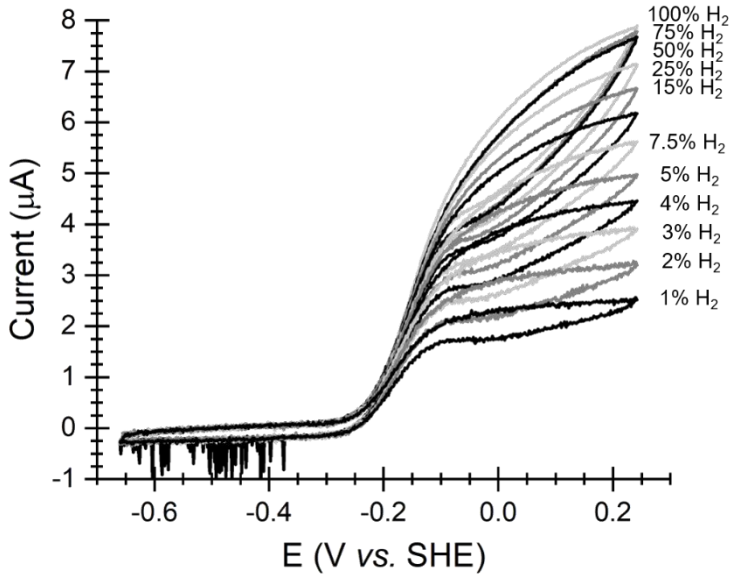


Figure 6.2: Cyclic voltammograms of the Hyd-1 variant D574N in different H_2/Ar mixes. These were used to generate the Hanes-Woolf plot shown in Figure 6.3. Conditions: −0.65 V to +0.24 V, 5 mV s^{-1}, pH 6, 30 °C, total gas flow = 1000 scc min^{-1}, ω = 3000 rpm

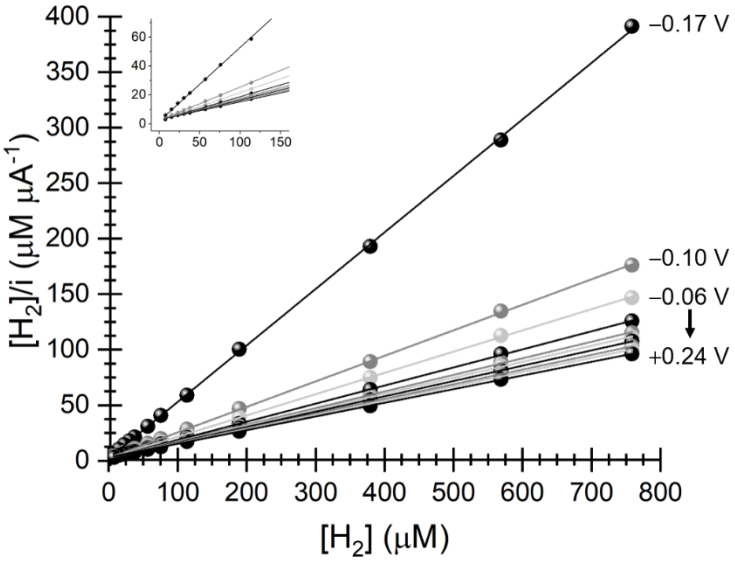


Figure 6.3: Example of a Hanes-Woolf analysis for the Hyd-1 canopy variant D574N. The data from Figure 6.2 was used in a $^{[\mathrm{H_2}]}/_{i}$ vs. $[\mathrm{H_2}]$ plot at different potentials. A linear regression was used to determine $V_{\max}$ and K_{M}. An inset is included to show the data at low $[\mathrm{H_2}]$.

6.4 Eyring equation and use

The Eyring equation is derived from transition state theory which describes reaction kinetics. Two reacting molecules C and D are in equilibrium with an 'activated complex' $\mathrm{M}^{\ddagger}$

$$\mathrm{C} + \mathrm{D} \rightleftharpoons \mathrm{M}^{\ddagger} \tag{6.42}$$

If the activated complex passes through the 'transition state' $\mathrm{TS}^{\ddagger}$, the reaction can proceed to the products. Although the transition state is an activated complex, it is not the only activated complex on the reaction energy profile.

$$\mathrm{C} + \mathrm{D} \rightleftharpoons \mathrm{TS}^{\ddagger} \rightarrow \mathrm{P} \tag{6.43}$$

The equilibrium constant for the first step is:

$$K^{\ddagger} = \frac{[\mathrm{TS}^{\ddagger}]}{[\mathrm{C}][\mathrm{D}]} \tag{6.44}$$

The reaction rate is equivalent to the number of activated complexes that reach the energy barrier, i.e. the transition state $\mathrm{TS}^{\ddagger}$, and then decompose to products. The frequency at which this happens is given by $\nu^{\ddagger}$. Thus, the rate can be written in two ways:

$$rate = \nu^{\ddagger}\left[\mathrm{TS}^{\ddagger}\right] = \nu^{\ddagger} K^{\ddagger}[\mathrm{C}][\mathrm{D}] \tag{6.45}$$

and

$$rate = k[\mathrm{C}][\mathrm{D}] \tag{6.46}$$

Thus,

$$k = \nu^{\ddagger} K^{\ddagger} \tag{6.47}$$

The frequency term comes from statistical mechanisms and includes the Boltzmann constant, k_B and Planck's constant, h:

$$\nu^{\ddagger} = \frac{k_B T}{h} \tag{6.48}$$

We can substitute (6.48) into (6.47):

$$k = \frac{k_B T}{h} K^{\ddagger} \tag{6.49}$$

The Gibbs free energy change can be determined is found using one of two expressions, which are equivalent:

$$\Delta G^{\ddagger} = \Delta H^{\ddagger} - T\Delta S^{\ddagger} = -RT\ln K^{\ddagger} \tag{6.50}$$

By substituting (6.49) into (6.50) and rearranging, we reach:

$$\ln\frac{kh}{k_B T} = -\frac{\Delta H^{\ddagger}}{RT} + \frac{\Delta S^{\ddagger}}{R} \tag{6.51}$$

Further rearrangement results in the linear form of the Eyring equation (6.53):

$$\ln\frac{k}{T} - \ln\frac{k_B}{h} = -\frac{\Delta H^{\ddagger}}{RT} + \frac{\Delta S^{\ddagger}}{R} \tag{6.52}$$

$$\ln\frac{k}{T} = -\frac{\Delta H^{\ddagger}}{RT} + \frac{\Delta S^{\ddagger}}{R} + \ln\frac{k_B}{h} \tag{6.53}$$

This form can be used to determine the enthalpy change $\Delta H^{\ddagger}$ and $\Delta S^{\ddagger}$ by using the current i in place of the rate constant k and plotting $\ln {}^{i}/_{T}$ versus ${}^{1}/_{T}$. The gradient gives $\Delta H^{\ddagger}$ and the intercept is ${}^{\Delta S^{\ddagger}}/_{R} + \ln {}^{k_B}/_{h}$. An example of temperature-dependent cyclic voltammograms for Hyd-1 variant D574N is shown in Figure 6.4 and the subsequent Eyring plot is shown in Figure 6.5.

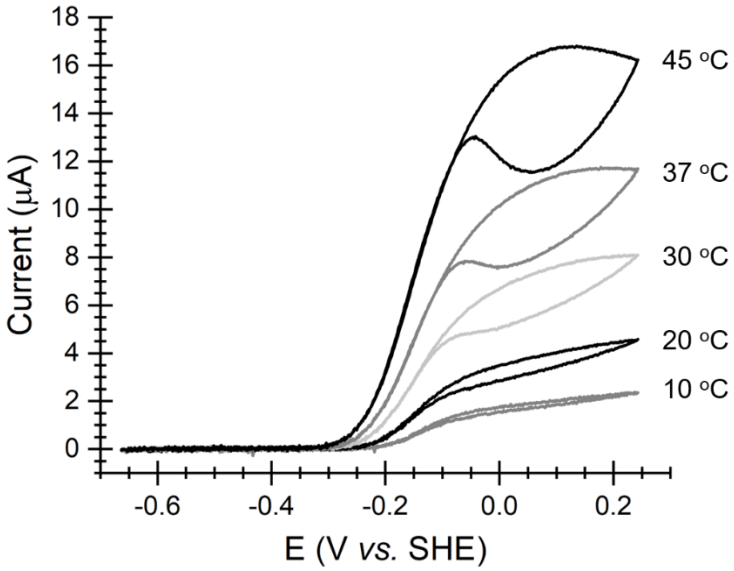


Figure 6.4: Cyclic voltammograms of Hyd-1 variant D574N at different temperatures. Data was used to produce the Eyring plot shown in Figure 6.5. Conditions: –0.65 V to +0.24 V, 5 mV s^{-1}, pH 6, 10 – 45 °C, 100% H_2, total gas flow = 500 scc min^{-1}, ω = 3000 rpm

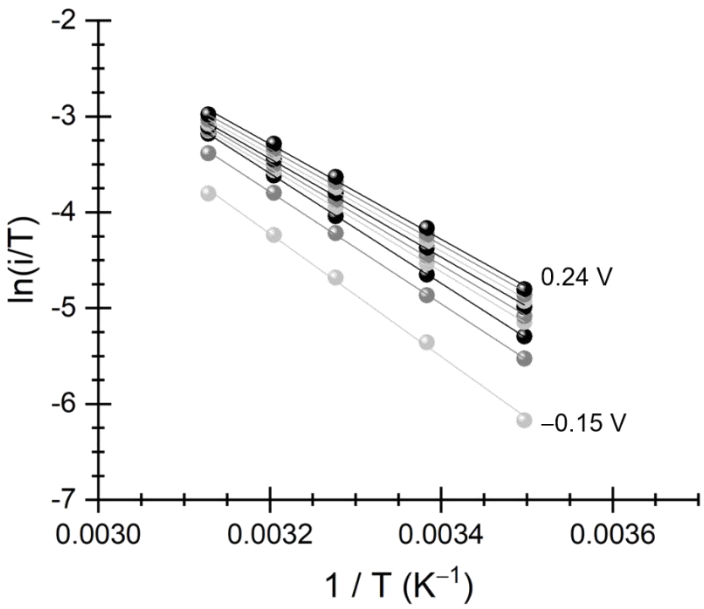


Figure 6.5: Example of an Eyring plot for the Hyd-1 canopy variant D574N. The data from Figure 6.4 was used to produce a plot of $\ln(i/T)$ versus $1/T$ at different potentials. A linear regression was used to determine $\Delta H^{\ddagger}$ and $\Delta S^{\ddagger}/R + \ln\left(k_B/h\right)$.

6.5 Correcting for a current offset

During the H_2 production experiments, a current offset way observed for the R509K variant. This resulted in the zero-current occurring at a lower potential than the thermodynamic potential predicted by the Nernst equation (Appendix 6.1). As a result, the current offset was corrected as follows:

- The current offset was measured to be 0.8 μA at the thermodynamic potential for the H^+/H_2 couple ($E_{eq}(H^+/H_2)$, -0.123 V at pH 3 and 1% H_2), indicated on Figure 6.6A
- At each potential, 0.8 μA was taken from the current
- The resulting plot is shown in Figure 6.6B. The zero-current potential matches the $E_{eq}(H^+/H_2)$.

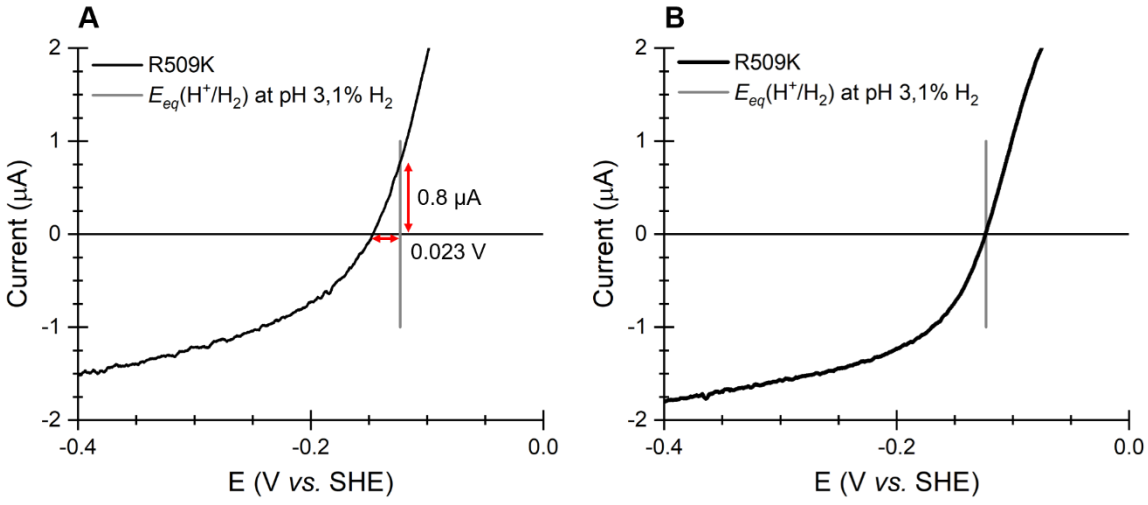


Figure 6.6: Current offset adjustment for R509K film on a modified electrode. A – R509K at pH 3 and 1% H_2 on a modified electrode. The forwards and reverse scans of a cyclic voltammogram were averaged so the zero-current potential could be determined. For this data, a 0.8 μA current offset resulted in the zero-current potential being 0.023 V below the Nernstian potential for the H^+/H_2 couple ($E_{eq}(H^+/H_2)$), which is indicated by the grey line. **B** – 0.8 μA was subtracted from the current at each potential. Following this correction, the zero-current potential for the R509K film matched exactly $E_{eq}(H^+/H_2)$ as expected

6.6 CO dependence of E28D

The sensitivity of E28D to CO was determined using the method described in Section 3.6.4. The current response of E28D was recorded at -0.06 V under 20% H_2. The current was monitored for approximately 650 s so ensure it was stable before CO was introduced. CO was then introduced and subsequently stepped to 20% CO, whilst maintain an atmosphere of 20% H_2. At each CO step, the a steady-state current was achieved. At 6500 s, the CO was removed and the current allowed to recover. This is shown in Figure 6.7A. A plot of $i_{\max}/i_{\mathrm{t}}$ versus [CO], where $i_{\max}$ is the current in 0% CO and i_{t} is the current at each CO step once stabilised, is shown in Figure 6.7B.

Although there is a slight increase in sensitivity to CO for E28D compared with native Hyd-1 (Figure 6.7B inset), the sensitivity of E28D does not reach that of Hyd-2.

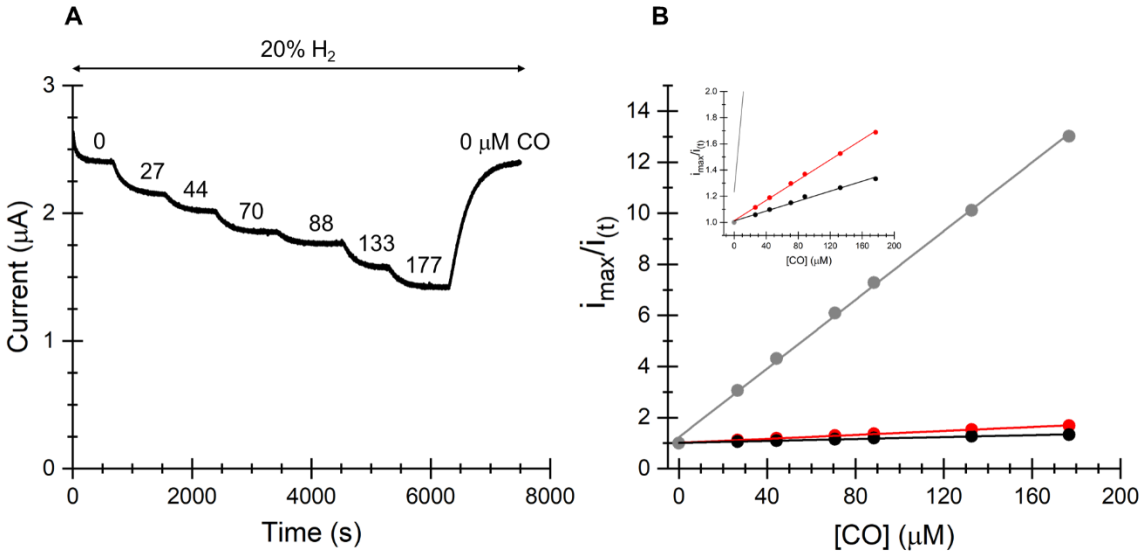


Figure 6.7: CO flow experiment for E28D. A – The CO sensitivity was measured as follows: the current response at -0.06 V was measured in 20% H_2 for approximately 650 s before introducing CO; the CO was then stepped from 1% to 20% whilst maintaining 20% H_2; after 6200 s the CO flow was stopped and the current in 20% H_2 measured for a further 1500 s. Other conditions: pH 6, 30 °C, total gas flow = 1000 scc min^{-1}, ω = 3000 rpm. B – A plot of $i_{\max}/i_{\mathrm{t}}$ versus [CO], where $i_{\max}$ is the current in 0% CO and i_{t} is the current at each CO step once stabilised. Plot includes an inset, showing a zoom in of the native Hyd-1 and E28D data.

6.7 pH dependence of E_{Kick}

The pH dependence of E_{Kick} was determined using the forwards and backwards scans of the cyclic voltammograms. At pH 10, E_{Kick} was masked by inactivation. At pH 4 and 5, E_{Kick} was not clear. E_{Kick} for pH 6 – 9 are marked on Figure 6.8. The pH dependence is shown in Figure 6.9.

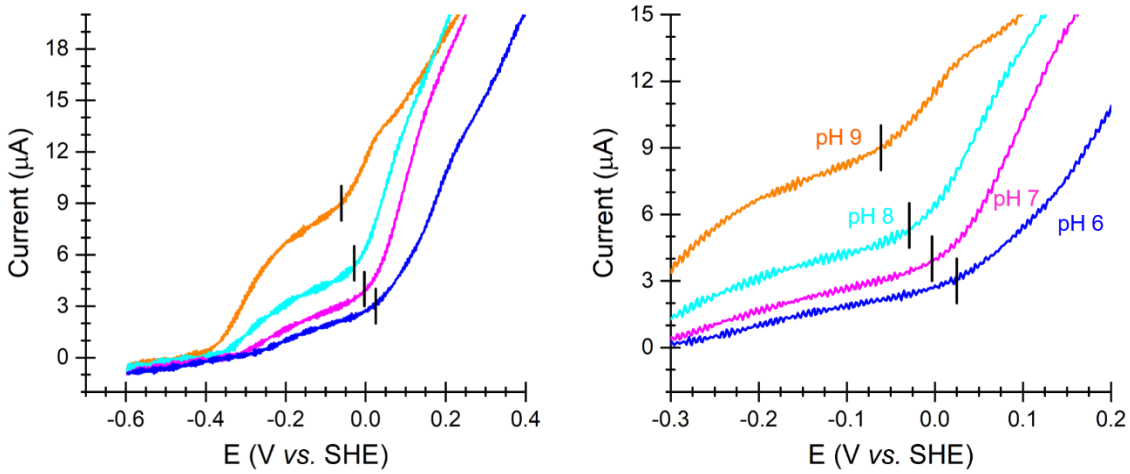


Figure 6.8: Determining E_{Kick} for E28Q. The black lines mark E_{Kick} for each pH. The right panel shows a close-up of the data surrounding E_{Kick}.

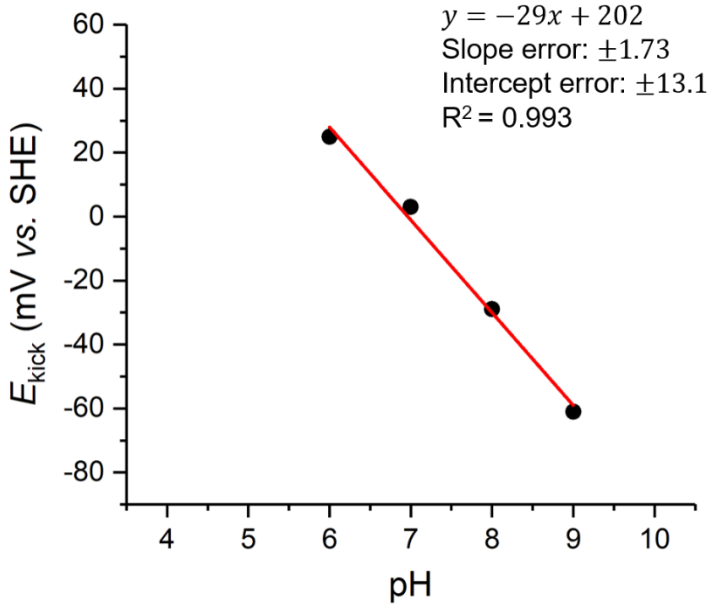


Figure 6.9: pH dependence of E_{Kick} for E28Q. the equation of the linear fit is included. The slope is -29 mV, which indicates a decrease of 29 mV (pH unit)$^{-1}$.